Dissertation
submitted to the
Combined Faculty of Mathematics, Engineering and Natural Sciences
of Heidelberg University, Germany
for the degree of
Doctor of Natural Sciences

Put forward by
Georgios Lioutas
born in: Trikala, Greece
Oral examination: 30.11.2022

Binary neutron star merger simulations on a moving mesh

Referees:	Priv.-Doz. Dr. Andreas Bauswein Prof. Dr. Björn Malte Schäfer

Zusammenfassung

In dieser Arbeit wird eine Erweiterung des Hydrodynamik-Codes AREPO vorgestellt, der die Gleichungen der Hydrodynamik auf bewegten Gittern löst. Die ursprünglich Newtonsche Implementierung wird auf allgemein relativistische Hydrodynamik erweitert, um relativistische Systeme mit diesem numerischen Schema zu modellieren. Diese Erweiterung beinhaltet die Kopplung an ein Modul, welches die Einsteinschen Feldgleichungen mithilfe der "conformal flatness" Näherung löst. Zur Validierung wird die Entwicklung isolierter Neutronensterne simuliert und mit unabhängigen Rechnungen verglichen. Eine erste relativistische Simulation einer Neutronensternverschmelzung auf einem bewegten Gitter wird präsentiert. Die Dynamik des Systems und allgemeine Merkmale des Gravitationswellensignals stimmen dabei mit unabhängigen Simulationen mit anderen Codes überein. Einige dynamische Merkmale nach der Verschmelzung wie die quasi-radialen Oszillationsmoden und die Doppelkernstruktur des Überrests bleiben jedoch in der Simulation mit AREPO länger erhalten, und das Gravitationswellensignal wird nach der Kollision der Sterne nur sehr langsam gedämpft. Dies deutet auf eine geringere numerische Viskosität in Simulationen auf bewegten Gittern hin und zeigt, dass dieser Ansatz für Modellierungen von verschmelzenden Neutronensternen sehr vorteilhaft sein kann. Ein weiterer Teil dieser Arbeit untersucht Schwingungsfrequenzen von isolierten Neutronensternen oder von Überresten von Neutronensternkollisionen. Dabei wird gezeigt, dass die Streuung von Datenpunkten in empirischen Relationen Informationen über die Zustandsgleichung von Neutronensternmaterie enthält.

Abstract

We discuss the extension of the, originally Newtonian, moving-mesh hydrodynamics AREPO code to study general relativistic systems. This includes the implementation of general relativistic hydrodynamics and coupling AREPO to a solver for the Einstein field equations, which adopts the conformal flatness approximation. We validate the implementation by evolving static neutron stars and comparing to independent calculations. We present the first general relativistic moving-mesh simulation of a neutron star merger. We find that the general dynamics and features of the post-merger gravitational wave emission agree with independent simulations performed with smoothed particle hydrodynamics and static-mesh tools. We observe that dynamical features in the post-merger phase, such as the quasi-radial oscillation mode and the double-core structure, survive longer in our moving-mesh simulation. Similarly, the post-merger gravitational wave signal is damped very slowly. These features suggest that the moving-mesh simulation has lower numerical viscosity and highlights that the moving-mesh approach can be very beneficial in simulations of neutron star mergers. As another part of this thesis, we examine relations between gravitational wave frequencies from isolated stars or merger remnants and stellar properties, such as the radius. We show that the scatter of points in such relations encodes information about the equation of state.

To my parents, Irini and Thanasi.

Contents

Nomenclature

List of acronyms

ADM	Arnowitt-Deser-Misner
BNS	binary neutron star
CFC	conformal flatness condition
CFL	Courant–Friedrichs–Lewy
EOS	equation of state
GRHD	general relativistic hydrodynamics
GW	gravitational wave
MC	monotonized central (slope limiter)
NS	neutron star
SPH	smoothed particle hydrodynamics
TOV	Tolman–Oppenheimer–Volkoff
1D, 3D	one-, three-dimensional

List of constants

c	speed of light
G	gravitational constant
$M_\odot$	solar mass

Part I

Motivation and theoretical background

1. Introduction

1.1. Physical system and observational aspects

In 2017 gravitational waves (GWs) from a binary neutron star (BNS) merger, named GW170817, were detected for the first time [6]. The latest stages before the merging, commonly called the inspiral, of the binary were measured [6]. Extensive searches were unable to detect a GW signal from the post-merger phase, placing such GW emission beyond the sensitivity of the detectors at that time [8, 11]. In addition to the GW observation, an electromagnetic counterpart was found in many different bands, from gamma rays to radio emission [7]. In particular, roughly 1.7 s after the time of merging, a gamma-ray burst was independently detected [5, 7, 130, 259]. An optical counterpart was observed about 11 h after the merger time, identifying NGC 4993 as the host galaxy [7, 81, 271, 298]. Observations over the course of the next, roughly, 30 days followed the evolution of the ultraviolet, optical and infrared component (see e.g. [7, 302] and references therein). Finally, X-ray and radio emission were found roughly 9 and 16 days after the merger event, respectively [7, 140, 204, 293].

The event provided observational data that have already proved to be extremely useful in our efforts to better understand BNS mergers as astrophysical sites, as well as neutron stars (NSs) and their physics. The detection of gamma rays from the event supports theoretical work which considers BNS systems as possible progenitors for short gamma-ray bursts [54, 107, 216]. Interestingly, the observed gamma-ray emission is sub-luminous compared to typical short gamma-ray bursts, while the identified components in its spectrum, the overall spectral evolution and subsequent emission (e.g. X-ray afterglow) are unlike other observed short gamma-ray bursts [7, 217, 236]. The interpretation of the gamma-ray (as well as X-ray and radio) observation and the underlying mechanism which produced the emission are not yet fully understood, e.g. [134, 186, 217, 236].

The analysis of the observed light curves in ultraviolet, optical and infrared bands provides strong evidence that heavy elements are synthesized in the ejecta of BNS mergers [7, 163, 282, 306]. BNS mergers were proposed as a possible production site of elements heavier than iron already decades ago [84, 106, 120, 183, 184, 279]. Material becomes gravitationally unbound during these merger events and heavy element nucleosynthesis can take place in the ejecta via the rapid neutron capture process (r-process). The radioactive decay of the newly formed, heavy, unstable nuclei can be observed as an electromagnetic transient, commonly referred to as kilonova [188, 208, 209]. Modeling the observed light curves can help determine the properties of the ejected material, such as the total ejected mass, composition and velocities (see e.g. [26, 164, 302]). Notably, based on the extracted r-process production rates, BNS mergers might be the main site of r-process nucleosynthesis [302].

Focusing on the GW observation, the analysis of the GW signal from the inspiral provided constraints for the tidal deformability and the radius of static NSs and, subsequently, the equation of state (EOS) [6, 9, 10]. Such constraints are extremely important in our effort to unveil the exact behavior of matter at the high densities found in the interior of NSs. In particular, NSs reach densities of a few times the nuclear saturation density ($\rho_{\mathrm{sat}} \approx 2.7 \cdot 10^{14}\ \mathrm{g} \cdot \mathrm{cm}^{-3}$). The exact composition of matter and the EOS at such high densities is only partially known [65, 138, 221]. Due to the uncertainties, a large number of EOS models have been proposed.

The general relativistic equations governing hydrostatic equilibrium, widely known as the Tolman–Oppenheimer–Volkoff (TOV) system [225, 289], uniquely link stellar properties of static stars to the (zero-temperature) EOS. Under the assumption of a specific EOS, the TOV system can be solved starting from a value for the central density of the star. Different initial values for the central density yield distinct stellar configurations, characterized by a number of properties such as the mass, radius, moment of inertia and tidal deformability[1]. Collecting all the configurations modeled by a specific EOS produces relations between e.g. the mass and the radius or tidal deformability of static NSs. Each EOS results in unique relations between stellar properties. Thus, measuring stellar parameters of static NSs directly translates to constraints on the EOS (e.g. [191, 192, 194, 195]).

The masses of some NSs have been measured with high precision (see e.g. [20, 25, 227]). However, determining properties such as the radius through electromagnetic observations is more difficult, which hinders our ability to strictly constrain the EOS. Prior to the GW observation, arguably the main constraint on the EOS came from mass measurements of massive NSs, which provide a lower limit on the maximum mass that the EOS should be able to support [24, 28, 85, 90, 190]. Following the GW observation, the analysis of the multi-messenger observation from various groups has resulted in a number of constraints on the EOS and stellar properties of static stars that an EOS should be able to reproduce, e.g. [9, 10, 47, 112, 169, 203, 241, 244, 248, 255, 266]. This highlights the importance of BNS mergers in determining the high-density EOS.

GWs from the inspiral of another event, GW190425, were observed in 2019 [3]. The analysis of the event identified it as a probable BNS merger. A particularly interesting aspect of the system is its high total mass of roughly 3.4 $M_{\odot}$, which is significantly higher compared to other observed galactic BNSs [3, 111]. Due to detectors being either offline or having insufficient sensitivity to observe the (low signal-to-noise ratio) event, GW190425 was a single-detector event. The extracted values for the tidal deformability and the radius from this event did not provide additional constraints on the EOS [3]. Moreover, despite efforts, no follow-up electromagnetic observation was made [80].

The two observations of BNS mergers, GW170817 and GW190425, alongside a number of other GW observations [2, 12, 283, 284], highlight the potential that GWs offer for the detection and study of mergers of compact objects (such as NSs and black holes). GW170817, jointly with the follow-up electromagnetic observations, has already showcased that BNS mergers are extremely important in the study of topics such as the high-density EOS, heavy element nucleosynthesis and the r-process[2]. What

---

[1] Note that the tidal deformability Λ is defined as $\Lambda = \frac{2}{3} k_2 \left(\frac{c^2 R}{GM} \right)^5$, where k_2 is the tidal Love number [86, 151, 152], while M and R refer to the mass and radius of the respective stellar model.

[2] Many other directions have been explored, including e.g. an independent determination of the

remains elusive up to now is the observation of the post-merger phase from a BNS system.

Theoretical studies of the system based on full three-dimensional (3D) numerical simulations show that, after the merging, different possibilities exist for the nature of the remnant [31, 263, 267]. The outcome of the merger depends primarily on the total mass of the binary system and the EOS [40, 155]. Binary systems with a total mass above a threshold, EOS-dependent mass M_{thres} promptly collapse to a black hole. The threshold mass, over which a direct collapse to a black hole takes place, is informative about the EOS (e.g. [40–42]). Systems with a total binary mass below M_{thres} result in hot, massive, differentially rotating NS remnants[3], which are further supported mainly by rotation. These systems can potentially also collapse to a black hole on longer timescales, because the NS remnant dynamically evolves through different mechanisms, such as energy and angular momentum losses due to GW emission, mass loss, angular momentum redistribution and neutrino cooling. Angular momentum redistribution gradually turns differential rotation into uniform rotation in the remnant. However, differential rotation is able to support more mass than uniform rotation [38]. Hence, remnants with masses below M_{thres}, but above the maximum mass that uniform rotation can support [78, 79], also collapse to a black hole in a delayed fashion. Remnants that can be supported by uniform rotation further spin down. Thus, they also collapse on longer timescales, unless their total mass is smaller than the maximum mass of static NSs that the EOS can support.

NS remnants form after the collision of the two companion stars, thus they exhibit nonaxisymmetric deformations (e.g. double-core structure, spiral density arms) and feature quasi-radial and nonaxisymmetric oscillations of the matter. The remnant emits GWs (e.g. [31, 48, 268, 269]), while features of the post-merger GW spectrum have been related to fluid oscillations [275]. Most importantly, the post-merger GW emission carries information about the EOS [44, 45, 57, 59, 73, 75, 280, 281, 305]. Hence, potential future GW observations of the post-merger phase offer the possibility to constrain the EOS in a complementary way to what has already been done.

The Advanced LIGO [189], Advanced Virgo [13] and KAGRA [162] detectors currently undergo upgrades as we approach the next observing run [4]. Current estimates predict that the number of BNS detections over a one-calendar-year observing run could be of the order of 10 [4]. The efforts of these three detectors are further aided by the GEO600 detector [96, 161], while another detector (LIGO-India [158]) is planned, which should increase detection rates and sky localization accuracy [110, 257, 261]. In addition, next-generation detectors such as the Einstein Telescope [238] and the Cosmic Explorer [1] are planned with design sensitivities roughly an order of magnitude higher than the design sensitivity of current detectors.

The extensive and ongoing effort to improve current GW detection capabilities increases the likelihood of more BNS observations in the upcoming years. Electromagnetic observations from these systems can provide important data for understanding the kilonova and the r-process. This highlights the need to devote similar efforts to expand and improve our theoretical knowledge of the system. Modeling the late inspiral stages, as well as the merger and the post-merger phase, can only be done

---

Hubble constant [6] and constraints on alternative theories of gravity [33].

[3] In this thesis, we consider only systems which produce a hot, massive NS remnant, which survives at least for a few tens of milliseconds. Throughout the text, we employ the term "remnant" to directly refer to such systems.

numerically. Hydrodynamical simulations are required to understand the post-merger dynamics leading to the emission of GWs. Furthermore, these simulations determine the properties of the ejecta (e.g. the amount, composition, entropy and density evolution of ejected material), which are necessary as initial conditions for realistic r-process calculations. As a result, better understanding the system and interpreting potential future GW or electromagnetic observations relies on further developing, ideally improving, our numerical modeling and closely investigating the simulation results. This thesis tries to take a step in this direction.

1.2. Numerical modeling

Numerical simulations of general relativistic systems require the treatment of general relativistic hydrodynamics (GRHD), as well as a dynamical spacetime. In Chapter 5 we discuss in detail a BNS merger, which results in a remnant that is supported against collapse to a black hole for at least a few tens of milliseconds. The discussion highlights the many physical processes that a simulation code should be able to resolve. These include, but are not limited to, the accurate evolution of the two stars in the inspiral (which is crucial for GW waveform modeling, see e.g. [93]), the formation of shocks and fluid instabilities particularly at the collision interface and the overall angular momentum redistribution in the remnant during the post-merger phase. In addition, investigating problems such as the nucleosynthesis of heavy elements in the matter which becomes unbound relies on resolving small amounts of ejecta, which move with high velocities over large distances.

Numerical studies with various codes suggest that simulation results feature uncertainties. In BNS merger simulations, aspects such as the properties of post-merger mass ejection, the orbital evolution in the inspiral and the characteristics of the GW signal (e.g. inspiral GW waveforms) are influenced up to some extent by numerics (e.g. resolution, employed numerical schemes) [43, 56, 154, 167, 215, 243]. For instance, ejecta masses extracted from simulations employing different resolutions admit relative errors of the order of $\approx 50\%$ [243]. Studies with different codes report similar uncertainties, e.g. [43, 123].

The most widely used approaches to treat relativistic hydrodynamics are Eulerian grid-based methods, such as finite-difference, finite-volume or discontinuous Galerkin schemes, and Lagrangian smoothed particle hydrodynamics (SPH) (see Sections 2.2 and 2.3). For more details and a better exposition of the various methodologies see for example [17, 37, 115, 206, 249, 253, 265, 311]. A number of codes have been developed and employed in the study of general relativistic systems based on these methodologies. For example, surveys of codes can be found in [32, 115, 119], while recently some relativistic SPH implementations were introduced in [200] (adopting a fixed spacetime metric) and in [92, 254] (including a dynamical spacetime and applications to BNS mergers). Both Eulerian grid-based methods and SPH have their respective advantages and drawbacks.

Eulerian methods discretize the relativistic hydrodynamics equations employing a fixed grid. Commonly, (adaptive) mesh refinement techniques are implemented in addition to place resolution in regions of physical interest. Over the course of the years, a set of high-resolution shock-capturing methods have been developed, which ensure that grid-based methods resolve shocks and fluid instabilities with accuracy.

On the other hand, Eulerian methods can suffer from grid orientation effects, while they typically introduce an artificial, low-density atmosphere to treat formally vacuum regions (see e.g. [117] and Section 3.8). Moreover, resolving the low-density, high-velocity ejecta can be difficult.

SPH discretizes the GRHD equations based on a set of particles. Each particle corresponds to a specific rest mass, which leads to excellent mass conservation. The particles follow the fluid motion making the scheme Lagrangian. Due to its Lagrangian nature, SPH resolves advection with high accuracy, while tracing ejecta trajectories is straightforward. Vacuum translates to the absence of particles, so no additional effort is required in zero-density regions. However, resolving shock and treating fluid instabilities is more challenging for SPH compared to grid-based approaches (see however e.g. [253] for recent developments). In addition, including a dynamical spacetime requires to solve Einstein's field equations. The metric field equations cannot be treated on the particle level. Instead, they are solved on an independent grid and additional effort is required to communicate between the particles and the metric grid. In principle, the same holds for other fields which do not vanish in vacuum (e.g. magnetic fields), i.e. where the method lacks resolving power.

Evidently, Eulerian grid-based methods and SPH both offer benefits. Moreover, one can find cases where one method includes features that make it particularly appealing, while the other approach faces challenges and vice versa. In an attempt to combine some of the best aspects of both approaches, the moving-mesh code AREPO was developed [273].

AREPO discretizes the equations of Newtonian hydrodynamics on an unstructured mesh. The mesh corresponds to the Voronoi tesselation of a set of mesh-generating points. The mesh-generating points can in principle be distributed in an arbitrary way. In addition, they can move freely (see Section 3.7 and [273] for more details), altering the mesh geometry in a continuous way. Due to the discretization on a mesh, the method inherits many of the benefits of grid-based methods, such as accurate shock resolution. Moreover, the moving-mesh approach obtains a quasi-Lagrangian nature if the mesh-generating points are moved with the local fluid velocity. In Chapter 3 we discuss aspects of the moving-mesh scheme in more detail.

Since it was originally introduced, AREPO has been employed in the study of a broad range of problems in fields such as cosmology, Type Ia supernovae, the common envelope phase in binary stars and many more (e.g. [136, 174, 222, 230, 231, 260, 303, 307]). Several other moving-mesh codes have subsequently been introduced and used to study various astrophysical systems [29, 71, 100–102, 124, 301, 317]. Overall, studies with the moving-mesh scheme have exhibited that it can be rather advantageous in comparison to traditional approaches.

In the moving-mesh approach, the geometry of the initial mesh can be chosen to be well-adapted to the properties of the physical system, while mesh-generating points can follow the motion of the fluid. In addition, AREPO can split or merge cells based on nearly arbitrary criteria. As a result, during a moving-mesh simulation, resolution can follow the fluid motion reducing numerical errors due to advection, while locally increasing or decreasing the resolution can further ensure that physically interesting regions are resolved. These features make the moving-mesh approach particularly appealing for simulations of compact objects, particularly BNS systems. Notably, most of the moving-mesh codes treat Newtonian hydrodynamics. Only recently some moving-mesh codes were extended to solve the GRHD equations [70, 256]. However, up to date, these implementations do not include a solver for a dynamical spacetime, but the spacetime is kept fixed. Naturally, simulating BNS mergers requires the inclusion of a dynamical spacetime. In this thesis, we present the first moving-mesh implementation which includes a dynamical spacetime [196].

The main focus of this thesis is performing general relativistic simulations with AREPO (using the upgraded version described in [232] as our basis code). This requires implementing GRHD in the code and coupling the code to a metric solver. The metric solver implementation originates from [220] and solves the metric field equations employing the conformal flatness condition (CFC) [157,312]. Moreover, we implement microphysics modules to account for the high-density EOS in NS simulations. In the present work, we describe tests which validate our implementation. Most importantly, we also discuss the first simulation of a BNS merger on a moving mesh. More details about the implementation, the tests and the binary simulation can be found in Part II of the thesis, while additional information and a short introduction to the main concepts involved in the numerical modelling of general relativistic systems are presented in Chapter 2. Our main results can be found in [196].

1.3. Gravitational wave asteroseismology

Another direction which we consider in this thesis is GW asteroseismology. Asteroseismology employs stellar oscillations to study the internal structure of stars. Naturally, this idea has been considered in the case of NS systems as well, e.g. [172]. The internal structure of NSs depends on the EOS, which is only partially known (e.g. [148,178,180,182,221,226]). This makes fluid oscillations which lead to the emission of GWs particularly interesting. Relating the characteristics of the oscillation and the resulting GW emission to stellar properties can be informative about the EOS. From a theoretical standpoint, this requires to numerically calculate the characteristics of the GW signal (e.g. the frequency) for a large set of EOSs and stellar models and, subsequently, identify possible correlations with stellar parameters. This allows to construct relations between the properties of the GW signal and stellar parameters by fitting the data.

BNS systems are a prominent source of GWs. Hence, they are a very interesting system to consider from the point of view of GW asteroseismology. The general dynamics in the post-merger phase is rather complicated. A proper analysis is required to relate features of the GW spectrum to the fluid dynamics [275]. In addition, fluid oscillations in isolated stars, which are a simpler system, can be studied and provide important knowledge that might be applicable in the case of BNS remnants as well. In this thesis, we consider both these two very distinct NS systems, namely isolated NSs and BNS merger remnants, in an effort to better understand GW asteroseismology relations.

One of the main fluid oscillations in isolated NSs is the fundamental quadrupolar fluid mode ($f-$mode), which is a strong GW emitter (see e.g. [172]). A number of different relations have been proposed, which relate the frequencies of the GW emission due to the $f-$mode to stellar properties of isolated stars [22,68,185,295]. These relations are largely insensitive to the neutron star EOS. Moreover, they involve different stellar parameters, such as the mass, radius, moment of inertia and tidal deformability. Hence, assuming the GW frequency of the $f-$mode for a particular stellar configuration is measured, these relations offer the possibility to place constraints on the stellar properties that an EOS should be able to reproduce.

Remnants of BNS mergers also feature fluid oscillations. The dominant fluid oscillation leads to the emission of GWs with a frequency (denoted by f_{peak} throughout this work) of a few kHz. More details can be found for example in [44, 45, 57, 76, 153, 218, 264, 268, 276, 281, 315] and also in reviews (and included references) such as [30, 51, 53, 55, 93, 122, 258]. Unfortunately, the post-merger phase of both the BNS merger GW170817 [6, 8] and the potential BNS merger GW190425 [3] was outside the sensitivity limits of the detectors, not allowing a measurement of f_{peak}. Nevertheless, upgraded current detectors operating at design sensitivity or more sensitive next-generation detectors should be able to observe the post-merger phase in the near future and measure f_{peak} [14, 15, 61, 62, 73, 75, 76, 104, 105, 126, 139, 147, 207, 224, 228, 292, 294, 318]. Similarly to the case of the $f-$mode in isolated stars, various relations between f_{peak} and different stellar parameters have been proposed, e.g. [44, 45, 57, 59, 281, 305]. Hence, measuring f_{peak} would allow us to extract information about stellar properties which are uniquely linked to the EOS.

The accuracy of the employed relation determines how strict the constraints that we can place on the EOS are. A proper comparison between different relations requires to extract them based on a consistent data set. In this thesis, we evaluate the accuracy of GW asteroseismology relations both for isolated stars, as well as for BNS remnants (see Section 6.2). We compute $f-$mode GW frequencies employing a code which solves the linear perturbation equations [198], while f_{peak} is extracted based on 3D simulations with an SPH code [219, 220] (see Section 6.1). A comparison between various proposed relations was presented in [74], which, however, considers only isolated NSs, significantly less EOSs and a subset of the relations discussed here.

Furthermore, we investigate whether the scatter of the data points, particularly how individual points distribute with respect to the fit to all data, contains additional information about the high-density EOS. This direction has only been considered recently in the literature in more detail [197, 245]. Various studies support that the dominant fluid oscillation in BNS remnants originates from the $f-$mode [49, 53, 67, 276]. This motivates to study the scatter in relations for isolated NSs and BNS mergers side by side. If the exact distribution of data points is strongly influenced by the EOS and the underlying mechanism is prevalent enough, one would expect that relations of the same type should exhibit many similarities for these two systems. In this thesis, we discuss this aspect in detail (see Section 6.3) and investigate whether this direction can provide tighter EOS constraints from observations. Our results are presented in [197].

1.4. Aims and outline

We now briefly summarize the main goals and provide an outline of the thesis. This work focuses on:

(i) Extending the moving-mesh code AREPO in order to study general relativistic systems with a dynamical spacetime. The combined volume of simulations discussed in this thesis tries to answer a series of questions. Can the moving-mesh approach be employed to study general relativistic systems? Can we perform high resolution moving-mesh simulations with reasonable computational demands? Is it possible that features of the moving-mesh approach observed in Newtonian simulations, such as the low numerical diffusivity, persist in BNS simulations? Overall, can the moving-mesh approach be beneficial for simulations of BNS mergers?

(ii) Analyzing the scatter in GW asteroseismology relations referring to either isolated NSs or BNS merger remnants. We define frequency deviations as the distance of individual data points from the fit to all data (measured in Hz) in GW frequency versus stellar properties (e.g. the radius or tidal deformability) plots. Based on the analysis of the data we address a number of questions. How accurate are the various GW asteroseismology relations based on a consistent data set? Do frequency deviations follow the same systematic behavior in isolated NSs and BNS merger remnants? Do frequency deviations carry additional information about the high-density EOS? How can we employ frequency deviations to further constraint the EOS? Does the agreement between frequency deviations in isolated NSs and post-merger NS remnants imply tight relations between the $f-$mode GW frequency in single NSs and the dominant fluid oscillation frequency $f_{\rm peak}$ in BNS remnants, even considering a broad range of total binary masses and mass ratios?

The outline of the thesis is the following: In Chapter 2 we provide a brief overview of the numerical techniques which we employ to study the dynamics of NS systems. Chapter 3 discusses the moving-mesh approach and provides details of our GRHD implementation in Arepo and the coupling to the metric solver. In Chapter 4 we evolve isolated, static NSs on a fixed or dynamical spacetime with Arepo in order to validate our implementation. We extract the frequency of the radial mode and compare to results from independent codes, while we also discuss various aspects of the simulations. In Chapter 5 we perform the first BNS merger simulation on a moving-mesh with Arepo. We discuss extensively the details of the simulation. The main focus is placed on the dynamics of the remnant and the post-merger GW emission. Chapter 6 focuses on GW asteroseismology relations for isolated NSs and NS remnants from BNS mergers. In particular, we extensively examine how individual models, described by different EOSs, scatter w.r.t. to the respective fit to all models. Finally, in Chapter 7 we provide a summary of our results, draw conclusions and outline future directions. Additionally, Appendix A investigates aspects which affect the accuracy of GW asteroseismology relations for BNS merger remnants and is particularly relevant to the discussion of Chapter 6.

Additional notes: Throughout this thesis we employ four different codes, featuring different degrees of complexity, to study NS dynamics[4]. The codes and my (main) contributions are:

(i) The Arepo moving-mesh code [273]. As our basis version, we employ the Newtonian version outlined in [232]. In this thesis, we discuss an extension to simulate general relativistic systems [196]. The GRHD implementation in the code was primarily developed by Andreas Bauswein. My main contributions

---

[4] Excluding codes used to generate initial data, which we reference in the appropriate places in the text.

include coupling the code to a metric solver, adding microphysics modules for the high-density EOS, extensively testing to validate the implementation, setting up the infrastructure for BNS simulations (e.g. importing BNS initial data for unstructured meshes) and investigating how various aspects of the mesh (e.g. initial mesh geometry and mesh motion) affect NS simulations. The metric solver implementation originates from [220]. The simulations with Arepo discussed in Chapters 4 and 5 and their analysis were carried out by me.

(ii) A 3D general relativistic SPH code [219, 220]. I am a user of the code and have not actively contributed to its development. Data from the SPH code are employed in Chapter 6. The analysis is performed by me.

(iii) A code which solves the linear perturbation equations for the fundamental quadrupolar fluid mode in isolated NSs [198]. The code was developed by me.

(iv) A perturbative code computing radial modes in isolated NSs. The code was developed by me.

References regarding the underlying theoretical formulations and numerical schemes can be found in the respective places in the text.

1.5. Conventions

Throughout this thesis we set $c = G = 1$, unless otherwise specified. Greek indices refer to space and time components and run from 0 to 3, while Latin indices denote spatial components and run from 1 to 3. Unless otherwise stated, Einstein summation notation is employed. Moreover, we adopt the signature $(-, +, +, +)$ for the metric. Differential operators Δ and ∂_i are with respect to the flat three metric.

In Part III we briefly discuss binary systems where the two NSs have different masses. We define the mass ratio as $q = M_1/M_2 \leq 1$, where M_1 and M_2 are the masses of the two companion stars in the binary system. In addition, we construct fits based on a number of data points and subsequently consider the deviations of individual data points from the respective fit. Assuming a data set (X_i, Y_i) consisting of N points, we employ the notation $\delta_X Y$ for deviations in Section 6.3. For a given data point i we define its deviation from the respective fit to all data as

$$\delta_X Y_i = Y_i - Y_{\text{fit}}(X_i). \tag{1.1}$$

Here Y_{fit} is the fit to the data. The maximum and average deviation then follow as

$$\max\left(\delta_X Y\right) = \max_i\left(|\delta_X Y_i|\right), \tag{1.2}$$

$$\overline{\delta_X Y} = \frac{\sum_{i=1}^{N} |\delta_X Y_i|}{N}, \tag{1.3}$$

where by $|\cdot|$ we denote the absolute value.

2. Theoretical formulation and numerical approaches

The numerical study of NS systems requires to treat GRHD, as well as capture the dynamics of the spacetime. In this work, we carry out full 3D simulations, as well as perturbative calculations. This chapter provides an overview of the main methods that we employ, alongside details about their numerical implementation. We devote Chapter 3 to a more extensive discussion on moving-mesh hydrodynamics, which is the main focus of this thesis. Chapter 3, alongside Sections 2.1, 2.2, 2.4, 2.5.1 and 2.6, serve as the theoretical background for the simulations discussed in Chapters 4 and 5. We employ the techniques outlined in Sections 2.3, 2.4, 2.5.2 and 2.6 for the results presented in Chapter 6.

2.1. General relativistic hydrodynamics

We consider the Arnowitt-Deser-Misner (ADM) 3+1 decomposition, which foliates the spacetime into a set of non-intersecting spacelike hypersurfaces with a constant coordinate time t [27]. In the ADM formalism, the general metric element reads

$$ds^2 = g_{\mu\nu} dx^\mu dx^\nu = \left(-\alpha^2 + \beta_i \beta^i\right) dt^2 + 2\beta_i dx^i dt + \gamma_{ij} dx^i dx^j, \tag{2.1}$$

where $g_{\mu\nu}$ is the spacetime $4-$metric, α denotes the lapse function, β^i is the shift vector and γ_{ij} the spatial $3-$metric.

Throughout this work we assume a perfect fluid with an energy-momentum tensor

$$T^{\mu\nu} = \rho h u^\mu u^\nu + p g^{\mu\nu}, \tag{2.2}$$

where ρ is the rest-mass density, $h = 1 + \epsilon + p/\rho$ is the specific enthalpy, ϵ is the specific internal energy, p is the pressure and u^μ is the $4-$velocity of the fluid.

A complete hydrodynamic description consists of determining at least 6 variables, i.e. ρ, p, ϵ and u^i. Assuming a typical EOS of the form

$$p = p(\rho, \epsilon), \tag{2.3}$$

eliminates the need to independently compute e.g. the pressure p. The remaining variables form the set of primitive variables $\mathbf{W} = (\rho, v^i, \epsilon)$, where $v^i = (u^i/u^0 + \beta^i)/\alpha$ is the fluid $3-$velocity.

The hydrodynamic evolution follows from solving the local conservation laws for the energy-momentum tensor and the matter current density $J^\mu = \rho u^\mu$, namely

$$\nabla_\mu T^{\mu\nu} = 0, \tag{2.4}$$

$$\nabla_\mu \left(\rho u^\mu\right) = 0. \tag{2.5}$$

By introducing a set of appropriate conserved variables, we can cast the conservation laws into a system of first-order flux-conservative hyperbolic differential equations, called the Valencia formulation [35, 115]. In the Valencia formulation, the GRHD equations read

$$\partial_0\left(\sqrt{\gamma}\mathbf{U}\right) + \partial_i\left(\sqrt{\gamma}\mathbf{F}^i\right) = \mathbf{S}. \tag{2.6}$$

The set of conserved variables form the state vector

$$\mathbf{U} = \begin{pmatrix} D \\ S_i \\ \tau \end{pmatrix} = \begin{pmatrix} \rho W \\ \rho h W^2 \upsilon_i \\ \rho h W^2 - p - D \end{pmatrix}, \tag{2.7}$$

where $W = \alpha u^0 = (1 - \gamma_{ij}\upsilon^i\upsilon^j)^{-1/2}$ is the Lorentz factor. Furthermore, $\mathbf{F^i}$ and $\mathbf{S}$ correspond to the flux and source vectors defined as

$$\mathbf{F}^i = \alpha \begin{pmatrix} D\left(\upsilon^i - \frac{\beta^i}{\alpha}\right) \\ S_j\left(\upsilon^i - \frac{\beta^i}{\alpha}\right) + p\delta^i_j \\ \tau\left(\upsilon^i - \frac{\beta^i}{\alpha}\right) + p\upsilon^i \end{pmatrix}. \tag{2.8}$$

and

$$\mathbf{S} = \alpha\sqrt{\gamma} \begin{pmatrix} 0 \\ T^{\mu\nu}\left(\partial_\mu g_{\nu j} - \Gamma^\lambda_{\nu\mu} g_{\lambda j}\right) \\ \alpha\left(T^{\mu 0}\partial_\mu \ln\alpha - T^{\mu\nu}\Gamma^0_{\nu\mu}\right) \end{pmatrix}, \tag{2.9}$$

respectively. Here $\Gamma^\lambda_{\nu\mu}$ are the Christoffel symbols of the metric and $\gamma = \det(\gamma_{ij})$ the determinant of the spatial 3-metric. We also introduce the definitions $\boldsymbol{\mathcal{U}} = \sqrt{\gamma}\mathbf{U}$ and $\boldsymbol{\mathcal{F}}^i = \sqrt{\gamma}\mathbf{F}^i$, which shall prove useful in Chapter 3, where we discuss in more detail how we solve Eqs. (2.6) in a finite volume fashion in AREPO.

More formulations exist for the GRHD equations (see e.g. [115, 249, 265]). The main advantage of the Valencia formulation is the hyperbolic, conservative nature of the equations. This allows the extension of a number of high-resolution shock-capturing schemes, initially developed for Newtonian hydrodynamics, to general relativistic applications. In the following section, we briefly discuss the standard methodology to solve the GRHD equations in the case of fixed-grid finite volume methods. We refrain from explicitly providing relations and extensive details. Our purpose is to present a brief outline of the main steps. More details can be found in e.g. [17, 37, 115, 206, 249, 253, 265, 311]. We devote Chapter 3 to describe such schemes in the case of moving-mesh hydrodynamics and in particular how they are implemented in the general relativistic version of the AREPO code.

2.2. Fixed-grid finite volume method

In order to numerically solve the GRHD Eqs. (2.6), an appropriate discretization scheme is necessary. Finite volume methods split the computational domain into a set of discrete cells and define averages of the conserved quantities in each one of the cells. The evolution of the system follows from updating each individual cell-averaged state, based on the ingoing/outgoing fluxes through the corresponding cell's boundaries, over the course of an appropriately chosen time step.

At the core of finite volume methods lies the observation that one can define a local Riemann problem at each interface between neighboring cells [129]. Computing the fluxes through an interface requires to solve the corresponding Riemann problem. To define the Riemann problem the fluid state on both sides of the common interface needs to be computed. These two states are typically called the “left” and “right” states. Computing the “left” and “right” states at any interface constitutes the reconstruction step. Many different methods exist for reconstructing the states. We outline some of the most commonly used ones here.

(i) Slope-limited piecewise linear reconstruction computes the value of a variable, at any point within a cell, by constructing a linear function (see e.g. [290]). The function includes a slope limiter, which modifies the slope by incorporating information about the value of the variable in the neighboring cells (see Section 3.3). Various slope limiters have been proposed in the literature, including the monotonized central (MC) [299], minmod [300] and superbee [250] limiters. The motivation behind slope-limited reconstruction is to construct total variation diminishing schemes, which eliminate spurious oscillations from the solution [143,144]. The method achieves second-order accuracy at all points, except for local extrema and shocks.

(ii) Other commonly used reconstruction methods include the piecewise parabolic method [77], essentially non-oscillatory schemes [145], weighted essentially non-oscillatory methods [201] and the monotonicity-preserving fifth-order reconstruction [278].

As soon as information about the “left” and “right” state at each interface is available, a Riemann solver is employed to compute the flux of conserved quantities through the face. Multidimensional exact solvers are computationally expensive, thus approximate solvers are typically used. Common choices include the HLLE [108, 146] and HLLC [210, 291] solvers. Riemann solvers are classified as complete or incomplete, based on the assumptions they make about the structure of the solution. In the case of GRHD, the solution of the Riemann problem consists of three waves. HLLC is a complete solver, because it includes all three possible characteristic waves, while HLLE is a two-wave model and hence incomplete. Extending HLLE to curved spacetimes is straightforward, while the solver yields accurate results. These features make it a common choice in GRHD codes.

Up until this point, we have only discussed the spatial discretization of Eqs. (2.6). The spatial and time discretization can be considered separately based on the method of lines. In particular, by discretizing all spatial components, the initial set of partial differential equations turns into ordinary differential equations in time. The time integration can then be carried out with standard numerical integrators, such as explicit Runge-Kutta methods. In order to guarantee the convergence of the solution, the time step of the integration needs to satisfy the Courant–Friedrichs–Lewy (CFL) condition [82, 83].

The GRHD equations include non-zero source terms due to the spacetime geometry (see Eqs. (2.6) and (2.9)). Their contribution to the solution can either be added alongside the fluxes, in accordance with the chosen time integrator, (unsplit methods) or independently consider the flux and source terms (fractional-step methods). In the second case, the solution is propagated in time in multiple steps, which consider either the flux terms only (thus solve a homogeneous set of differential equations) or focus on the source terms alone and solve the corresponding ordinary differential equations without the fluxes.

The overall accuracy of the solution is determined by the accuracy of the methods used for both the spatial discretization and the time integration. As a result, it is important to couple a high-order time integration scheme to similarly high-order spatial schemes (e.g. reconstruction).

As a few final remarks on finite volume techniques we note the following. The finite volume approach works with cell-averaged quantities. As a result, at the end of each time step, we obtain the state vector of each cell, i.e. the conserved quantities. From a physical point of view it is more useful to know the values of the primitive variables at the cell centers. Even though computing the conserved quantities from the primitive ones is straightforward based on the definitions (2.7), the inverse procedure cannot be carried out analytically. Instead, a root-finding method is used to recover the primitive variables from the conserved variables (see Section 3.5 for more details).

Furthermore, the standard Eulerian formulation that we discuss faces problems at vacuum regions. A rather popular approach to circumvent the problem is to include a very low density artificial atmosphere, many orders of magnitude below the maximum density within the computational domain [117] (see Section 3.8). Alternative formulations have been proposed, which alleviate the issue [99].

2.3. Smoothed particle hydrodynamics

An alternative way to treat hydrodynamics is SPH [127, 202, 211]. Instead of solving the GRHD equations on a grid, SPH employs a set of particles comoving with the fluid and expresses dynamics in terms of operations at the particle level. Hence, SPH is a purely Lagrangian method. We focus our description to a specific general relativistic SPH code [219, 220], because in Chapter 6 we discuss results from [197] based on a number of simulations employing the results from [45, 48, 219, 220].

Similarly to the case of finite volume methods, we focus first on the spatial dimensions. Within SPH, the first step in this direction is an interpolation method. In particular, a function $f(\mathbf{r})$ (e.g. the density ρ) is approximated at a point with coordinates $\mathbf{r}$ as

$$f_I(\mathbf{r}) = \int f(\mathbf{r}')W(\mathbf{r}-\mathbf{r}', h)d^3\mathbf{r}', \tag{2.10}$$

where W is the kernel function and h the smoothing length, which determines the integration domain (see e.g. [251]). The kernel function needs to be normalized and have compact support. Furthermore, it should tend to the Dirac delta distribution at the limit $h \to 0$, so that we recover the function $f(\mathbf{r})$ at the limit of vanishing h. Unless otherwise stated, in the simulations discussed in this thesis we employ the spherically symmetric spline kernel [213]. In a few cases, we opt for the Wendland kernel [89, 310].

Since SPH divides the fluid to a set of particles, the integral (2.10) can be approximated as a summation over the particles

$$f_S(\mathbf{r}) = \sum_b f(\mathbf{r_b})\frac{m_b}{\rho_b^*}W(\mathbf{r}-\mathbf{r_b}, h), \tag{2.11}$$

where m_b is the rest mass of the particle denoted by b. Computing the value of a quantity at any point follows from Eq. (2.11), where in the summation we take into account all the particles with a smoothing length around their position which includes the point of interest. The smoothing length of each particle changes based on the local particle density [211]. In the SPH code that we employ, the smoothing length of most particles is regulated to include roughly 100 neighbors.

Similarly to the Eulerian formulation presented in Section 2.1, we define a set of conserved quantities $(\rho^*, \hat{u}_i, \tau^*)$ such that

$$\rho^* = \sqrt{\gamma}\rho W, \tag{2.12}$$

$$\hat{u}_i = h u_i = h W v_i, \tag{2.13}$$

$$\tau^* = hW - \frac{p}{\rho W} - \sqrt{1 + \gamma^{ij}\hat{u}_i\hat{u}_j}. \tag{2.14}$$

It is straightforward to relate ρ^* and $\hat{u}_i$ to D and S_i, while τ^* and τ differ more due to the kinetic term $\varpi = \sqrt{1 + \gamma^{ij}\hat{u}_i\hat{u}_j}$. The underlying reason is that evolving τ^* with the SPH code produces better results in regions where the kinetic energy is the dominant contribution to the total energy. Note that τ^* is defined slightly differently than in [219] to improve numerical stability. This modification dates back to early studies with the code [48].

Taking into account that SPH is a Lagrangian approach, the time derivative operator $\frac{d}{dt}$ is related to the (Eulerian) time derivative ∂_0 as $\frac{d}{dt} = \partial_0 + \frac{u^i}{u^0}\partial_i$. The system of differential equations for $(\rho^*, \hat{u}_i, \tau^*)$, namely the hydrodynamic evolution equations, then reads

$$\frac{d\rho^*}{dt} = -\rho^*\partial_i\left(\frac{u^i}{u^0}\right), \tag{2.15}$$

$$\frac{d\hat{u}_i}{dt} = -\frac{1}{\rho^*}\alpha\psi^6\partial_i p - \alpha\hat{u}^0\partial_i\alpha + \hat{u}_j\partial_i\beta^j + \frac{2\hat{u}_j\hat{u}_j}{\psi^5\hat{u}^0}\partial_i\psi, \tag{2.16}$$

$$\begin{aligned}\frac{d\tau^*}{dt} = &-\frac{\psi^6}{\rho^*}\alpha v^i\left(1 - \frac{hW}{\varpi}\right)\partial_i p - \psi^6\frac{p}{\rho^*}\partial_i\left(\alpha v^i\right)\\ &- 6\psi^5\frac{p}{\rho^*}\alpha v^i\partial_i\psi - \frac{\hat{u}_i}{\psi^4}\left(1 - \frac{hW}{\varpi}\right)\partial_i\alpha\\ &+ \frac{1}{\psi^4}\left(\frac{1}{hW} - \frac{1}{\varpi}\right)\left(\hat{u}_i\hat{u}_j\partial_j\beta^i - \frac{1}{3}\hat{u}_i\hat{u}_i\partial_j\beta^j\right),\end{aligned} \tag{2.17}$$

where the conformal flatness condition is imposed, namely $\gamma_{ij} = \psi^4\delta_{ij}$ in Cartesian isotropic coordinates, where ψ is the conformal factor (see Section 2.4 for more details).

Due to the differentiable nature of Eq. (2.11), spatial derivatives can be computed by direct differentiation, without the need for a finite difference method. This is an important aspect of SPH, because the hydrodynamic evolution equations (i.e. Eqs. (2.15)-(2.17)) become a set of ordinary differential equations in time. Similarly to fixed-grid finite volume methods, a standard numerical integration scheme can be employed for the time integration. In particular, the code employs a fourth-order Runge-Kutta method and determines the time step based on the CFL condition.

In order to accurately treat shocks SPH requires an artificial viscosity scheme [212, 251–253]. The implementation in the code is outlined in [219]. The principal idea is to consider each particle pair as the “left” and “right” state of a local Riemann problem, similar in spirit to the discussion in Section 2.2.

Furthermore, we note that the SPH code includes support for analytic EOSs (i.e. ideal gas), zero-temperature microphysical EOSs supplemented by an ideal gas thermal component (see Section 2.6), as well as full temperature- and composition-dependent EOSs of the form $p(\rho, \epsilon, Y_e)$, where Y_e is the electron fraction.

Similarly to fixed-grid Eulerian approaches, Eqs. (2.12)-(2.14) highlight that the conversion from $(\rho^*, \hat{u}_i, \tau^*)$ to the primitive variables requires a numerical approach. On the contrary, SPH does not require the inclusion of an artificial atmosphere to treat vacuum regions. Furthermore, fixed-grid approaches require the implementation of (adaptive) mesh refinement techniques to locally increase or decrease the spatial resolution throughout a simulation. The discretization via particles, which comove with the fluid, on its own guarantees adaptive resolution, thus making SPH an excellent choice for many astrophysical problems.

2.4. Conformal flatness approximation

For the description of the spacetime, we adopt the ADM formalism, which leads to the metric element (2.1). In addition, we employ the CFC approach [157,312], which approximates the spatial 3−metric as

$$\gamma_{ij} = \psi^4 \hat{\gamma}_{ij}, \tag{2.18}$$

where $\hat{\gamma}_{ij}$ is the flat metric. The metric solver employs Cartesian isotropic coordinates, thus $\hat{\gamma}_{ij} = \delta_{ij}$.

Employing the maximal slicing condition $\mathrm{tr}K_{ij} = 0$, where K_{ij} is the extrinsic curvature, the Einstein field equations reduce to a set of five coupled nonlinear elliptic differential equations for the metric components (e.g. [36])

$$\Delta\psi = - 2\pi\psi^5 E - \frac{1}{8}\psi^5 K_{ij}K^{ij}, \tag{2.19}$$

$$\Delta(\alpha\psi) = 2\pi\alpha\psi^5(E + 2S) + \frac{7}{8}\alpha\psi^5 K_{ij}K^{ij}, \tag{2.20}$$

$$\Delta\beta^i = - \frac{1}{3}\partial^i\partial_j\beta^j + 2\psi^{10}K^{ij}\partial_j\left(\frac{\alpha}{\psi^6}\right) + 16\pi\alpha\psi^4 S^i, \tag{2.21}$$

where

$$E = \rho h \left(au^0\right)^2 - p, \tag{2.22}$$

$$S = \rho h \left[\left(au^0\right)^2 - 1\right] + 3p, \tag{2.23}$$

are matter contribution to the source terms, while $S^i = \rho h \alpha u^0 u^\mu \gamma^i_\mu$ are the contravariant components of S_i defined in Eq. (2.7).

The extrinsic curvature, under the conformal flatness assumption, depends on the metric as

$$K_{ij} = \frac{\psi^4}{2\alpha}\left(\delta_{ik}\partial_j\beta^k + \delta_{jk}\partial_i\beta^k - \frac{2}{3}\delta_{ij}\partial_k\beta^k\right). \tag{2.24}$$

The equation for β^i can be cast into two Poisson-like differential equations through the definition $\beta^i = B^i - \frac{1}{4}\partial_i\chi$ [36]. The differential equations for B^i and χ read

$$\Delta B^i = 2\psi^{10}K^{ij}\partial_j\left(\frac{\alpha}{\psi^6}\right) + 16\pi\alpha\psi^4 S^i, \tag{2.25}$$

$$\Delta\chi = \partial_i B^i. \tag{2.26}$$

In the metric solver implementation, the equations for ψ, $\alpha\psi$, B^i and χ are discretized on a Cartesian uniform grid. A multipole expansion up to quadrupole order provides boundary conditions for Eqs. (2.19) and (2.20). Fall-off boundary conditions are imposed for Eqs. (2.25) and (2.26). The equations are then solved iteratively until they converge employing a multigrid approach [63]. The metric solver implementation was originally introduced in [220].

The CFC approximation ignores off-diagonal spatial metric terms. Hence, it omits gravitational waves. In order to extract the gravitational wave signal and include the backreaction to matter, a small, non-conformally flat correction to the metric is added. The scheme was derived in [113], while elements of the calculation can be found in [60]. This approach leads to post-merger gravitational wave frequencies, black-hole formation, ejecta and torus masses which are in good agreement with full general relativistic simulations of BNS systems [41, 43, 45, 173]. More details on any aspect of the metric solver implementation can be found in [219].

Finally, we note that we employ almost identical metric modules to treat gravity in the SPH code and AREPO[1]. However, the coupling between the metric and the hydrodynamics modules of the two codes differs. From the purely technical point of view, the SPH code (hydrodynamic and metric modules) is written in Fortran and parallelized with OpenMP. AREPO on the other hand is written in C and employs the MPI protocoll for parallelization. So the communication and synchronization between AREPO and the metric modules is more challenging. Furthermore, modelling the interaction of the fluid with the spacetime requires mapping hydrodynamic data from the SPH particles or AREPO cells to the metric grid points and vice versa. Regarding the first direction, SPH provides a native interpolation method. In the case of AREPO, the situation is different and we provide more details in Section 3.6. Mapping metric fields to any point (e.g. SPH particle or cell center positions) is easier because the metric is known on a uniform Cartesian grid (see Section 3.6 for more details on how it is done in AREPO).

2.5. Perturbative approach

In the previous sections, we discussed a formulation and numerical approaches which allow for a full 3D dynamical study of NS systems. Such simulations are rather demanding computationally, which made them practically impossible in early studies of the system. Another powerful tool, which has been and is still being used extensively to study certain aspects of the system, is perturbation theory (see e.g. [172] and references therein).

The perturbative approach considers an equilibrium state of the system as the background solution. In the case of static, spherically symmetric NSs, this requires to solve the TOV equations. Without loss of generality, the background metric in Schwarzschild coordinates is written as

$$ds^2 = -e^{2\nu(r)}dt^2 + e^{2\lambda(r)}dr^2 + r^2(d\theta^2 + \sin^2\theta d\phi^2), \tag{2.27}$$

where $\nu(r)$ is a metric potential and $e^{2\lambda(r)} = \left(1 - \frac{2m(r)}{r}\right)^{-1}$ with $m(r)$ the gravitational

---

[1] The main difference is that, in the case of the SPH code, some metric grid related operations are carried out at the level of particles, while in AREPO we opt to map and compute everything on the metric grid.

mass inside a radial distance r. We highlight that this ansatz for the metric is only relevant for the discussion on perturbative methods. The modeling of the spacetime for the 3D codes discussed in this thesis is outlined in Section 2.4.

In order to model small perturbations in the fluid and the spacetime, the perturbed Einstein equations and the variation of the energy-momentum tensor conservation need to be solved, i.e.

$$\delta\left(G^{\mu\nu} - 8\pi T^{\mu\nu}\right) = 0, \tag{2.28}$$

$$\delta\left(\nabla_\mu T^{\mu\nu}\right) = 0, \tag{2.29}$$

where $G^{\mu\nu}$ is the Einstein tensor.

In principle, we can consider perturbations up to an arbitrary order in a perturbation parameter. However, the problem becomes quite difficult already at second order [64, 128]. Hence, we focus our attention to first-order perturbations. Linear perturbations ignore mode couplings and thus do not capture the full dynamics of the system. Nevertheless, they are successful in computing the frequencies of both fluid and spacetime oscillations for various types of perturbations and they are extremely useful in better understanding the basic dynamics of the system.

In the following, we examine two different types of oscillations, the radial mode and the $f-$mode. Our main motivation behind studying radial pulsations is that they constitute a standard test for 3D general relativistic hydrodynamic codes. We present such tests with Arepo in Chapter 4. For additional flexibility in these tests, we developed a code to compute radial modes which supports the polytropic EOS, as well as zero-temperature microphysical EOSs in the form of piecewise polytropes [246].

In Chapter 6 we examine the accuracy of universal relations between $f-$mode frequencies and stellar parameters. Furthermore, we consider the main gravitational wave frequency from the post-merger phase of BNS merger remnants. We try to identify possible EOS signatures in the post-merger signal. A number of arguments support that the dominant frequency is produced by the $f-$mode oscillation in the remnant [49, 53, 67, 276]. For this reason, we employ also perturbative calculations of the $f-$mode for zero-temperature microphysical EOSs, provided in tabulated form, to further investigate EOS effects in a simpler system. We extract post-merger frequencies with the SPH code discussed in Section 2.3 (see [45, 48, 219, 220] for more details), while we obtain perturbative $f-$mode frequencies with the code presented in [198].

2.5.1. Radial mode

The radial pulsation equations were derived in [69]. Since then various different formulations have been proposed in the literature (e.g. [72, 131, 171]). We follow [131] because their formulation is singularity-free at the surface and also does not contain derivatives of the adiabatic index Γ (see relevant discussion in [131]), which makes it easier to apply to piecewise polytropic EOSs.

The functional form of the perturbations should preserve the spherical symmetry of the background solution. Furthermore, we assume a harmonic time dependence for all perturbations. If we denote the radial displacement of a fluid element, located at a distance r in the background solution, as $\Delta r(r,t)$, we can explicitly decompose Δr as e.g.

$$\Delta r(r,t) = G(r)e^{i\omega t}, \tag{2.30}$$

where $G(r)$ is the radial dependence, which remains to be determined. The remaining perturbed variables are treated in the same way, i.e. $\Delta p(r,t) \propto e^{i\omega t}$, etc.

The system of differential equations governing radial oscillations then reads

$$\frac{d\xi}{dr} = -\frac{1}{r}\left(3\xi + \frac{\Delta p}{\Gamma p}\right) - \frac{dp}{dr}\frac{\xi}{\varepsilon + p}, \tag{2.31}$$

$$\begin{aligned} \frac{d(\Delta p)}{dr} =& \xi\left[\omega^2 e^{2(\lambda-\nu)}(\varepsilon+p)r - 4\frac{dp}{dr}\right] \\ &+ \xi\left[\left(\frac{dp}{dr}\right)^2 \frac{r}{\varepsilon+p} - 8\pi e^{2\lambda}(\varepsilon+p)pr\right] \\ &+ \Delta p\left[\frac{dp}{dr}\frac{1}{\varepsilon+p} - 4\pi e^{2\lambda}(\varepsilon+p)r\right], \end{aligned} \tag{2.32}$$

where $\xi = \Delta r/r$ is the relative radial displacement and $\varepsilon = \rho(1+\epsilon)$ is the total energy density.

Solving the equations requires boundary conditions. In order to ensure that Eq. (2.31) is regular at the center and due to the normalization of eigenfunctions, it follows that

$$(\Delta p)_c = -3(\xi \Gamma p)_c, \tag{2.33}$$

$$\xi_c = 1, \tag{2.34}$$

where we use c to denote that these relations hold at the stellar center. Moreover, the pressure at the surface of the star by definition drops to zero, which results in

$$(\Delta p)_R = 0, \tag{2.35}$$

where R is the stellar radius.

In order to solve the equations, we employ the boundary conditions (2.33) and (2.34) to integrate from the center to the surface for a trial value of the frequency ω. Determining the spectrum of eigenvalues ω^2 for a particular stellar model translates to tracking down the values of ω^2 which satisfy the boundary condition (2.35). The spectrum contains an infinite number of eigenvalues ω_n^2. Furthermore, we note that $\omega^2 > 0$ holds for real values of ω, while $\omega^2 < 0$ means that ω is imaginary. If the spectrum contains only positive eigenvalues, namely $\omega_n^2 > 0\ \forall n$, the solution is purely oscillatory and the configuration is stable. On the contrary, if the spectrum contains at least one negative eigenvalue, the corresponding frequency is imaginary. Based on the harmonic time dependence assumption the perturbation is now exponentially growing. As a result, the configuration is unstable. The maximum mass stable model for a given EOS is directly related to the instability under radial perturbations [142].

2.5.2. Quadrupole mode

Quadrupole oscillations produce gravitational waves. As a consequence, it does not suffice to study only the NS interior, but we also need to model the perturbed spacetime outside the star as well. We start the discussion from the study of the quadrupole mode in the interior of NSs. A number of works investigated the problem of nonradial oscillations in NSs [66, 156, 237, 285–287]. We adopt the formulation from [91], which builds on top of earlier work [193]. For extensive reviews on the topic see [121, 172].

The symmetries of the background allow us to decompose the perturbations into a sum of quasi-normal modes, which correspond to different spherical harmonics. The angular part of scalar, vector and tensor quantities is represented with scalar, vector and tensor spherical harmonics, respectively. Furthermore, we assume a harmonic time dependence for all perturbations, where the frequency

$$\omega = 2\pi f + \frac{i}{\tau_{\text{damp}}} \tag{2.36}$$

is now complex. The real part is the frequency of the oscillation f, while τ_{damp} is the damping timescale due to gravitational waves.

We can then expand perturbations, e.g. the Lagrangian perturbation of the pressure Δp, as

$$\Delta p(t,r,\theta,\phi) = r^l \Delta p^{lm}(r) Y_{lm} e^{i\omega t}, \tag{2.37}$$

where $\Delta p^{lm}(r)$ is the radial part of the perturbation and Y_{lm} are the spherical harmonics. We focus on the $(l,m)=(2,0)$ mode.

Based on [91], in order to determine all the perturbation functions (e.g. $\Delta p^{lm}(r)$), we need to solve a system of four first-order differential equations which read

$$\begin{aligned}
\frac{dH_1^{lm}}{dr} =& -\frac{1}{r}\left[l+1+\frac{2me^{2\lambda}}{r}+4\pi r^2 e^{2\lambda}(p-\varepsilon)\right]H_1^{lm} \\
&+\frac{e^{2\lambda}}{r}\left[H_0^{lm}+K^{lm}-16\pi(\varepsilon+p)V^{lm}\right], && (2.38)\\
\frac{dK^{lm}}{dr} =& \frac{1}{r}H_0^{lm}+\frac{l(l+1)}{2r}H_1^{lm}-\left[\frac{l+1}{r}-\frac{d\nu}{dr}\right]K^{lm}-8\pi(\varepsilon+p)\frac{e^{\lambda}}{r}W^{lm}, && (2.39)\\
\frac{dW^{lm}}{dr} =& -\frac{l+1}{r}W^{lm}+re^{\lambda}\left[\frac{e^{-\nu}}{c_s^2(\varepsilon+p)}X^{lm}-\frac{l(l+1)}{r^2}V^{lm}+\frac{1}{2}H_0^{lm}+K^{lm}\right], && (2.40)\\
\frac{dX^{lm}}{dr} =& -\frac{l}{r}X^{lm}+\frac{(\varepsilon+p)e^{\nu}}{2}\left\{\left(\frac{1}{r}-\frac{d\nu}{dr}\right)H_0^{lm}+\left(r\omega^2e^{-2\nu}+\frac{l(l+1)}{2r}\right)H_1^{lm}\right. \\
&+\left(3\frac{d\nu}{dr}-\frac{1}{r}\right)K^{lm}-\frac{2l(l+1)}{r^2}\frac{d\nu}{dr}V^{lm} \\
&\left.-\frac{2}{r}\left[4\pi(\varepsilon+p)e^{\lambda}+\omega^2e^{\lambda-2\nu}-\frac{r^2}{2}\frac{d}{dr}\left(\frac{2e^{-\lambda}}{r^2}\frac{d\nu}{dr}\right)\right]W^{lm}\right\}, && (2.41)
\end{aligned}$$

where c_s the speed of sound, while $H_1^{lm}(r)$, $K^{lm}(r)$ refer to spacetime perturbations and $W^{lm}(r)$, $X^{lm}(r)$ to fluid perturbations. The functions $H_0^{lm}(r)$, $V^{lm}(r)$ can be directly related to H_1^{lm}, K^{lm}, W^{lm} and X^{lm}. Once we determine this set of four functions $(H_1^{lm}, K^{lm}, W^{lm}, X^{lm})$, we can express all the spacetime and fluid perturbations in the interior of the star with respect to them (e.g. $\Delta p^{lm} = e^{\nu}X^{lm}$) [91,193,287].

Eqs. (2.38)-(2.41) are singular near the center. Hence, their solution is approximated based on a second-order expansion near $r=0$. The lowest-order term of the expansion provides constraints for H_1^{lm} and X^{lm} at $r=0$, which means the solution from the center is the combination of two linearly independent bounded solutions at $r=0$. We pick two sets of linearly independent boundary conditions for (K^{lm}, W^{lm}) and employ the expansion to compute the two solutions close to the center. We then integrate outwards to extend both solutions up to some point $r_* \approx 0.2R$. In addition, we have a single boundary condition at the surface, $X^{lm}(R)=0$, since the pressure should vanish. As a result, at the surface, the unique solution is a linear combination of three linearly independent solutions which satisfy this condition. We pick three sets of linearly independent boundary conditions for $(H_1^{lm}, K^{lm}, W^{lm})$ and integrate them inwards up to r_*. At $r = r_*$ we match the linear combination of the two solutions from the center to the linear combination of the three solutions from the surface in order to determine a single solution for the system, which is unique up to a multiplication factor. For more details see [91, 193].

In order to compute the frequencies ω, we need to study the exterior of the NS as well. In the vacuum, the fluid perturbations vanish, so only the spacetime perturbations are relevant. The perturbation functions H_1^{lm} and K^{lm} can be combined into a single function called the Zerilli function, which satisfies a second-order differential equation known as the Zerilli equation [109, 319]. In order to solve the equation, the Zerilli function and its first derivative are matched to the interior solution at the surface. For a general value of ω, the Zerilli function behaves as the sum of an ingoing and an outgoing wave at infinity. The eigenvalues ω^2 correspond to the discrete set of ω for which the solution at infinity is purely outgoing, namely no incoming gravitational radiation drives the oscillation.

In our code, we adopt a different formulation for the exterior problem which was presented in [23]. The problem is reformulated to obtain a differential equation with a significantly less oscillatory solution than the Zerilli equation. The differential equation which we need to solve reads

$$\frac{1}{2q}\frac{d^2q}{dr^2} - \frac{3}{4q^2}\left(\frac{dq}{dr}\right)^2 + q^2 - U(r) = 0. \tag{2.42}$$

Here $q(r)$ is a function related to the perturbations (see [23]), while

$$U(r) = \left(1 - \frac{2M}{r}\right)^{-2}\left[\omega^2 - V_z(r) + \frac{2M}{r^3} - \frac{3M^2}{r^4}\right], \tag{2.43}$$

where M the stellar mass and $V_z(r)$ an effective potential given by

$$V_z(r) = e^{-2\lambda}\frac{2n^2(n+1)r^3 + 6n^2Mr^2 + 18nM^2r + 18M^3}{r^3(nr+3M)^2}, \tag{2.44}$$

with $n = (l-1)(l+2)/2$.

The value of the potential $U(r)$ does not vary significantly at $r \to \infty$. Hence, we neglect the derivative terms in Eq. (2.42) at infinity and approximate the solution as $q(r) \approx \sqrt{U(r)}$. We employ this expression to construct initial conditions for integrating Eq. (2.42). The overall procedure is described in more detail in [23].

2.6. Equation of state

An important part of the description of NSs, as well as one of the main reasons for which we study the system, is the nuclear EOS. NSs reach densities of a few times the nuclear saturation density ρ_{sat}, while binary neutron star mergers can also reach temperatures of several tens of MeV or possibly even more. However, the EOS of ordinary matter at densities above ρ_{sat} is quite uncertain [65, 138, 221]. Terrestrial experiments involving nuclei set constraints up to roughly ρ_{sat}, while heavy-ion collisions provide additional information for hot, approximately symmetric nuclear matter up to a few times $\rho_{\rm sat}$ [179, 180, 221, 226]. A number of different microphysical models and nuclear parametrizations exist to model matter behavior at such high densities (see e.g. [65, 114, 138, 221]). Throughout this study we employ a number of different EOSs. We refrain from explicitly discussing each EOS and instead provide references to the works in which every individual EOS was introduced and is described in detail.

In order to accurately simulate BNS mergers we need EOSs which cover the whole range of thermodynamic conditions in the post-merger phase, i.e. densities up to a few times $\rho_{\rm sat}$, temperatures which can exceed 100 MeV and also an excess of neutrons over protons. A number of such EOSs with full temperature dependence, which also cover a range of electron fractions, exist[2]. Moreover, the significantly greater number of available EOSs for cold (zero-temperature) matter in neutrino-less beta-equilibrium can also be complemented by an ideal gas to approximate thermal effects [159]. The full "hybrid" EOS reads

$$p = p_{\rm cold} + p_{\rm th}, \tag{2.45}$$

$$\epsilon = \epsilon_{\rm cold} + \epsilon_{\rm th}, \tag{2.46}$$

where $p_{\rm cold} = p_{\rm cold}(\rho)$ and $\epsilon_{\rm cold} = \epsilon_{\rm cold}(\rho)$ refer to the microphysical cold EOS in beta-equilibrium, while $p_{\rm th}$ and $\epsilon_{\rm th}$ describe the thermal part. The hydrodynamic evolution determines ρ and ϵ. Then, $\epsilon_{\rm th} = \epsilon - \epsilon_{\rm cold}(\rho)$ and the thermal pressure is given by

$$p_{\rm th} = (\Gamma_{\rm th} - 1)\rho\epsilon_{\rm th}, \tag{2.47}$$

where typical values for the adiabatic constant $\Gamma_{\rm th}$ lie in the range $1.5 - 2$ (see [46] for a detailed discussion).

In addition to microphysical EOSs, one can also employ an analytic EOS to model NSs. A typical choice is the polytropic EOS which reads

$$p = K\rho^{\Gamma}, \tag{2.48}$$

where K is the polytropic constant and Γ the polytropic index.

Modelling NSs as polytropes is not very precise, because the two available parameters are not enough to accurately describe the whole density range realized within NSs. Nevertheless, simulations with polytropes still capture part of the dynamics, especially for configurations that are close to equilibrium. Furthermore, evolving (isentropic) polytropes is less computationally demanding, mainly because the specific internal energy follows analytically from the density as

$$\epsilon = \frac{K\rho^{\Gamma-1}}{(\Gamma - 1)}, \tag{2.49}$$

which eliminates the need to evolve the hydrodynamic equation for τ.

Evolutions with the (isentropic) polytropic EOS fail to capture a number of dynamical processes, such as shocks. An ideal gas EOS instead provides a more physical description of the system. Hence, in some of our AREPO tests we construct initial data with the polytropic EOS and then employ

$$p = (\Gamma - 1)\rho\epsilon, \tag{2.50}$$

throughout the evolution. In this case, both ρ and ϵ follow from solving the GRHD equations.

---

[2] For clarification, we employ EOSs with full temperature and composition dependence only in the resuls presented in Chapter 6. We briefly summarize the microphysics modules currently implemented in AREPO in Section 3.8, based on the discussion presented in the current section.

Part II

General relativistic moving-mesh hydrodynamics with AREPO

Preface

Introductory and concluding remarks for the results discussed in Chapters 3, 4 and 5 can be found in Sections 1.2 and 7.1, respectively. Chapter 2 provides more details on the theoretical formulation and the numerical modeling. The bulk of this study follows [196][1], submitted to *Monthly Notices of the Royal Astronomical Society*. The text, figures and tables have been modified and adapted to suit this thesis.

---

[1] `https://arxiv.org/abs/2208.04267`

3. Moving-mesh hydrodynamics for general relativistic systems

3.1. Voronoi mesh in the Arepo code

In this study we employ the Arepo code [273]. Arepo solves hydrodynamics on a moving mesh. The basis of the moving-mesh construction is a discrete set of mesh-generating points. For a given set of points, the code constructs a so-called Voronoi tessellation. Each mesh-generating point corresponds to a different Voronoi cell. By definition, each Voronoi cell contains the region of space which is closer to its respective generating point than any other point. As a result, the Voronoi tesselation decomposes space into a set of discrete cells. This enables a finite volume formulation of the (general relativistic) hydrodynamic equations on a Voronoi mesh (see Section 3.2).

Arepo constructs the Voronoi tessellation by first creating a so-called Delaunay tessellation corresponding to the set of mesh-generating points. The Delaunay tessellation is the topological dual of the Voronoi diagram and computationally less expensive to generate. It is a specific triangulation of space where the points serve as vertices to form tetrahedra in 3D. The defining property of the Delaunay triangulation is that the circumsphere of each tetrahedron does not contain any of the remaining mesh-generating points. For more details on how to compute the Delaunay tesselation, see [273] and references therein.

As soon as the Delaunay tesselation is available, one can extract the Voronoi mesh. In particular, the mid-points of the circumspheres around each tetrahedron correspond to the vertices of the Voronoi cells. Based on the defining properties of the Voronoi mesh, one can compute the geometric characteristics of each Voronoi cell, i.e. the cell's center of mass and volume, as well as the face area between neighbouring cells. In principle, cell centers do not coincide with the positions of the mesh-generating points except for special cases, such as the Cartesian mesh.

The moving nature of the mesh originates from the fact that the mesh-generating points can move freely, which leads to a new mesh construction in each time step. The velocities of mesh-generating point can be chosen arbitrarily. Point motion changes the Voronoi mesh in a continuous way, which ensures that no mesh-tangling problems occur throughout the mesh evolution. For more details on the initial point distribution and motion, see Section 3.7.

3.2. Time integration

The original implementation of Arepo solves Newtonian hydrodynamics. However, the aim of this thesis is to simulate general relativistic systems with the moving-mesh approach. This requires extending the code with two main components, the necessary modules to solve the GRHD equations (i.e. Eqs. (2.6)) and a solver for the dynamical spacetime (see Sections 2.4 and 3.6). In this section we describe how we discretize the GRHD equations in a finite volume fashion and integrate in time to update the state of the system. Our basis version of the code includes the upgrades described in [232].

In Section 2.2 we present the outline of finite volume methods in GR. It was shown in [273] that the hydrodynamics equations can be discretized on an unstructured Voronoi mesh and solved in a moving-mesh fashion. For each cell i we define the volume integrated conserved variables as

$$\mathbf{Q}_i = \int_{V_i} \boldsymbol{\mathcal{U}} dV. \tag{3.1}$$

Arepo employs Heun's method for time integration, i.e. to update the state $\mathbf{Q}_i^n$ from time t^n to $t^{n+1} = t^n + \Delta t$, where Δt is the time step [232]. Heun's method is a second-order Runge-Kutta method which computes the time-updated state $\mathbf{Q}_i^{n+1}$ as

$$\begin{aligned}\mathbf{Q}_i^{n+1} =& \mathbf{Q}_i^n - \frac{\Delta t}{2}\left(\sum_j A_{ij}^n \hat{\mathbf{F}}_{ij}^n(\mathbf{W}_{ij}^n, \mathbf{W}_{ji}^n) + \sum_j A'_{ij} \hat{\mathbf{F}}'_{ij}(\mathbf{W}'_{ij}, \mathbf{W}'_{ji})\right) \\ &+ \frac{\Delta t}{2}\left(\boldsymbol{\mathcal{S}}_i^n + \hat{\boldsymbol{\mathcal{S}}}'_i\right), \qquad (3.2)\\ \mathbf{r}_i^{n+1} =& \mathbf{r}_i^n + \frac{\Delta t}{2}\left(\mathbf{w}_i^n + \mathbf{w}'_i\right). \qquad (3.3)\end{aligned}$$

Here $\mathbf{r}_i$ are the coordinates of the mesh-generating point for cell i and $\mathbf{w}_i$ is the point's velocity. Eq. (3.3) describes how the mesh changes during the time step. Focusing on Eq. (3.2), the index j accounts for all the neighbouring cells of cell i, while A_{ij} is the oriented interface area between cells i and j. $\hat{\mathbf{F}}_{ij}$ is an approximate Riemann solver estimate for the fluxes through the interfaces, which depends on the reconstructed primitives from the center of cell i (or j respectively) to the cell interfaces denoted by $\mathbf{W}_{ij}$ (or $\mathbf{W}_{ji}$ respectively) (see also Sections 3.3 and 3.4). $\boldsymbol{\mathcal{S}}_i = \int_{V_i} \mathbf{S} dV$ are the volume-integrated source terms computed for cell i. Primed quantities are explained in Eqs. (3.4) and (3.5).

Heun's method consists of two substeps, as can be seen in Eqs. (3.2) and (3.3). The two substeps require information at the beginning and the end of the time step, respectively. The input for the second substep follows from a forward Euler integration[1] which reads

$$\begin{aligned}\mathbf{Q}'_i =& \mathbf{Q}_i^n - \Delta t \sum_j A_{ij}^n \hat{\mathbf{F}}_{ij}^n(\mathbf{W}_{ij}^n, \mathbf{W}_{ji}^n) + \Delta t \boldsymbol{\mathcal{S}}_i^n, \qquad (3.4)\\ \mathbf{r}'_i =& \mathbf{r}_i^n + \Delta t \mathbf{w}_i^n. \qquad (3.5)\end{aligned}$$

Based on the estimates $\mathbf{Q}'_i$, we compute the fluxes $\hat{\mathbf{F}}'_{ij}$ and source terms $\hat{\boldsymbol{\mathcal{S}}}'_i$ at the end of the time step.

Formally, Heun's method requires two different mesh constructions for $\mathbf{r}_i^n$ and $\mathbf{r}'_i$. Arepo imposes that the mesh-generating point velocity remains constant during the whole time step, i.e. $\mathbf{w}'_i = \mathbf{w}_i^n$. Then

$$\mathbf{r}_i^{n+1} = \mathbf{r}_i^n + \frac{\Delta t}{2}\left(\mathbf{w}_i^n + \mathbf{w}'_i\right) = \mathbf{r}_i^n + \Delta t \mathbf{w}_i^n = \mathbf{r}'_i, \tag{3.6}$$

---

[1] Note that the Newtonian version of Arepo follows a different approach [232].

which means that the mesh which was constructed for the second substep of Heun's method in the current time step can be reused in the first substep of the next time step, i.e. in Eq. (3.2) $A'_{ij} = A^{n+1}_{ij}$. Hence, only one mesh construction is necessary per time step, which reduces the computational effort.

We update the metric at the beginning of each Heun substep. We solve the metric field equations in both substeps of Heun's method in the nine first time steps and, subsequently, in the first substep of every fifth time step. In all other substeps we estimate the metric based on a parabolic extrapolation using the last three metric solutions, which reduces the required computational effort. Explicitly calling the metric solver in the initial timesteps is necessary to obtain the required metric solutions for the extrapolation, as well as guarantee the stability of the scheme after importing initial data. We find this approach to be in excellent agreement with solving the field equations in every substep, provided that the metric fields do not vary significantly between successive time steps. The frequency with which we call the metric solver can be adjusted to the problem in hand based on the time step Δt.

Evolving the system requires to determine the time step Δt. For each cell with volume V_i, we compute the maximum allowed time step Δt_i as

$$\Delta t_i = C_{\text{CFL}} \frac{R_i}{|\lambda_i^{\max}|}, \tag{3.7}$$

where $R_i = (3V_i/(4\pi))^{1/3}$ is an effective cell radius and $\lambda_i^{\max}$ is the maximum eigenvalue of the Jacobian of the GRHD equations (see [35]) for this particular cell. Moreover, we apply the CFL condition with a CFL factor C_{CFL}, which we typically set to 0.3.

Arepo can update cell states based on a global time step or consider individual time steps for each cell based on a power-of-two hierarchy to achieve synchronization (see [273, 308] for more details). In our implementation we opt for a global time step defined as

$$\Delta t = \frac{T_{\text{tot}}}{2^N}, \tag{3.8}$$

where T_{tot} is the total simulation time and N is the smallest integer which satisfies $\Delta t < \min_i \Delta t_i$. The total simulation time T_{tot} can be chosen freely.

3.3. Primitive variables reconstruction

Arepo approximates any quantity ϕ within a cell linearly as

$$\phi(\mathbf{r}) = \phi(\mathbf{s}_i) + \langle \nabla \phi \rangle_i \cdot (\mathbf{r} - \mathbf{s}_i), \tag{3.9}$$

where $\mathbf{s_i}$ is the position of the cell's center of mass, $\mathbf{r}$ any other point within the cell and $\langle \nabla \phi \rangle_i$ is an estimate for the gradient of ϕ in cell i. To compute $\langle \nabla \phi \rangle_i$ in each cell, the code relies on the fact that we know the value of ϕ at the center of mass of all the cells. Moreover, for any cell j which is a neighbour of cell i, we can estimate ϕ at its center of mass $\mathbf{s}_j$ based on Eq. (3.9) as

$$\phi_j^{\text{est}} = \phi(\mathbf{s}_i) + \langle \nabla \phi \rangle_i \cdot (\mathbf{s_j} - \mathbf{s}_i). \tag{3.10}$$

To determine the gradient $\langle \nabla \phi \rangle_i$ we demand that the estimate ϕ_j^{est} is accurate. In particular, we employ a least-squares method to minimize the weighted sum of the deviations over all neighbouring cells of cell i

$$\sum_j g_j \left(\phi(\mathbf{s}_j) - \phi_j^{\text{est}}\right)^2 , \tag{3.11}$$

where $g_j = A_{ij}/|\mathbf{s}_i - \mathbf{s}_j|^2$ (see [232] for more details). Based on the gradient estimate $\langle \nabla\phi \rangle$ we can directly employ Eq. (3.9) to reconstruct primitives to the mid-points of the faces.

Alternatively, we can apply a slope limiter to the gradient estimate to construct a total variation diminishing scheme. We adopt the approach presented in [87] for the extension of slope limiters to unstructured grids (see also [229]). We denote the cells associated with a face as left (L) and right (R). To extrapolate a primitive variable from the center of mass of the left cell to the interface, the method relies on the scalar

$$r_L = \frac{\nabla\phi_L \cdot \mathbf{s}_{LR}}{\phi_R - \phi_L} - 1, \tag{3.12}$$

where $\nabla\phi_L$ is the gradient of ϕ at the center of mass of the left cell, $\mathbf{s}_{LR}$ is the vector from the center of the left cell to the center of the right cell and ϕ_L, ϕ_R are the values of the primitive variable at the center of the left and right cells, respectively. Then, the reconstructed value of the primitive variable from the left cell to the interface is given by

$$\phi_L^{\text{face}} = \phi_L + \frac{1}{2}\Psi(r)(\phi_R - \phi_L), \tag{3.13}$$

where $\Psi(r)$ is the slope limiter function. A similar process is followed to extrapolate from the center of the right cell to the interface.

Unless otherwise stated, in the simulations presented in this thesis we employ slope-limited reconstruction using the gradient estimate $\langle \nabla\phi \rangle$ computed in the left cell as the value of $\nabla\phi_L$. Various options for the slope limiter exist. Our choice is the MC slope limiter [299], because it performs better in simulations of single relativistic stars [116].

3.4. Riemann problem

In a moving-mesh approach the face between neighbouring cells is moving. To accurately resolve the Riemann problem at the face, we need to take this motion into account. The Newtonian version of Arepo considers the face motion by solving the Riemann problem in the rest-frame of the face. This requires boosting the cell states by the velocity of the face. The code then reconstructs the primitive variables at both sides of the mid-point of each face to construct the left (L) and right (R) states. After rotating the reconstructed states, such that they align with the normal vector of the face, a one-dimensional (1D) Riemann solver can be applied. The solution is rotated and boosted back to the original non-moving frame and the fluxes can now be computed. This process requires an estimate for the face's velocity, which the code approximates as

$$\tilde{\mathbf{w}} = \frac{\tilde{\mathbf{w}}_\text{R} + \tilde{\mathbf{w}}_\text{L}}{2} + \frac{(\tilde{\mathbf{w}}_\text{L} - \tilde{\mathbf{w}}_\text{R}) \cdot [\mathbf{f} - (\mathbf{r}_\text{R} + \mathbf{r}_\text{L})/2]}{|\mathbf{r}_\text{R} - \mathbf{r}_\text{L}|} \frac{(\mathbf{r}_\text{R} - \mathbf{r}_\text{L})}{|\mathbf{r}_\text{R} - \mathbf{r}_\text{L}|}, \tag{3.14}$$

where $\mathbf{r}_{\text{L/R}}$, $\tilde{\mathbf{w}}_{\text{L/R}}$ are the positions and velocities of the mesh-generating points associated with the respective face, while $\mathbf{f}$ is the position of the mid-point of the face. The first term is the average velocity of the two mesh-generating points, while the second term captures the residual motion due to the fact that the center of mass of the two points does not generally coincide with the mid-point of the face (see also [273]).

In our general relativistic implementation, we follow a different approach, which was introduced in [100], and solve the Riemann problem in the non-moving frame. We employ the HLLE solver [108, 146]. Because the face is moving with velocity $\tilde{\mathbf{w}}$, we sample the solution along the curve $x/t = \tilde{\mathbf{w}} \cdot \hat{\eta}$ in order to capture the correct HLLE state. Here $\hat{\eta}$ is the outward normal vector to the face. In contrast, in Eulerian codes the faces are not moving and the solution is sampled along the curve $x/t = 0$. The fluxes entering Eq. (3.2) then read

$$\hat{\mathbf{F}}_{ij} = \boldsymbol{\mathcal{F}}^{\rm 1D}_{ij} - \tilde{\mathbf{w}}_{ij} \cdot \hat{\eta} \boldsymbol{\mathcal{U}}^{\rm 1D}_{ij}, \tag{3.15}$$

where $\boldsymbol{\mathcal{F}}^{\rm 1D}_{ij}$ and $\boldsymbol{\mathcal{U}}^{\rm 1D}_{ij}$ are the HLLE fluxes and state vector, the indices i, j label the two cells which share the face and the advective (second) term appears due to the face's motion.

3.5. Primitive variables recovery

The time evolution equations are written for the set of volume integrated conserved variables $\mathbf{Q}$ (see Eq. (3.2)). Hence, at the end of the time step we know the variables $\mathbf{Q}$ from which we can directly extract the conserved variables $\mathbf{U}$. In contrast to Newtonian hydrodynamics, computing the primitive variables $\mathbf{W}$ from the set of conserved variables cannot be done analytically and a numerical recovery scheme is required.

We employ a rather common recovery scheme (see e.g. [249]). We start by defining

$$S^2 = \gamma^{ij} S_i S_j = (\rho h W)^2 (W^2 - 1), \tag{3.16}$$

$$Q = \tau + p + D = \rho h W^2. \tag{3.17}$$

It is then straightforward to show that

$$\rho = \frac{D\sqrt{Q^2 - S^2}}{Q}, \tag{3.18}$$

$$\epsilon = \left(\sqrt{Q^2 - S^2} - \frac{pQ}{\sqrt{Q^2 - S^2}} - D \right) \bigg/ D, \tag{3.19}$$

where it is evident that ρ and ϵ do not depend only on the conserved variables, but also on the pressure. The problem of converting the conserved to the primitive variables now translates to identifying the set of ρ, ϵ, p which satisfy the EOS. For a generic EOS of the form $p = p(\rho, \epsilon)$ this requires to solve the equation

$$p - \hat{p}\left[\rho\left(\mathbf{U}, p\right), \epsilon\left(\mathbf{U}, p\right)\right] = 0, \tag{3.20}$$

based on a root-finding scheme. Here p is the value which we wish to determine, while $\hat{p}\left[\rho\left(\mathbf{U}, p\right), \epsilon\left(\mathbf{U}, p\right)\right]$ is the value produced by the EOS based on the conserved variables and the (guess for the) pressure p. We employ a Newton-Rapshon method and use the pressure at the cell center in the previous time step as an initial guess to accelerate root-finding. The Newton-Rapshon method requires to compute the derivatives $\partial\hat{p}/\partial\rho$, $\partial\hat{p}/\partial\epsilon$, $\partial\rho/\partial p$ and $\partial\epsilon/\partial p$. We numerically differentiate the EOS to compute the first two derivatives, while the latter two are easy to compute analytically based on Eqs. (3.18) and (3.19).

To eliminate possible unphysical solutions, at the end of the Newton-Raphson step for each cell we check if $p < 0$. Moreover, we identify cells for which $\rho < \rho_{\mathrm{thr}}$, where ρ_{thr} is a threshold density related to the artificial atmosphere. In both cases, we set the primitive variables to atmosphere values and recompute the conserved variables based on the new primitives (see Section 3.8 for more details on the artificial atmosphere).

3.6. Voronoi mesh and metric grid coupling

Arepo solves the GRHD equations on an unstructured Voronoi mesh. The metric equations are solved iteratively on an independent uniform Cartesian grid, which covers the physical domain of interest (see Section 2.4 for more details). However, a number of hydrodynamical operations such as moving the mesh-generating points, computing the interface fluxes or recovering the primitive variables require knowledge of the metric fields at a number of different points, like the mesh-generating point positions, the center of mass of Voronoi cells or the mid-point of the interfaces between neighbouring cells. Similarly, in order to solve the metric field equations we need to know the values of the hydrodynamic variables at the positions of the metric grid points. Hence, we need to establish mapping techniques between the Voronoi mesh and the metric grid, which practically constitute the coupling between hydrodynamics and space time.

(i) *Metric grid to hydrodynamic mesh*: We know the metric fields on a uniform Cartesian grid. Hence, it is straightforward to interpolate to any position within the domain of the metric grid. At the moment, we employ a third-order Lagrange polynomial. For points which lie outside the metric grid limits we follow a different approach. We compute the metric fields at their position based on the multipole expansion and fall-off boundary conditions that we use to compute boundary conditions for Eqs. (2.19), (2.20) and (2.25), (2.26), respectively.

(ii) *Hydrodynamic mesh to metric grid*: Mapping from the Voronoi cells to the metric grid points is significantly more difficult due to the unstructured nature of the Voronoi mesh. We perform a tree walk [273] to identify which Voronoi cell lies closest to each metric grid point. The values of all necessary hydrodynamic variables are then directly passed from the Voronoi cell to the metric grid point. This is rather accurate, because hydrodynamic resolution is higher at physically important regions, i.e. currently regions with $\rho > \rho_{\mathrm{thr}}$. Naturally, increasing the hydrodynamic resolution, i.e. the number of mesh-generating points, improves the accuracy. In principle, this approach can be extended to account for the fact that the moving-mesh cell center and the closest metric grid point generally do not coincide. One way, which would practically leave the computational effort almost unaffected, is to employ the gradient of each variable (see discussion on $\langle\nabla\phi\rangle$ in Section 3.3).

3.7. Mesh geometry and motion

The moving-mesh approach offers significant flexibility with respect to the mesh geometry. The mesh-generating points can be distributed in an arbitrary way, as long as the mesh-construction algorithm can successfully create the Voronoi tessellation. Hence, the mesh geometry can be chosen based on the physical and geometrical characteristics of the problem, such as the mass distribution and the symmetries of the simulated physical system. For a fixed number of mesh-generating points, focusing the resolution on physically important regions captures the physics more accurately compared to other point distributions not adjusted to the problem. In the various simulations that we perform, we employ different initial point distributions, i.e. we start from different initial mesh geometries.

During the simulation, the mesh evolves based on the motion of the mesh-generating points. The velocities of the points can be chosen nearly arbitrarily. In our moving-mesh simulations each point moves with the local fluid coordinate velocity, while in cases where a cell becomes too irregular a corrective velocity component is added to suppress possible discretization errors and mesh noise [100,273,304]. To compute the distortion of a cell, we define for each cell the parameter

$$\alpha_{\mathrm{max}} = \max_i \left(\frac{1}{h_i} \sqrt{\frac{A_i}{\pi}} \right), \tag{3.21}$$

where the index i runs over all the faces of the cell, h_i is the distance from the mesh-generating point to the face and A_i is the face area. Large values of α_{max} indicate irregular cells. The corrective velocity term for each cell then reads

$$v_{\mathrm{cor}} = \begin{cases} 0 & , \alpha_{\mathrm{max}} \le 0.75\,\beta \\ f_{\mathrm{shaping}}\,\frac{\alpha_{\mathrm{max}}-0.75\beta}{0.25\beta}\,v_{\mathrm{char}} & , 0.75\,\beta < \alpha_{\mathrm{max}} \le \beta \\ f_{\mathrm{shaping}}\,v_{\mathrm{char}} & , \alpha_{\mathrm{max}} > 0.75\,\beta \end{cases} , \tag{3.22}$$

where v_{char} is a local characteristic speed which we take to be the speed of sound in the cell, β a parameter which determines when the corrective velocity term is applied (i.e. which cells are classified as irregular) and f_{shaping} determines the fraction of the characteristic speed applied to the mesh-generating point. Typical values are $\beta \approx 2.25$ and $f_{\mathrm{shaping}} \approx 0.5$. This prescription to ensure mesh regularity was originally introduced in [304] (see also [308]).

Creating a mesh-generating point distribution which is well-adapted to the problem and drifting the mesh-generating points primarily based on the local fluid velocity reduces, up to some extent, the need for adaptive mesh refinement. Nevertheless, Arepo can dynamically increase or decrease the local resolution by refining or derefining cells. The process of cell refinement consists of splitting a cell into two distinct cells by inserting a new mesh-generating point within a distance of $0.025R_i$ from the cell's original point. Here R_i is the cell's effective radius (see discussion of Eq. (3.7)), while the exact position of the new mesh-generating point is randomly generated within the described region. The conserved variables are conservatively distributed to the two new cells, while the mesh regularization algorithm steers the points away from each other over the next few time steps. Notably, refinement does not affect the geometry of any cell outside the one involved in the process. On the other hand, cell derefinement is achieved by removing a cell and distributing the conserved variables to the surrounding cells, based on the fraction of the original cell's volume that each one of the neighbors claims. Nearly arbitrary criteria can be used to trigger the refinement or derefinement of a cell, which makes these two operations particularly useful in many different scenarios, such as maintaining a roughly constant mass resolution during the evolution, increasing the resolution in physically interesting regions or decreasing the resolution to reduce the computational effort. For more details see [273].

In addition to the moving-mesh simulations, we also perform static-mesh simulations, i.e. simulations where the cells do not move, but stay fixed at their initial positions. Static-mesh simulations enable a more direct comparison to existing literature results. Overall, we provide details on the initial mesh geometry, mesh motion and whether we employ the functionality of cell refinement and derefinement when we discuss each simulation.

3.8. Additional details

In Section 2.6 we describe different possible approaches to the EOS. In Arepo we implemented a high-density EOS module, which supports zero-temperature tabulated microphysical EOS complemented with a thermal ideal gas component. We employ this approach in simulations of isolated, static NSs, which also serve as a test of the implementation. Furthermore, we present a BNS merger with this microphysics description. In addition, the code can run simulations based on either a polytropic or an ideal gas EOS. We run test simulations of isolated stars employing the ideal gas EOS.

As it is typical in grid-based treatments of hydrodynamics, we employ an artificial atmosphere for vacuum regions. In particular, we define a floor density $\rho_{\rm atm}$ and cover vacuum regions with cells of this density. Every time that we recover the primitive variables, i.e. in every Heun substep of the time integration, we identify all cells with density below a threshold value $\rho_{\rm thr} > \rho_{\rm atm}$ and reset their density to $\rho_{\rm atm}$. In addition, we reset the velocities in atmosphere cells to zero and compute the pressure and specific internal energy based on a polytropic EOS with $K = 100$ and $\Gamma = 2$. We then recompute the conserved variables in the cell, based on the new values of the primitives. In the simulations which we discuss in this work, the atmosphere density is defined to be in the range $\rho_{\rm atm}/\rho_{\rm max} = 10^{-7} - 10^{-8}$, where $\rho_{\rm max}$ is the maximum density in the whole numerical domain at a given time. We set the threshold density to $\rho_{\rm thr} = 10 \times \rho_{\rm atm}$. The ratios $\rho_{\rm atm}/\rho_{\rm max}$ and $\rho_{\rm thr}/\rho_{\rm atm}$ are code parameters that can be chosen by hand.

In our implementation the GRHD equations are solved on a Voronoi mesh, while the metric equations are solved on an independent uniform Cartesian grid. In Section 2.4 we describe how we obtain boundary conditions for the metric grid. In the case of the hydrodynamic mesh, we adopt periodic boundary conditions, which however do not influence our evolutions because the boundaries of the Voronoi mesh are carefully placed at a large distance from the regions of physical interest. Due to the fact that a small number of large atmosphere cells suffices to cover these distant regions, the computational demand is practically unaffected by the size of the hydrodynamic mesh. We provide more information on the size of both the Voronoi mesh and the metric grid in the discussion of each simulation. In all cases the metric grid covers the regions of interest and the Voronoi mesh extends even further and defines the size of the numerical domain.

4. Static neutron stars on a moving mesh

4.1. Radial pulsation test

A standard test for general relativistic codes consists of extracting the radial pulsation frequencies of isolated NSs. Initially, we compute stellar models of static stars by solving the TOV equations. The equations describe static, spherically symmetric solutions, which makes them 1D. Hence, they can be integrated with a very small spatial step of the order of meters or even less. The high resolution solution is then mapped to the 3D mesh of Arepo.

The stellar configurations are formally static. However, because of the finite resolution of 3D codes, truncation errors at the surface and the center of the star (i.e. at the points where the solution exhibits extrema and the hydrodynamical schemes become lower order) excite small amplitude radial oscillations. These radial pulsations correspond to normal modes of pulsation of the star. The amplitude of the pulsation decreases as the resolution used in the 3D code increases. Hence, the amplitude does not carry any physical information about the system. On the other hand, the frequencies of the radial pulsations do carry information about the system, because they should match the values computed based on perturbative calculations for the radial mode of single NSs (see Section 2.5.1). Hence, extracting the frequencies of the radial oscillation from evolutions of isolated NSs based on a Fourier analysis and comparing to perturbative calculations or results from independent codes, serves as a test for 3D implementations.

In this chapter we perform two distinct tests. In the first test, we evolve an isolated NS described by a polytropic EOS on a fixed spacetime, namely we keep the metric fixed and neglect all spacetime perturbations (Cowling approximation). This evolution employs our hydrodynamics modules alone and aims to evaluate our GRHD implementation. In the second test, we evolve a NS described by a microphysical EOS and dynamically evolve the spacetime as well. This more demanding setup tests all the main components of the code, i.e. the GRHD implementation, the metric solver and their coupling, as well as the microphysics module.

To ensure that we specifically excite the radial eigenmode and enhance the oscillation amplitude, we add a radial 3-velocity perturbation of the form

$$\delta v_r = A \sin\left(\frac{\pi r}{R}\right) \tag{4.1}$$

to the initial data. Here A is the perturbation amplitude, r is the radial distance from the stellar center and R is the radius of the star. We provide more information about the setup that we use in each test in the respective sections.

4.2. Cowling approximation

4.2.1. Initial data

We solve the TOV equations using a polytropic EOS with $K = 100$ and $\Gamma = 2$. Starting from a central density $\rho_c = 1.28 \times 10^{-3} \approx 7.91 \times 10^{14}\ \mathrm{g \cdot cm^{-3}}$, we construct a stellar model with a gravitational mass $1.4\ M_\odot$ and radius $R \approx 12$ km (in isotropic coordinates). This particular configuration is a common choice in radial pulsation tests, which allows us to compare to independent literature results (e.g. [116]).

We map the 1D TOV solution to the 3D Voronoi mesh, such that the center of the star is located at the center of the simulation domain in Arepo. We set the numerical domain to be a cube with side $58\ M_\odot \approx 85.6$ km and place mesh-generating points to construct a mesh. Around the center of the domain, where the star lies, we distribute mesh-generating points to obtain a high-resolution uniform Cartesian grid with a side of $24\ M_\odot \approx 35.4$ km, where each cell has a side $h = 0.1\ M_\odot \approx 147.6$m. Throughout the whole evolution, this Cartesian grid covers the star. We cover the rest of the domain with points which result in a lower resolution. These outer cells do not affect the evolution and are only required to guarantee a successful mesh construction. Employing a Cartesian mesh around the star enables a direct comparison with [116], which presents results from a Cartesian grid code.

We evolve the initial data based on an ideal gas EOS, i.e. we evolve the energy equation in the system (2.6) as well. Any cell with density $\rho < 10 \times \rho_{\mathrm{atm}}$ is reset to be part of the atmosphere, where we pick $\rho_{\mathrm{atm}} = 10^{-8} \times \rho_{\mathrm{max}}$. During the simulation this criterion captures many cells of the central Cartesian grid (see Fig. 4.3), as well as all the cells which lie further away. In the simulations discussed in this section we explicitly disable refinement and derefinement. In addition, the spacetime is static. We interpolate the high resolution metric profile, which we obtain from the TOV solution, to any position in the domain where knowledge of the metric fields is required. Finally, we induce by hand a radial excitation with an amplitude $A = -0.005$ to the initial data based on Eq. (4.1).

4.2.2. Simulations

We perform both a moving-mesh and a static-mesh simulation with the same setup. In particular, we evolve the initial data for roughly 10 ms. Figure 4.1 presents the evolution of the maximum rest-mass density ρ_{max}, throughout the whole simulation domain, normalized to its initial value. Due to the radial pulsation, i.e. the contraction and expansion of the stellar model, the maximum density oscillates. The blue line refers to the moving-mesh simulation, while the orange line shows the static-mesh simulation, i.e. a simulation where the cells are kept fixed.

In Fig. 4.2 we present the spectrum of the oscillation, which we extract based on a Fourier transform of the density evolution. Colors are kept the same as in Fig. 4.1. The vertical dashed lines correspond to the frequencies presented in [116], namely they refer to frequencies computed with an independent 3D code. Focusing on the fundamental frequency, we obtain 2.672 kHz for the moving-mesh and 2.682 kHz for the static-mesh simulation, respectively. Both frequencies are in excellent agreement with the value reported in [116], which is 2.696 kHz. In addition, higher frequency modes are excited in the two simulations that we perform and are visible in the spectrum. In

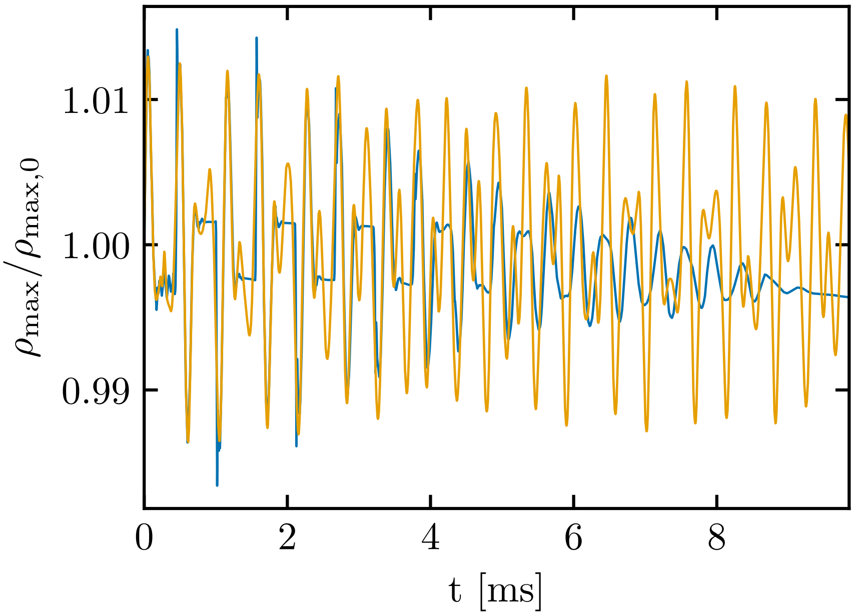

Figure 4.1: Evolution of the normalized maximum rest-mass density for a 1.4 $M_{\odot}$ TOV NS modelled as a polytrope with $K = 100$ and $\Gamma = 2$. The blue and orange lines refer to a moving- and static-mesh simulation, respectively. In both simulations the spacetime is kept fixed. For details regarding the simulation setup see the main text. Figure adapted from [196].

the moving-mesh evolution, we can identify a total of six overtones. The first two overtones are quite pronounced. All the higher mode frequencies match excellently those discussed in [116]. Similarly, in the static-mesh simulation, we clearly identify two overtones, which also align well with the benchmark frequencies. The overall agreement in the frequencies of the fundamental mode, as well as higher frequency modes, validates our GRHD implementation.

Based on Fig. 4.1, both the moving- and static-mesh evolutions preserve the value of the maximum density quite well over the course of the roughly 10 ms for which we simulate the system. Namely, the secular evolution of the maximum rest-mass density is small and, at the end of the simulation time, the stellar configurations are still very close to the initial static equilibrium. The two evolutions are quite similar during the first few milliseconds. However, the moving-mesh simulation exhibits some damping at later times, which probably originates from the surface. Based on the excitation that we add, the star initially contracts. Stellar cells, namely cells with $\rho > \rho_{\rm thr}$, move away from atmosphere cells (i.e. cells where $\rho < \rho_{\rm thr}$). This creates a gap between them, effectively lowering the resolution locally. During the expansion of the star, stellar cells move beyond the equilibrium radius of the model and into what originally was atmosphere. Throughout this oscillation, cells close to the surface which initially belonged to the star can cross below $\rho_{\rm thr}$ and become atmosphere and, vice versa, atmosphere cells can become stellar and start moving. Overall, this process lowers the resolution close to the surface. This can be seen in Fig. 4.3, which shows snapshots of the rest-mass density along the equator for both the moving-mesh (left panel) and static-mesh (right panel) run. We only present the region [0, 14] km in both the x- and y-axis, while we overplot the grid with white lines. Already after

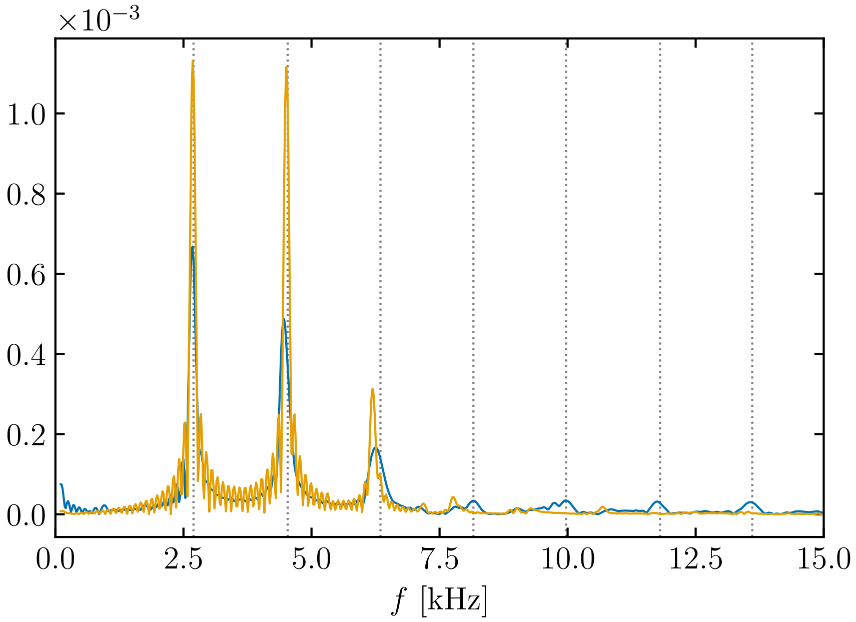

Figure 4.2: Fourier spectrum of the normalized density evolution in a moving-mesh (blue) and a static-mesh (orange) Cowling evolution of a static 1.4 $M_\odot$ stellar model. The NS is described by a polytropic EOS with $K = 100$ and $\Gamma = 2$. Vertical dashed lines correspond to frequencies computed with an independent 3D code [116]. The fundamental frequency and higher overtones in our results are in excellent agreement with the literature results. The units of the vertical axis are arbitrary.

≈ 2 ms of evolution, larger cells (i.e. lower resolution) form due to mesh motion close to the surface in the moving-mesh simulation, compared to the static-mesh run. This decrease of the resolution close to the surface is quite possibly the main reason for the oscillation damping, considering that the radial pulsation is quite sensitive to the surface.

Figure 4.3 also shows that the mesh in the moving-mesh run changes due to cell motion. Already, within roughly 2 ms from the simulation start, the mesh differs from how it was in the beginning of the simulation. In particular, close to the surface the resolution is lower, while many cells accumulate right outside the surface and a thin high resolution layer forms. This highlights that, in moving-mesh simulations, even defining a single resolution in terms of a characteristic length is practically impossible. Hence, a direct comparison between moving-mesh simulations and fixed grids is not necessarily straightforward. Even if the initial mesh in a moving-mesh setup is identical to a static mesh, the motion of mesh-generating points quickly changes the positions, shapes and sizes of the cells.

In addition, we comment on the choice of a Cartesian mesh as a starting point for moving-mesh simulations of isolated NSs. Cartesian grids do not take the spherical symmetry of the system into account. Moreover, they have (initially) the same resolution in all regions, regardless of the mass distribution of the system. As it is shown in Fig. 4.3, this can lead to issues, especially close to the surface, where NSs exhibit a very steep density gradient. In particular, the small cells which form right outside the surface can, in principle, lower the (global) time step and increase the computational effort. This issue can be alleviated by derefining small cells, which however we do not

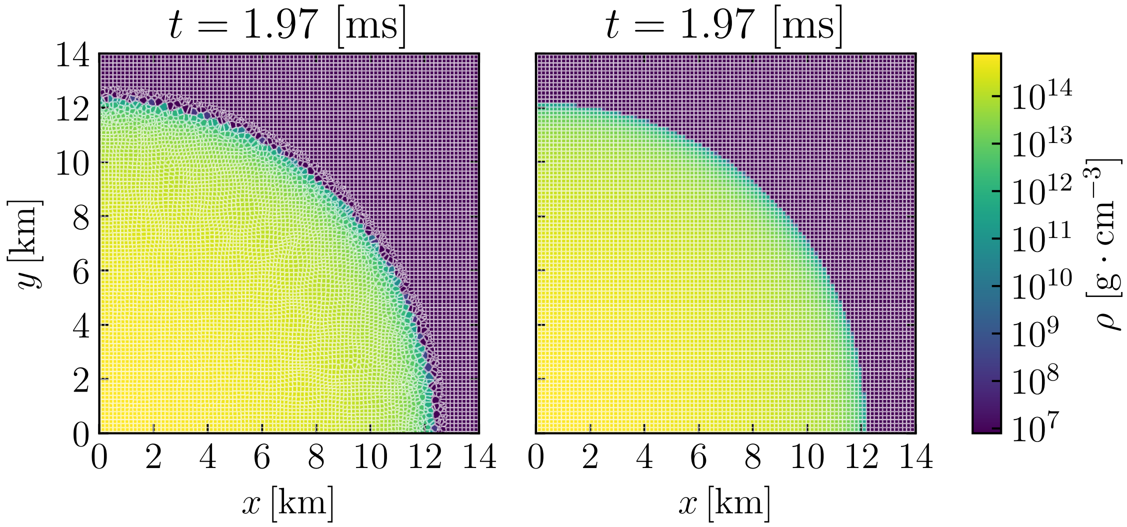

Figure 4.3: Rest-mass density along the equator ($z = 0$ plane). We focus in the range $[0, 14]$ km in both the x- and y-axis. This region is covered by a high resolution Cartesian grid, which is overlaid in white lines. The left and right panels correspond to the moving- and static-mesh Cowling simulations (discussed in Section 4.2.2), respectively. Both snapshots show the state of the system after evolving the initial data for almost 2 ms. Mesh rearrangement in the moving-mesh simulation is evident in the left panel, in particular close to the surface.

do in the simulations discussed in this section. Finally, independently of the simulated system, the mesh construction algorithm typically takes more time to generate a Cartesian grid, compared to other distributions with the same number of mesh-generating points, due to the extra effort required to resolve geometric degeneracies during the mesh construction.

It is important to remark that an essential part of moving-mesh simulations is to identify the setup which better captures the simulated systems dynamics. In the case of isolated stars, it is evident that a Cartesian grid is not the most appropriate choice. Since our main focus is BNS mergers, we do not examine this point in detail in the current context. However, we highlight that different initial mesh geometries, mesh motion parameters or the use of refinement/derefinement can, in principle, lead to better results.

In addition, the overall evolution of the system is sensitive to the exact choice of hydrodynamics schemes, regardless of whether the simulation employs a moving or static mesh (see e.g. [116] for the dependence of static-mesh simulations on different slope limiters and Riemann solvers). Due to cell rearrangement in a moving-mesh run, the exact effect of the chosen hydrodynamics schemes on the evolution might differ, up to some extent, between moving- and static-mesh simulations. We briefly examine how a different slope limiter affects our moving-mesh evolution in Fig. 4.4, where we present two moving-mesh simulations. The blue line refers to the moving-mesh simulation that we have already discussed, i.e. matches the blue line in Fig. 4.1. The orange line is another moving-mesh simulation, which differs only in the way that the primitive variables are reconstructed to the cell faces. In particular, instead of our standard recipe, which involves Eq. (3.13) and the MC slope limiter, we employ Eq. (3.9) directly. Clearly, the two evolutions are rather similar in the first few milliseconds.

At later times, employing Eq. (3.9) for the reconstruction leads to less damping. Focusing on the new simulation (orange line), the oscillation is still sizeable at the end of the simulation time, while overtones can be identified in the rest-mass density evolution even at late stages. We obtain 2.677 kHz for the main frequency of the radial mode, namely slightly higher compared to the original run with the MC slope limiter. The differences between the two simulations most probably originate from the fact that slope-limited reconstruction becomes first-order accurate at local extrema by construction, while Eq. (3.9) has no such property. Hence, the simulation with the MC slope limiter should, in principle, be more dissipative. At the same time, slope limiters resolve sharp discontinuities without introducing spurious oscillations, which is why they are our standard choice in this work.

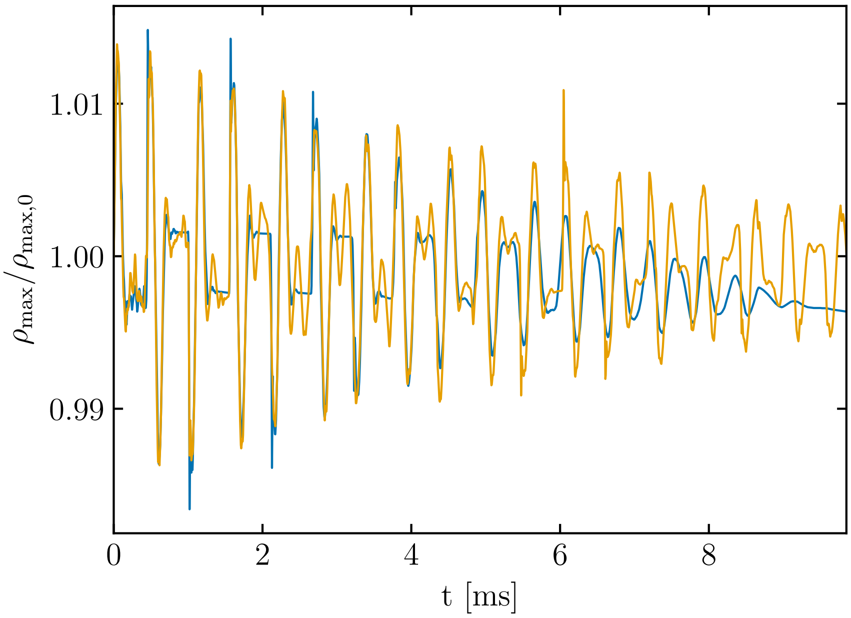

Figure 4.4: Maximum rest-mass density evolution in two moving-mesh simulations, which differ only in the employed reconstruction scheme. The blue line refers to a run with MC slope-limited reconstruction, while the orange line corresponds to an evolution where the primitive variables are reconstructed to the cell faces based on Eq. (3.9).

Figure 4.4 shows that a more detailed analysis of the effect of the employed hydrodynamics schemes to moving-mesh simulations can in principle lead to better results. A similar argument can be made for the details of the mesh setup (e.g. initial mesh geometry and cell motion). We briefly examine the impact of grid orientation effects, originating from the initial mesh geometry, in the next section.

4.3. Dynamical spacetime

4.3.1. Initial data

We solve the TOV system with the H4 EOS [176] modelled as a piecewise polytrope [246] and construct a 1.41 $M_\odot$ stellar model. The configuration has a radius $R \approx$

11.69 km in isotropic coordinates and central density $\rho_c = 9.545 \times 10^{-4} \approx 5.9 \times 10^{14}\ \mathrm{g} \cdot \mathrm{cm}^{-3}$.

In Arepo we employ a spherical distribution for the mesh-generating points. Based on this setup, we construct a spherical grid around the center of the simulation domain. The grid consists of 85 shells which extend to a distance of 11 $M_\odot \approx 16.2$ km. The distance between consecutive shells is fixed and equal to ≈ 191 m. In addition, to make sure that the mesh-construction algorithm can generate the Voronoi tesselation, we cover the numerical domain with a coarse Cartesian grid. The numerical domain's size is the same as in our Cowling tests (i.e. a cube with side 58 $M_\odot \approx 85.6$ km), while our mesh is clearly different. This setup corresponds to our standard resolution. In addition, we perform higher and lower resolution simulations to examine the dependence of our results over a (limited) range of resolutions. The mesh setup for these additional resolutions is similar to our standard resolution. In the high resolution setup, we employ 100 shells, which correspond to a radial separation between cells of ≈ 162.4 m. At the same time, the low resolution setup features 64 shells, i.e. a resolution of ≈ 253.7 m. Finally, we also explore the influence of grid effects on the results by considering a fourth mesh, which closely follows the standard resolution grid, but we randomly distribute the mesh-generating points on each shell.

In this section we do not compare our radial frequency results to a Cartesian grid, as we do in Section 4.2. We instead compute the radial frequencies employing perturbation theory based on an independent code which we developed (see Section 2.5.1). We explore this additional flexibility and simulate the system with the mesh setups that we describe, which in principle capture the geometrical characteristics of a single star better than a Cartesian grid.

We evolve the initial data with the H4 EOS, which we complement with a $\Gamma_{\mathrm{th}} = 1.75$ thermal ideal-gas component. In the simulations which we present in this section, we consider a dynamical spacetime by solving the metric field equations on an independent, uniform Cartesian grid with a resolution $h_{\mathrm{M}} = 0.3\ M_\odot$ and a total of 129^3 grid points. Similarly to our Cowling simulations, we set the atmosphere density to $\rho_{\mathrm{atm}} = 10^{-8} \times \rho_{\mathrm{max}}$ and the atmosphere threshold value to $\rho_{\mathrm{thr}} = 10 \times \rho_{\mathrm{atm}}$. Furthermore, we do not refine or derefine cells. A radial perturbation with an amplitude $A = -0.001$ is added to the initial data based on Eq. (4.1).

4.3.2. Simulations

Similarly to our Cowling tests, we perform moving- and static-mesh simulations. In Fig. 4.5 we present the evolution of the normalized maximum rest-mass density for the moving-mesh (blue) and static-mesh (orange) evolutions with the standard resolution setup. In both runs we evolve the system for roughly 10 ms. We extract the main radial pulsation frequency from the density oscillation. We obtain 2.343 kHz for the moving-mesh and 2.358 kHz for the static-mesh runs. To compare, we compute the radial mode frequency based on the perturbative code and find 2.385 kHz. The small deviations we find are comparable to what is found by other codes, e.g. [116].

In both simulations, there is no significant drift in the density, which highlights that the code preserves the initial TOV equilibrium rather well. The rest-mass density oscillation features some damping in the moving-mesh simulation. Still, it can be clearly identified for as long as we evolve the system. Similarly to our Cowling tests, this behavior quite possibly originates from the surface. Spherical grids are well-

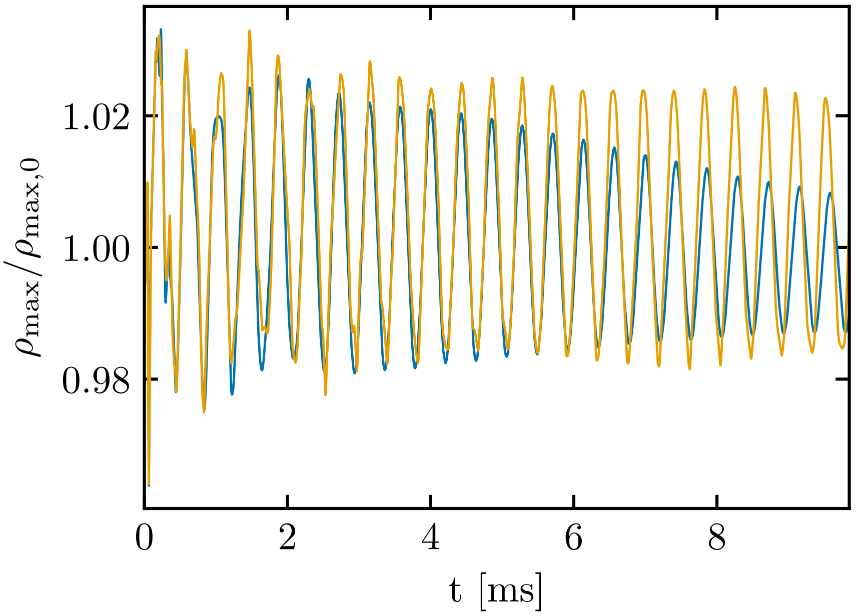

Figure 4.5: Normalized maximum rest-mass density from a moving-mesh (blue line) and a static-mesh (orange line) evolution of a 1.41 $M_{\odot}$ star described by the H4 EOS. The spacetime is evolved dynamically and the metric field equations are solved on a grid with 129^3 points and resolution 0.3 $M_{\odot}$. The pulsation is excited with a radial velocity perturbation with amplitude -0.001. See the main text for a description of the initial mesh-generating point distribution. Adapted from [196].

adapted to the spherical symmetry of the TOV solution. However, they do not take into account the mass distribution in the system and are prone to the same issues that we faced with a Cartesian grid in the region close to the surface (see Fig. 4.3 for Cartesian grid). In principle, modifications in the moving-mesh simulation setup, which target the mesh motion and resolution close to the surface, can improve the behavior. However, we do not investigate this point further.

To evaluate the effect of resolution to the radial mode frequency and density evolution, we also perform moving-mesh simulations with the lower and higher resolution mesh setups. We show the normalized maximum density for these runs in Fig. 4.6. The blue line corresponds to the standard resolution moving-mesh run, while the green and orange curves correspond to the lower and higher resolution runs, respectively. We extract the main oscillation frequency, based on a Fourier tranform, for the lower and higher resolution simulations. We obtain frequencies of 2.318 kHz and 2.352 kHz respectively, i.e. the frequency approaches the perturbative value with increasing resolution. We present the frequencies alongside the perturbative result in Fig. 4.7. Evidently, increasing the resolution positively affects the results. We remark that a proper convergence analysis is not possible, because the simulations do not span a broad range of resolutions.

In Fig. 4.5 it is evident that the resolution affects the evolution of the maximum density. The lower resolution run exhibits more damping, while the density drift towards smaller values is more pronounced. On the contrary, increasing the resolution reduces the secular drift of the maximum rest-mass density, i.e. preserves the TOV equilibrium more accurately. Similarly, the oscillation is damped less in the high

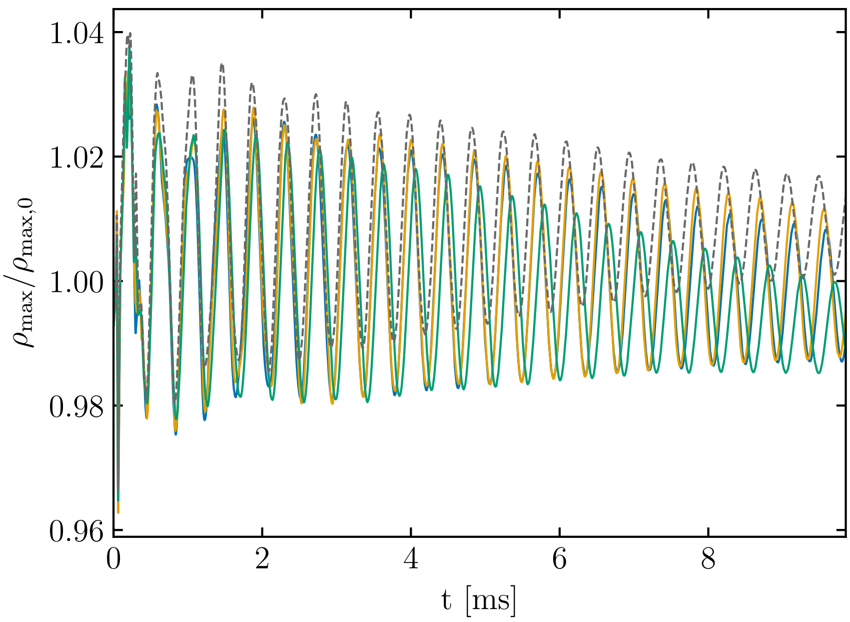

Figure 4.6: The green, blue and orange lines correspond to simulations with resolutions ≈ 253.7 m, ≈ 191 m and ≈ 162.4 m respectively, in which we complement the H4 EOS with a $\Gamma_{\text{th}} = 1.75$ thermal ideal-gas. Increasing the resolution leads to smaller oscillation damping and less density drift. The gray dashed line shows an adiabatic evolution (see text) with a resolution ≈ 191 m. Contrary to the other simulations, the (minor) secular evolution of the rest-mass density in the adiabatic run is towards higher densities. Note that the blue line is the same as in Fig. 4.5.

resolution simulation compared to both the lower and standard resolution cases. For all the resolutions that we examine, the oscillation survives for the ≈ 10 ms of evolution that we present, while the drift of the maximum density is minimal. Namely, all three moving-mesh evolutions remain very close to the initial TOV stellar model.

In addition to the different resolution runs, we perform a moving-mesh simulation on a grid similar to our standard resolution of ≈ 191, which, however, also includes an additional random component in the positions of the mesh-generating points. We obtain a frequency of 2.349 kHz, which is slightly higher compared to the run with standard resolution, but without the random offset. The rest-mass density evolution is rather similar between the two standard resolution moving-mesh runs (with and without random component). The oscillation damping is only slightly more pronounced when randomly placing the points on the shells. Moreover, by inspecting the positions and velocities of the mesh-generating points throughout both evolutions, we note that adding the random component reduces grid orientation effects.

In all the runs which we discussed in this section, we complement the H4 EOS with a $\Gamma_{\text{th}} = 1.75$ thermal ideal-gas. In principle, the inclusion of a thermal component should not affect the evolution significantly, which is what we see in all the simulations with a dynamical spacetime that we discussed up to now. For the description of stable stellar models which remain close to the initial TOV equilibrium, we can also perform adiabatic evolutions, i.e. do not evolve the specific energy, but instead compute it alongside the pressure based on the tabulated H4 EOS in each time step. Such an evolution is not appropriate for systems in which thermal effects are

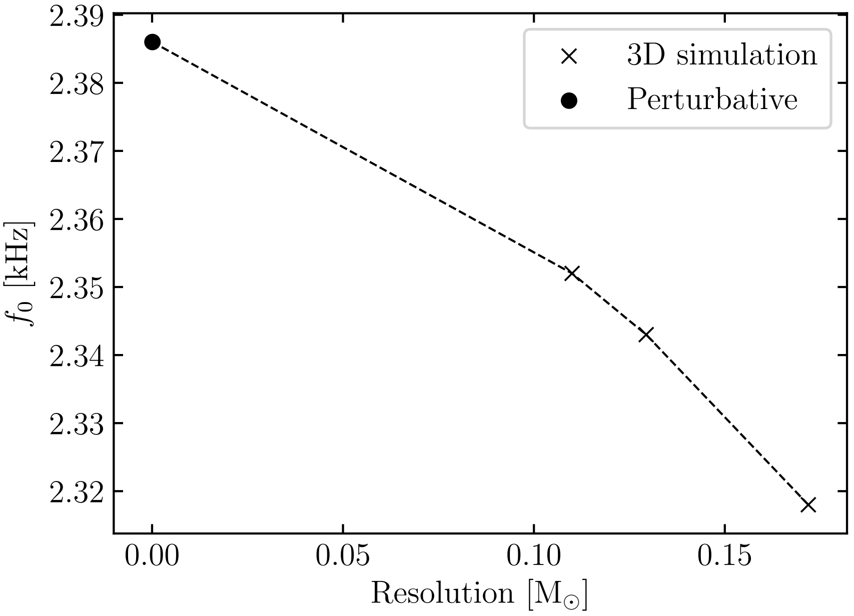

Figure 4.7: Main radial mode frequency of a 1.41 $M_\odot$ TOV star described by H4. The crosses correspond to 3D simulations with different resolutions. The filled circle refers to the perturbative calculation. The dashed lines connect consecutive points and carry no extra information.

significant. However, it should be rather accurate in evolutions of stable TOV configurations close to equilibrium. We perform an adiabatic simulation with the standard resolution ≈ 191 m. We find that such evolutions are more prone to grid orientation effects. Hence, we add an additional random component to the initial positions of the mesh-generating points, which eliminates axis effects.

The evolution of the normalized rest-mass density is shown in Fig. 4.6 with a gray dashed line. For this particular simulation we obtain a frequency of 2.37 kHz, which is even closer to the perturbative value. This further supports the validity of our implementation. In addition, we note that the secular evolution of the maximum density is slightly different than what we observe in our evolutions with a thermal ideal-gas component. Specifically, the density exhibits a very minor increase over the simulation time. This difference in the behavior of the maximum density drift between adiabatic runs and simulations where we also evolve the energy equation aligns with what is reported in [116].

The overall agreement between the frequencies extracted from the 3D evolutions discussed in this section and the perturbative frequency validates the GRHD and metric solver implementation, their coupling, as well as the EOS module.

5. Binary neutron star mergers on a moving mesh

5.1. Preface

In this chapter we apply our moving-mesh approach to a BNS system. This is the first BNS merger simulation on a moving mesh. In the following sections, we describe our setup, present our results in detail and compare to simulations performed with independent SPH and Eulerian grid-based codes.

5.2. Initial data

In our simulation we model the NSs with the DD2 EOS [150, 297]. Formally, the DD2 model computes the full temperature and composition dependence of the EOS. In this simulation, for convenience, we adopt the "hybrid" approach discussed in Section 2.6. In particular, we employ a slice of the DD2 EOS at $T = 0.1$ MeV as our zero-temperature model and supplement it with an ideal-gas component with $\Gamma_{\rm th} = 1.75$ to describe thermal effects. The DD2 EOS is in full agreement with current observational constraints on the maximum NS mass that an EOS should support [24, 28, 85, 90, 190], while also marginally compatible with constraints on the tidal deformability from the analysis of the inspiral of GW170817 [6, 10].

We generate initial data with the open-source library LORENE[1] [135]. LORENE constructs quasiequilibrium configurations of either corotating or irrotational BNS systems in the inspiral phase. The code employs multi-domain spectral-methods, which allow to directly map the initial data to arbitraty positions. We consider a BNS system with two equal-mass companions with a gravitational mass of $M = 1.35\ M_\odot$ (as measured at infinite binary separation). We place the two stars at an initial separation of $26\ M_\odot \approx 38.4$ km. LORENE adopts the CFC approximation, just like our code, which allows to start our evolutions from such close orbits without unphysical transients. In contrast, fully relativistic simulations would detect and react to the fact that the initial data do not contain GWs. The stars are chosen to be irrotational, because it is considered to be a more realistic scenario [58, 170].

In Arepo we construct an initial mesh, which follows approximately the mass distribution in the binary system, and map the LORENE data to this cell arrangement. In particular, around each one of the two companion stars, we create spherical shells. On each shell we distribute cells based on the HEALPix algorithm presented in [133]. The main purpose is to construct cells which have roughly a mass of $m_{\rm cell,0}$, where $m_{\rm cell,0}$ can be chosen freely. For this particular simulation we set $m_{\rm cell,0} = 1.68 \times$

---

[1] http://www.lorene.obspm.fr/

$10^{-6}\ M_\odot$. In [223] it is discussed in detail how to obtain this grid setup. In order to estimate the size of the shells and guarantee that we obtain cells with approximately the same mass content $m_{\text{cell},0}$, we need to provide an estimate for the mass profile of each one of the stars. For this purpose, we employ the mass profile $m(r)$ of a $1.35\ M_\odot$ TOV star described by the DD2 EOS, which however we modify in the outer parts of the star. In particular, we consider the radial distances $r_{\text{in}} = r(\rho_c/2)$ and $r_{\text{out}} = 1.1 \times R$, where ρ_c is the central density and R the radius of the TOV star. When computing $m(r)$, we keep $\rho\sqrt{\gamma} = \rho\psi^6$ fixed and equal to its value at r_{in} between the distances r_{in} and r_{out} . This modification serves two purposes. By modifying the mass profile we guarantee that the resolution does not drop significantly close to the surface because of the steep density gradient of the actual TOV solution. Instead, these outer stellar regions are also resolved. Moreover, the grid covering each star extends up to a distance r_{out}, i.e. it extends beyond the stellar surface. This is important because the stars in a binary are not perfect spheres, but are (tidally) deformed. As described in [223], applying the HEALPix algorithm requires a coordinate system. In each shell we randomly rotate this coordinate system in space, which results in a mesh with no grid orientation effects.

We cover the rest of the simulation domain, i.e. the (vacuum) regions outside the two spheres with radius r_{out} centered at each star, with a coarse Cartesian grid with resolution $10.1\ M_\odot \approx 14.91$ km. We employ an artificial atmosphere approach for the vacuum, where we adopt the parameters $\rho_{\text{atm}} = 10^{-7} \times \rho_{\text{max}}$ and $\rho_{\text{thr}} = 10 \times \rho_{\text{atm}}$ (see Section 3.8). The metric fields equations are solved on an independent, uniform Cartesian grid with a resolution of $0.8\ M_\odot$ and a total of 129^3 grid points.

Contrary to the TOV simulations which we discuss in Chapter 4, in our binary simulation we employ the cell refinement and derefinement capabilities offered by AREPO. We adopt a number of refinement and derefinement criteria. To ensure that most cells have a similar mass content m_{cell} during the simulation, we refine cells with mass $m_{\text{cell}} > 2 \times m_{\text{cell},0}$ and derefine cells with mass $m_{\text{cell}} < m_{\text{cell},0}/2$. In addition, for each cell we identify the smallest neighbouring cell. We denote the volume of the cell as V and the volume of the smallest neighbouring cell as $V_{\text{ngb}}^{\text{min}}$. To avoid abrupt changes in the resolution, we do not derefine cells for which $V > 1.5 \times V_{\text{ngb}}^{\text{min}}$ holds. Furthermore, we refine cells which are significantly larger than their neighbouring cells, particularly any cell that satisfies $V > 5 \times V_{\text{ngb}}^{\text{min}}$. Cell refinement can in principle create an irregular mesh. To avoid this possibility, we do not refine any highly distorted cell. We define cell distortion based on the parameter α_{max} (see Section 3.7 for the definition) and specifically identify any cell with $\alpha_{\text{max}} \geq 3.375$ as highly distorted [304]. This combination of refinement and derefinement criteria guarantees that, during the simulation, the mesh consists of cells with comparable mass content, while also the regions close to the surface are resolved with decent resolution. Based on the chosen value for $m_{\text{cell},0}$ and the set of refinement and derefinement criteria, we end up with roughly 1.7×10^6 cells with $\rho > \rho_{\text{thr}}$, which resolve physically interesting regions. Most cells outside the stars are quickly derefined in the very early stages of the simulation. Since only a small number of atmosphere cells are required, the size of the numerical domain does not significantly affect the required computational effort in our approach.

Finally, we investigate if our method for producing initial data is robust. We examine this by performing an independent simulation of an isolated $1.35\ M_\odot$ TOV star described by DD2. The mesh setup, metric resolution, atmosphere parameters and refinement/derefinement criteria are the same as in our binary system simulation.

In both the binary, as well as the single star simulation, truncation errors due to the finite resolution excite oscillations in the maximum density and the minimum lapse function. We compare the oscillations in maximum density (see Fig. 5.1) and lapse function evolution from the first few milliseconds of our BNS simulation to those from the single star simulation. We find similar oscillation frequencies, while the amplitudes are slightly higher in the isolated NS simulation. Thus we conclude that the process we follow to construct initial data performs well and no additional errors are introduced except for those which are expected, i.e. discretization errors.

5.3. Simulations

5.3.1. General dynamics

In Fig. 5.1 we present the maximum rest-mass density evolution throughout the whole simulation. We express time w.r.t. the moment of merging of the two NSs. We define the merging time t_{merg} as the time when $|h(t)| = \sqrt{h_+^2(t) + h_\times^2(t)}$ reaches its maximum value. Here h is the GW signal, while h_+ and $h_\times$ denote the plus and cross GW polarizations, respectively. By definition, t_{merg} separates the evolution into two phase, the inspiral ($t < t_{\mathrm{merg}}$) and the post-merger phase ($t > t_{\mathrm{merg}}$). Figure 5.2 shows snapshots of the rest-mass density in the orbital plane at different stages of the binary evolution. The top and middle row panels are on a logarithmic scale, while the bottom row panels are on a linear scale. Regarding the evolution stage, the top left and top right panels present snapshots from the inspiral and shortly after t_{merg}, respectively. The middle and bottom row panels correspond to 20 ms and 39.5 ms after merging. We evolve the binary for a total of roughly 39.5 ms in the post-merger phase.

During the inspiral the two companions revolve around each other. The emitted GWs carry away energy and angular momentum from the system, which leads to a decrease in the orbital separation. Small oscillations can be identified in the evolution of the maximum rest-mass density during the inspiral, especially in the early times (see Fig. 5.1). As discussed, these oscillations originate from discretization errors, which excite dominantly the radial mode. As the orbital separation decreases, the stars become deformed due to tidal effects. These deformations can be identified in the top left panel of Fig. 5.2, which presents a snapshot of the system a few milliseconds before the merger.

After a few revolutions, the stars collide. As soon as the stars merge, the maximum density suddenly increases (Fig. 5.1), while the temperature[2] T of material at the collision interface rises due to shock-heating. In Fig. 5.3 we present the temperature in the orbital plane of the binary. The top row shows snapshots right after the two stars merge, when the highest temperatures are reached in the system. The bottom row presents two later times in the post-merger phase, which match the times shown in the middle and bottom row of Fig. 5.2. In all the panels of Fig. 5.3, we include contour lines corresponding to two different densities. The dashed white line marks where the density is 10^{13} g $\cdot$ cm^{-3}. Hence, it is indicative of the regions where most of matter is

---

[2] In our "hybrid" EOS approach, we estimate the temperature from the thermal energy (see Eq. (2.46)) via the relation $\epsilon_{\mathrm{th}} = \frac{kT}{m_{\mathrm{B}}(\Gamma_{\mathrm{th}}-1)}$, where k denotes the Boltzmann constant and m_B is the baryon mass.

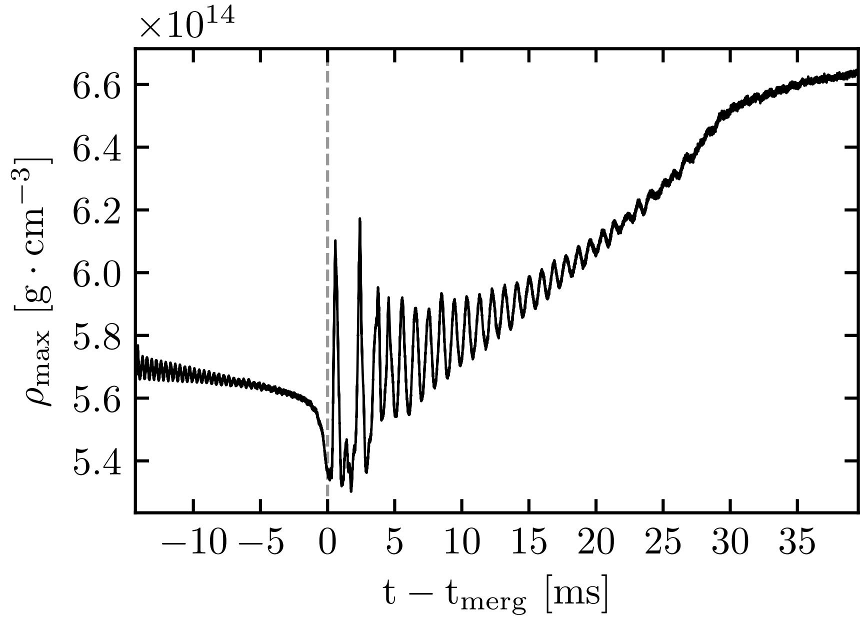

Figure 5.1: Evolution of the maximum rest-mass density for a BNS merger of two 1.35 $M_\odot$ NSs described by the DD2 EOS. The vertical dashed line denotes the merging time. Adapted from [196].

found. The solid white line indicates where the density equals 2.7×10^{14} $\mathrm{g \cdot cm^{-3}}$, i.e. the nuclear saturation density.

High-density matter, with the exception of material at the collision interface, remains cold during the merger phase. Matter at the collision interface heats up, reaching temperature of $\approx$ 90 MeV. The high thermal pressure, occurring as a result of the high temperature, lowers the density in these regions to slightly below 2.7×10^{14} $\mathrm{g \cdot cm^{-3}}$, as seen in the top row of Fig. 5.3. These lower density regions can also be identified in the top right panel of Fig. 5.2 and form as material from the two stars mixes right after merging (see e.g. [165]). When the outer layers of the two stars come into contact, the velocity parallel to the orbital plane exhibits a discontinuity. Hence, these regions are subject to the Kelvin-Helmholtz instability and the creation of local vortices. The distribution of thermal energy, and in turn temperature, is indicative of the local vorticity (see e.g. [166]). As a result, the upper row snapshots in Fig. 5.3 follow, up to some extent, the formation and evolution of vortices.

The two stellar cores do not directly merge in the post-merger phase. Instead, a double-core structure forms, which, in our simulation, survives for more than 20 ms after merging. The two distinct cores can be identified at $t - t_{\mathrm{merg}} = 20$ ms in the middle left and bottom left panels of Fig. 5.2, as well as in the bottom left panel of Fig. 5.3 in the region enclosed by the solid white line. The highest density parts of the two cores merge roughly 28 ms after t_{merg}, which is significantly longer compared to Eulerian grid-based simulations (see e.g. [141,165]). Notably, the high-density material does not settle to a single, spherically-shaped core throughout the almost 40 ms in the post-merger phase for which we simulate the system. Even at the latest times in the post-merger phase that we simulate (i.e. $\approx$ 39.5 ms), the high-density material has a bar-shaped structure. We note that, as shown in Fig. 5.1, the quasi-radial oscillation also lasts for similar timescales as the double-core phase.

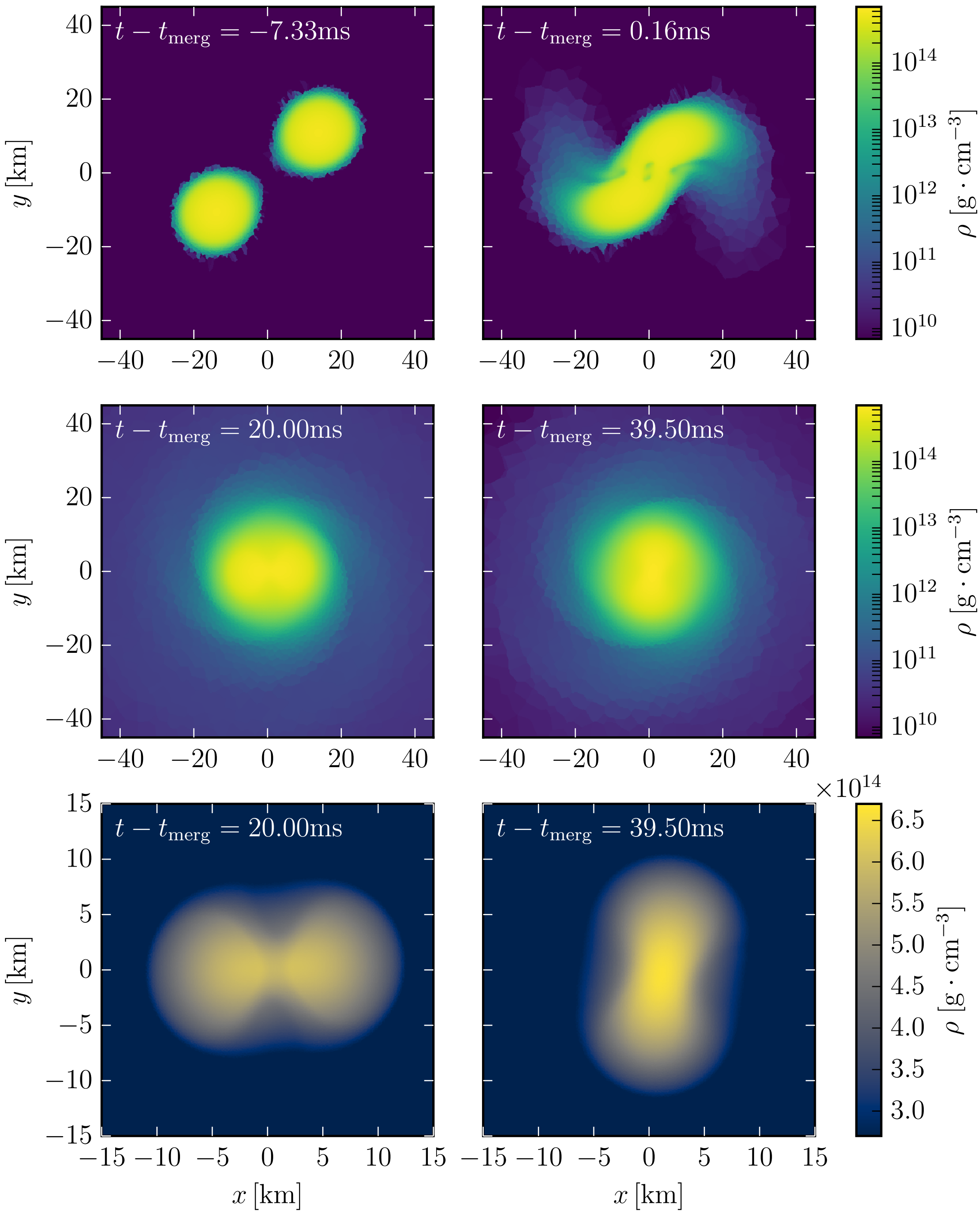

Figure 5.2: Rest-mass density in the orbital plane for the BNS merger simulation. The upper and middle row panels are shown on a logarithmic scale, while the bottom row panels are on a linear density scale and present only the high-density material in the merger remnant. Snapshots from the inspiral and right after merging are displayed in the top row panels. The middle row panels show two times in the late stages of the post-merger evolution. The times in the bottom row panels are identical to those in the middle row. Adapted from [196].

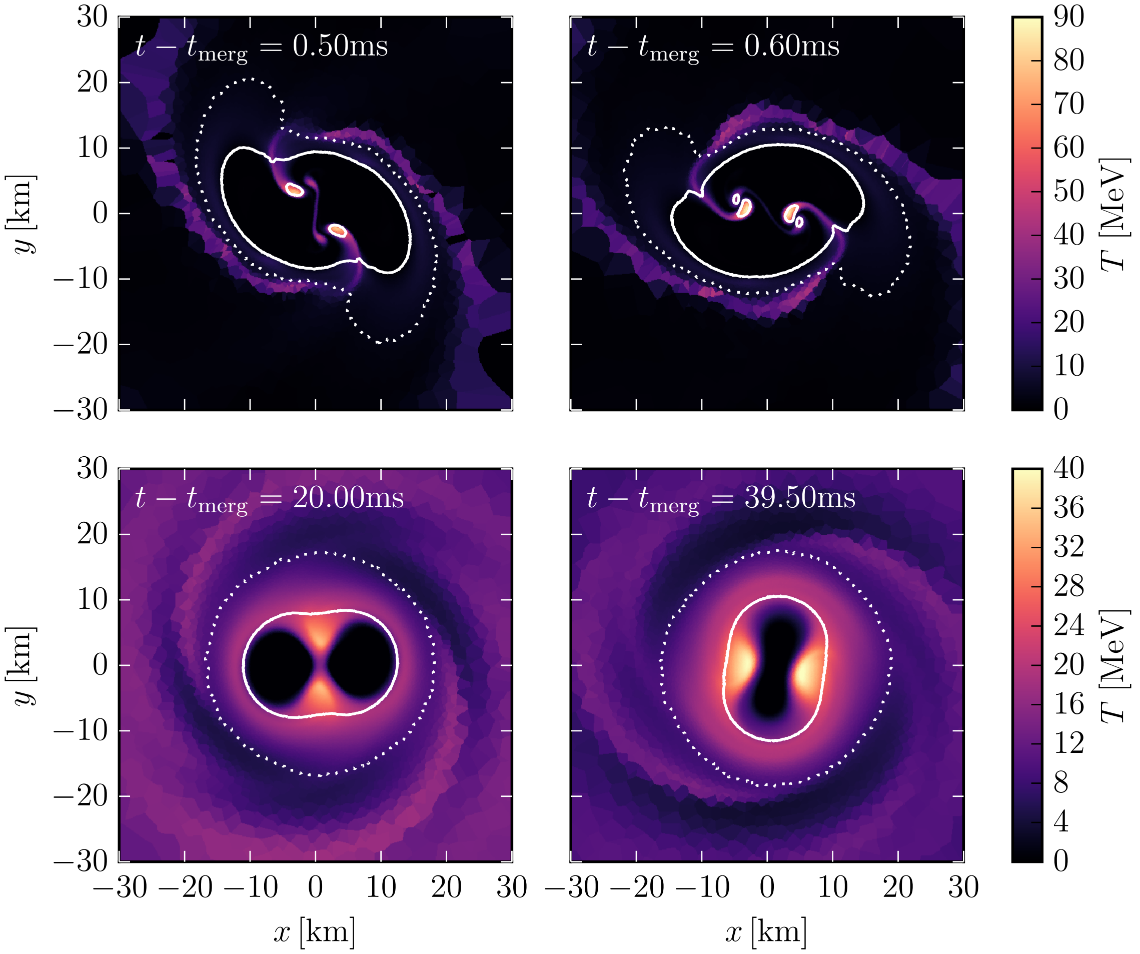

Figure 5.3: Temperature snapshots for the BNS merger simulation. Each panel shows a slice through the orbital plane of the binary. The bottom row focuses at times right after merging, when the temperature increases and reaches $T \approx 90$ MeV, which is the highest during the whole evolution. The bottom row presents late times in the post-merger phase. Densities corresponding to $10^{13}\ \mathrm{g \cdot cm^{-3}}$ and $2.7 \times 10^{14}\ \mathrm{g \cdot cm^{-3}}$ are shown as white dotted and solid contour lines, respectively. High-density material remains cold even at late stages of the evolution. Figure adapted from [196].

High-density matter remains cold throughout the whole post-merger phase, as shown in the bottom row panels in Fig. 5.3. High temperatures up to ≈ 40 MeV occur at the outer edges of the contact interface between the two cores at later times in the post-merger phase. Notably, even at the end of our simulation, i.e. $t - t_{\mathrm{merg}} = 39.5$ ms, spiral density arms starting from the central remnant can be identified both in the middle right panel in Fig. 5.2, as well as in the bottom right panel in Fig. 5.3.

It has been proposed that in remnants of equal-mass binary systems an $m = 1$ instability might occur, which would also contribute to the GW signal [103,187,233,240]. The occurrence of odd modes requires a breaking of the initial data symmetry. In our BNS simulation, we cannot identify a pronounced $m = 1$ instability by examining rest-mass density snapshots in the orbital plane for the whole duration of the simulation. In addition, we perform a simulation of the binary system with an SPH code also adopting the CFC approximation [219,220]. We employ a total of $\approx 3 \times 10^5$ SPH particles[3], while we adopt the same "hybrid" EOS approach. We can clearly identify the $m = 1$ instability in the SPH simulation. We cannot exclude that the instability occurs on longer timescales in the moving-mesh simulation, beyond the simulated time. Still, the $m = 1$ instability seems to be sensitive to the hydrodynamics schemes employed and the overall details of the simulation. We highlight that we do not impose any symmetries in our simulation, namely we simulate the whole 3D domain. This is crucial because the $m = 1$ instability violates the π-symmetry of the initial data. As a result, imposing certain symmetries to the simulated numerical domain[4] can fully suppress the instability.

We now focus on the rotational profile of the merger remnant in the equatorial plane. In Fig. 5.4 we present the time- and azimuthially-averaged angular velocity Ω at different times in the post-merger phase[5]. Originally, the center of the remnant exhibits the highest angular velocity. The central peak gradually decreases, as angular momentum redistributes in the remnant. We notice that an off-center peak emerges at a radial distance of ≈ 4 km, roughly 28 ms after t_{merg}. Angular momentum transfer towards larger radial distances shifts the position of the off-center peak. By the end of the simulation time, the off-center peak has moved outwards to a radial distance of ≈ 7 km. The rotational profiles agree qualitatively with results from independent simulations (see e.g. [137, 141, 165, 268]), but Ω evolves over longer timescales, which clearly suggests that angular momentum redistributes at a slower rate. Very high resolution simulations also result in an overall slower evolution of the angular velocity [168]. We note, however, that the simulations in [168] use a different EOS, while they also take magnetic fields into account. Hence, a direct comparison is not

---

[3] We note that a comparison between the number of SPH particles and the number of cells in a grid-based application is not necessarily meaningful. SPH computes quantities based on a number of "neighbour" particles and thus, effectively, has a lower resolution. In addition, the discussed SPH simulation employs a lower number of particles, compared to the cells in the moving-mesh simulation.

[4] For example, equal-mass BNS systems are sometimes simulated in the literature imposing reflection symmetry with respect to the orbital plane and π-symmetry with respect to the axis normal to the orbital plane, i.e. only the $x, z > 0$ region is simulated.

[5] We define the angular velocity as $\frac{xv^y - yv^x}{\sqrt{x^2+y^2}}$, where $v^i = u^i/u^0$ is the coordinate velocity. We determine all quantities with respect to the center of mass of high-density matter with $\rho > 0.95 \times \rho_{\mathrm{max}}$. To construct the rotational profiles shown in Fig. 5.4, we average the angular velocity along the azimuthial direction and over a 1 ms time window. Since we employ an unstructured mesh, we sample the angular velocity on a polar grid centered at the (previously described) high-density matter center of mass, which greatly simplifies the angular averaging.

straightforward.

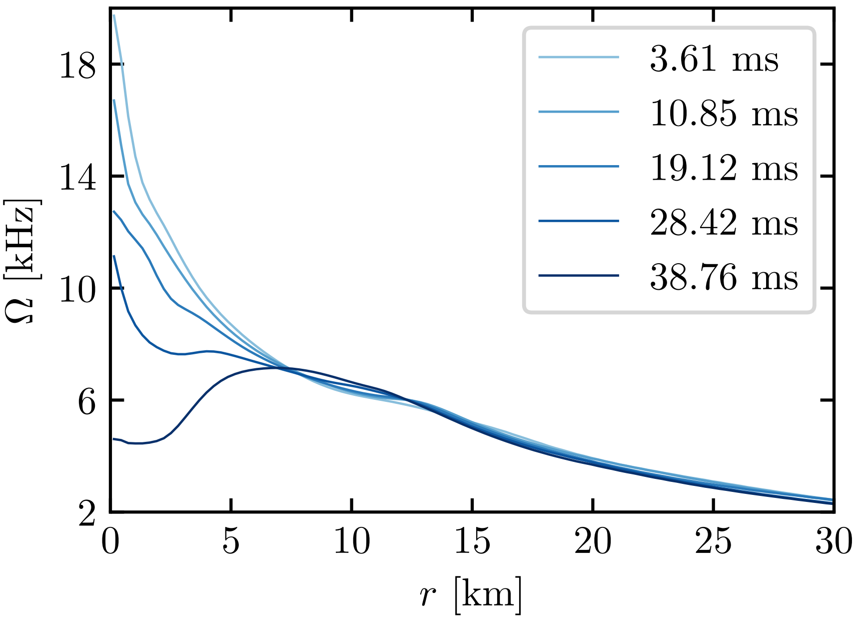

Figure 5.4: Time- and azimuthially-averaged angular velocity Ω on the equatorial plane at various times after merging. Time windows of 1 ms are considered for the averaging. The times included in the legend refer to the midpoint of the considered time interval for each line. Adapted from [196].

Overall, we find that the general dynamics of our moving-mesh simulation qualitatively agree with independent SPH and Eulerian fixed-grid results. Notably, the quasi-radial oscillations and the double-core structure survive for longer times. Furthermore, the rotational profile or the remnant also evolves slower and an off-center angular velocity peak appears only at the late stages of our simulation. That is, angular momentum redistributes over longer timescales. These characteristics suggest that the moving-mesh setup, which we employ, features lower numerical viscosity. This point is further supported by the discussion on the GW signal damping in Section 5.3.2.

Finally, we consider the resolution of our simulation. In Section 5.2 we remark that we employ roughly 1.7×10^6 cells, which roughly follow the mass distribution within the system. In addition, we employ a number of refinement and derefinement criteria based on the mass content of each cell, the cell shape and the overall local geometry of the mesh. Hence, the volume of cells varies throughout the numerical domain, while cells also do not have a fixed shape during the simulation. This makes it practically impossible to define a single resolution. We can however focus on specific regions of the numerical domain and, under some assumption for the cell shape, estimate the local resolution. We consider material with $\rho > 0.5 \times \rho_{\mathrm{max}}$ at a given time and compute the average cell volume. Assuming that cells are spheres, we compute the mean cell radius. The distance between cell centers of neighbouring cells can then be estimated as twice the mean cell radius. We consider this estimate to be indicative of the local resolution. Focusing on the post-merger phase, the mean distance between cell centers is approximately $0.11\ M_{\odot} \approx 162$ m in regions with $\rho > 0.5 \times \rho_{\mathrm{max}}$. This number provides only an estimate of the local resolution. Naturally, some cells have greater or smaller volume than what this number indicates. The reported resolution is roughly comparable to what is employed nowadays in BNS simulations, although with high-order schemes. Performing higher resolution simulations is part of our future plans. Given the modest computational demand of our simulation (a few weeks on 192 cores) higher resolutions are well achievable.

5.3.2. Gravitational waves

We now focus on the GW emission from the system. Figure 5.5 presents the plus polarization of the GW signal along the polar direction[6]. We assume that the system is at a distance of 40 Mpc. Similarly to Section 5.3.1, time in figures is expressed with respect to the moment of merging t_{merg} (indicated with a vertical dashed line in Fig. 5.5). During the inspiral, the emitted GWs have a frequency of two times the orbital frequency. As the orbital separation decreases, the orbital frequency and, it turn, the GW frequency increases. Similarly, the amplitude of the GW signal increases, until it becomes maximum at the moment of merging. Due to the collision of the two NSs, a number of modes are excited in the remnant, which contribute to the post-merger GW signal.

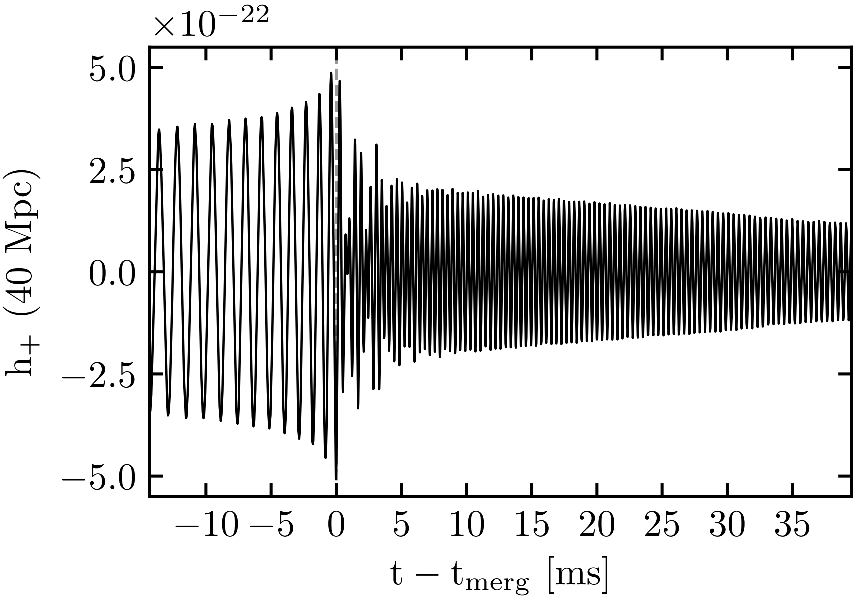

Figure 5.5: Plus polarization of the binary system's GW signal at a distance of 40 Mpc. The time of merging is indicated with a dashed line. Adapted from [196].

We note that the amplitude of the GW signal decreases very slowly during the almost 40 ms of post-merger evolution. This is in full agreement with our observation in Section 5.3.1, that our simulation features low numerical diffusivity. By employing the GW signal modelling from [272], we estimate the damping time to be $\tau_{\mathrm{peak}} \approx$

---

[6] We extract the GW signal based on the quadrupole formula, which is known to underestimate the amplitude by a few ten percent (30 – 40% reported in [268], likely closer to 100% based on examination of more recent simulations [272]). Hence, we multiply the GW signal by a (moderate) numerical factor 1.4.

48 ms. For comparison, the SPH calculation briefly discussed in Section 5.3.1 results in $\tau_{\text{peak}} \approx 10.5$ ms for the same binary system. In [272] damping times for a variety of masses are presented, based on full general relativistic simulations. The damping times, extracted for all their simulated models and employed resolutions, are always smaller than 11 ms (the binary system with total gravitational mass of 2.7 $M_\odot$ yields $\tau_{\text{peak}} \approx 7$ ms). A direct comparison is however not possible, because in [272] a different EOS is employed.

Figure 5.6 shows the GW spectrum based on a Fourier transform of $h_+(40\text{ Mpc})$. The solid line refers to the full GW signal from the whole simulation as presented in Fig. 5.5. The dotted line takes into account only the signal for $t > t_{\text{merg}}$. Furthermore, with the upper and lower dash-dotted lines we denote the design sensitivities of Advanced LIGO [189] and the Einstein Telescope [238], respectively. We identify a number of different peaks in the GW spectrum. The dominant oscillation frequency is found at $f_{\text{peak}} = 2.56$ kHz. This is in good agreement with the SPH calculation for which we extract $f_{\text{peak}} = 2.62$ kHz. We note that the features in the moving-mesh GW spectrum are more pronounced compared to SPH spectrum, possibly because the GW signal is damped slower.

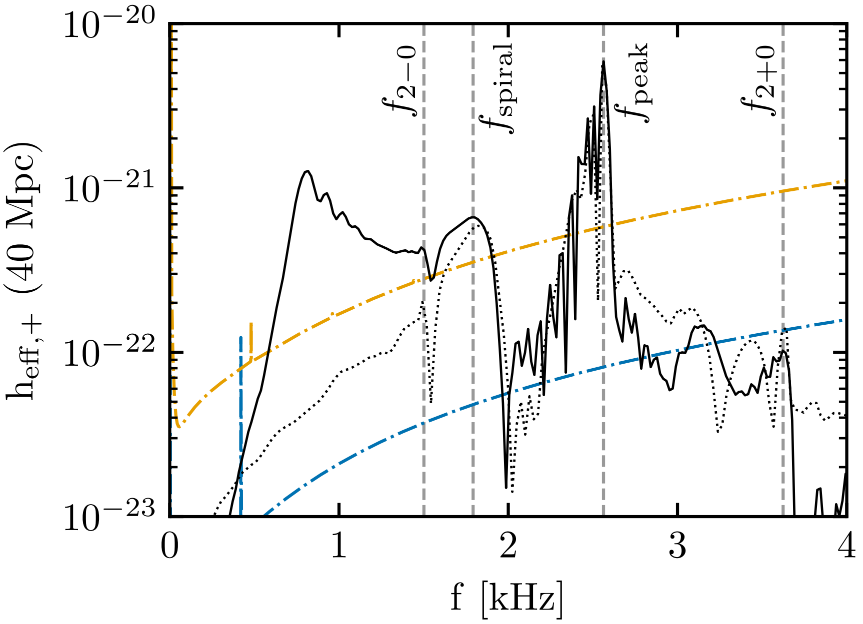

Figure 5.6: GW spectrum of the plus polarization for the binary simulation. The solid line refers to the full simulation, while the dotted line is the spectrum of the post-merger phase alone. The vertical dashed lines mark the position of four peaks in the spectrum, i.e. f_{peak}, f_{spiral}, f_{2-0} and f_{2+0}. The upper (orange) and lower (blue) dash-dotted curves indicate the design sensitivity of Advanced LIGO [189] and the Einstein Telescope [238], respectively. Figure adapted from [196].

We also compare the dominant post-merger oscillation frequency to full general relativistic, fixed-grid simulations of the same binary system from the CORE database[7] [94]. The database includes two simulations with finest grid resolutions of 0.125 $M_\odot$ and 0.083 $M_\odot$ for our setup (see [239, 242] for more details). We extract

---

[7] `http://www.computational-relativity.org`

$f_{\mathrm{peak}} = 2.57$ kHz and $f_{\mathrm{peak}} = 2.65$ kHz for these two resolutions respectively, which are both in good agreement with our result. We note that the full temperature-dependent EOS is employed in these Eulerian grid-based simulations. In principle, one can expect differences up to a few percent in the extracted f_{peak} between calculations which employ a "hybrid" EOS approach and simulations where thermal effects are treated consistently in the EOS [46].

In Fig. 5.6 we also indicate a number of subdominant features, some of which can, in principle, be observed based on the sensitivity curves of the detectors. We denote the most prominent of the secondary features in our simulation by f_{spiral}. The spiral mode originates from the rotation of two antipodal tidal bulges, which form immediately after merging. These lower density tidal tails rotate slower compared to the high-density material [50]. We extract $f_{\mathrm{spiral}} = 1.79$ kHz in our moving-mesh simulation. In the respective SPH calculation, we obtain a frequency roughly 200 Hz higher for the spiral mode. The difference in the extracted values for f_{spiral} suggests a dependence of the feature on the employed hydrodynamics schemes, given that both the moving-mesh and the SPH simulations employ practically the same metric modules.

We mark two more frequencies in Fig. 5.6 as f_{2+0} and f_{2-0}. These peaks originate from the non-linear coupling of the dominant oscillation mode f_{peak} to the quasi-radial mode f_0 [275] and have frequencies $f_{2\pm0} \approx f_{\mathrm{peak}} \pm f_0$. In order to identify these couplings in the spectrum, we extract f_0 based on a Fourier analysis of the lapse function evolution in the post-merger phase. Then, based on the extracted values for f_{peak} and f_0, we locate the peaks in the spectrum occurring at roughly $f_{\mathrm{peak}} \pm f_0$.

Part III

Frequency deviations in universal relations

Preface

Introductory and concluding remarks for the results discussed in Chapter 6 can be found in Sections 1.3 and 7.2, respectively. Appendix A provides more details relevant to the work presented here. The bulk of this study follows [197], published in *Physical Review D* 104, 043011[1]. The text, figures and tables have been modified and adapted to suit this thesis.

---

[1] `https://doi.org/10.1103/PhysRevD.104.043011`

6. Gravitational wave frequency deviations

6.1. Setup and data

In this chapter we consider fluid oscillations in two distinct physical systems. We employ the perturbative approach, discussed in Section 2.5.2, to compute GW frequencies originating from the fundamental quadrupole mode in static isolated stars. In addition, we extract the GW frequencies corresponding to the dominant fluid oscillation in BNS merger remnants based on 3D relativistic hydrodynamics simulations with an SPH code [219, 220]. The two data sets are presented below.

6.1.1. Linear quadrupole perturbations

In Section 2.5.2 we discuss nonlinear oscillations in NSs, placing the attention on the fundamental quadrupole $(l, m) = (2, 0)$ mode, i.e. the $f-$mode. To compute the perturbative GW frequencies, which we denote as f_{pert}, we employ the code presented in [198]. We consider a number of different EOSs (see Section 6.1.3). For each EOS we compute the $f-$mode frequency for stellar configurations with masses in the range $[1.1, 1.9]\ M_\odot$ with a step of $0.05\ M_\odot$. Our main goal is to compare with GW frequencies from BNS remnants. The most massive binary systems taken into account in this study have a total gravitational mass of $3\ M_\odot$ (see Section 6.1.2). The maximum rest-mass densities in remnants of such massive systems are similar to the central rest-mass densities admitted by static NSs with masses up to roughly $1.9\ M_\odot$. Hence, even though all the EOSs considered here can produce stellar models with masses above $1.9\ M_\odot$, we do not include these models in our study.

6.1.2. Binary neutron star data sets

Our binary systems data sets consist of calculations with a 3D SPH code, which adopts the CFC approximation, employing results from [45, 48, 219, 220]. In each simulation we employ a total of roughly 3×10^5 SPH particles and start from irrotational binaries (i.e. the stars have initially no intrinsic spin) about three orbits before the merger. All but 6 of the EOS models that we employ provide the full temperature dependence. If the full temperature dependence is not provided, we supplement the EOS with a thermal ideal-gas component with an index $\Gamma_{\mathrm{th}} = 1.75$. We provide a quick overview of the EOS models we employ in Section 6.1.3.

The data set consists of 57 equal-mass binary systems. Table 6.1 summarizes which EOSs are simulated, as well as the total mass of each system. Binary systems with a total mass of $M_{\mathrm{tot}} = 3\ M_\odot$ result in a prompt collapse to a black hole for most of the EOSs that we consider [41]. Hence, the set of $1.5 + 1.5\ M_\odot$ systems is comparatively smaller than the sets referring to different total binary masses. For each one of the 57 binary systems, we extract the dominant post-merger GW frequency, which we denote by f_{peak}. All systems are simulated up to roughly 20 ms after merging, which suffices for an accurate determination of f_{peak}. We verify that the dominant post-merger frequency is mostly unaffected by the initial orbital separation and resolution for a some of the binary systems. This aspect is furthered discussed in Section 6.3.1, while more simulations and details can be found in e.g. [44, 45].

Table 6.1: Summary of EOSs simulated for each binary system mass. The first column indicates binary system masses. The second column presents all EOSs simulated for the respective binary mass. The table is adapted from [197].

System masses $[M_\odot]$	Simulated EOSs
$1.2 + 1.2$	APR, BHBLP, BSK20, BSK21, DD2, DD2F, DD2Y, WFF2, LS220, LS375, GS2, SFHO, SFHOY, SFHX, SLY4, TMA
$1.35 + 1.35$	ALF2, APR, BHBLP, BSK20, BSK21, DD2, DD2F, DD2Y, WFF2, LS220, LS375, GS2, NL3, SFHO, SFHOY, SFHX, SLY4, TM1, TMA
$1.4 + 1.4$	APR, BHBLP, BSK20, BSK21, DD2, DD2F, DD2Y, WFF2, LS220, LS375, GS2, SFHO, SFHOY, SFHX, SLY4, TMA
$1.5 + 1.5$	BHBLP, BSK21, DD2, LS375, GS2, TMA

6.1.3. Equations of state

We compute $f-$mode frequencies for a total of 20 EOSs (ALF2 [18, 247], APR [16], BHBLP [34], BSK20 [132], BSK21 [132], DD2 [150, 297], DD2F [21, 296, 297], DD2Y [118, 205], WFF2 [313], LS220 [181], LS375 [181], GS1 [262], GS2 [262], NL3 [150, 177], SFHO [274], SFHOY [118, 205], SFHX [274], SLY4 [97], TM1 [149, 277], TMA [149, 288]). We extract the post-merger GW frequencies for a marginally smaller subset of these EOSs (see Section 6.1.2 and Table 6.1).

Figure 6.1 presents the gravitational mass M versus radius R relation for all the EOSs which we consider. All of the employed EOSs are fully compatible with current observational constraints on the maximum NS mass at the two sigma level [24, 28, 85, 90, 190]. Furthermore, most EOSs are compatible with the less strict tidal deformability constraint originating from the analysis of the inspiral of GW170817, namely that the tidal deformability of 1.37 $M_\odot$ stars is smaller than 800 [6, 10]. Six EOSs (LS375, GS1, GS2, NL3, TM1, TMA) are incompatible with the tidal deformability constraint and are depicted with dashed lines in Fig. 6.1. Nevertheless, we take them into account to increase the size of the data set. Employing a larger set of EOSs tests our relations more extensively and further strengthens their reliability. We do not include any quark or hybrid EOSs in our analysis. Clearly, the EOS sample under consideration covers a broad part of the allowed $M - R$ parameter space.

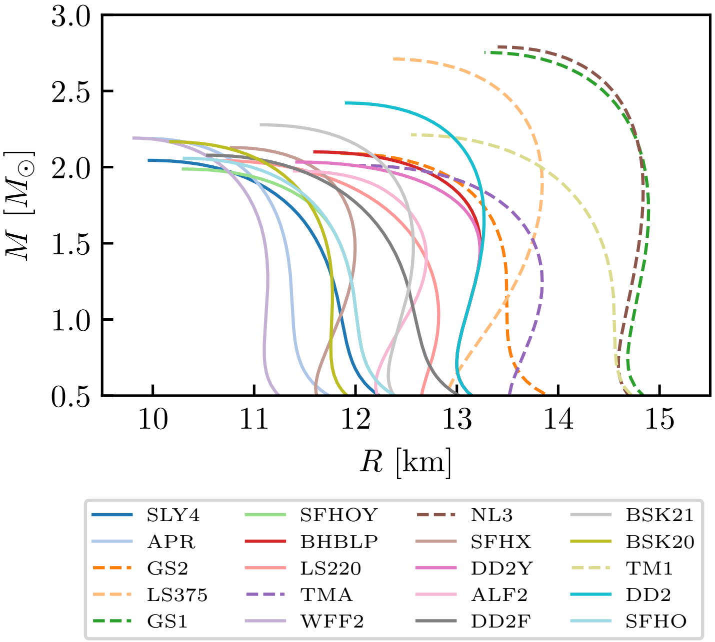

Figure 6.1: Gravitational mass-radius relations for all EOSs employed in this chapter. EOSs which are incompatible with current tidal deformability constraints are shown with dashed lines. Figure adapted from [197].

6.2. Accuracy of empirical relations

Relations between properties of the GW signal and stellar parameters are the basis of GW asteroseismology. In the context of static, isolated stars, many such relationships have been proposed, which exhibit a different degree of accuracy. For example, the $f-$mode GW frequency f_{pert} has been related to parameters like the mass M, radius R, moment of inertia I and tidal deformability Λ (see e.g. [22, 68, 185, 295]). Turning to BNS systems, a number of relations involving f_{peak} exist referring to systems of different masses and mass ratios [44, 45, 57, 59, 281, 305]. These relations can describe either a broad range of masses of focus on a fixed mass.

Such relations allow us to extract information about the stellar parameters of the system, based on the measurement of GW frequencies. The scatter in these relations is a source of error and needs to be taken into account when employing such relations to determine stellar parameters. In this section, we examine the accuracy of a number of different relations using a consistent data set, which allows for an objective comparison between different relations. Initially, we focus on isolated NSs and discuss relations proposed in the literature, as well as relations newly introduced in [197]. We investigate whether these relations carry information about the high-density EOS by looking into new relations, which excise the low-density parts of the star and focus on the properties of the innermost region. In addition, we extend the discussion to relations for binary systems.

We consider the maximum and mean deviation between the data points and the corresponding fit to the data, as metrics to quantify the scatter of a given relation. The maximum deviation captures extreme models. Hence, it serves as a conservative estimate of the accuracy of a relation, i.e. the maximum error introduced by the relation if it is employed in a GW observation. The maximum deviation is biased by extreme models and does not necessarily capture how most of the points distribute with respect to the fit, which is why we also present the mean deviation. We note, however, that the EOS sample is not a statistical ensemble. As a result, the mean deviation might not be fully representative of the error. In all cases, for completeness, we include both the maximum and mean deviation. Generally, the behavior of the two figures of merit is consistent.

6.2.1. Isolated neutron stars

We start by discussing relations in the case of isolated stars, namely between f_{pert} and stellar parameters. Table 6.2 summarizes all the relations discussed in this section, including the maximum and mean deviation for each relation based on our data.

Some very well known relations between f_{pert} and the stellar mass M and radius R exist. Andersson and Kokkotas proposed a correlation between f_{pert} and the mean density of the star [22]. Later, Tsui and Leung employed a different scaling, which relates the mass-scaled frequency Mf_{pert} to the compactness M/R [295]. This functional form leads to accurate relations for both f_{pert}, as well as the damping time τ_{damp}. Moreover, it can successfully be applied to frequencies and damping times of other families of modes. Figures 6.2a-6.2b show both relations based on our perturbative $f-$mode data. In both diagrams we include second-order fits to our data, shown as solid curves. We construct fits based on our data to quantify the data scatter around them. Employing a consistent data set for all the relations enables an accurate comparison between them[1]. Based on the deviations of each relation (see Table 6.2), the relation involving the mass-scaled frequency is more accurate. However, both relations still exhibit some sizable data scatter.

Lau et al. [185] suggested a different relation, which involves the moment of inertia. They remarked that quark stars were not accurately described by previously proposed relationships, because the stellar structure of quark stars and NSs differs. Instead of employing the compactness M/R, they defined an effective compactness based on the moment of inertia I. Their main motivation was that I is sensitive to the matter distribution within the star and thus better captures the stellar structure for both types of stars. In Table 6.2 we present both second- and fourth-order fits to our data[2], following the functional form proposed in [185]. We note that the relation is very tight, while its accuracy remains practically the same as we increase the order of the fit.

Chan et al. [68] proposed that f_{pert} should tightly correlate with the tidal deformability Λ (see also [309]). The moment of inertia tightly correlates with the tidal deformability based on the I-Love-Q relations [316], while the relation involving f_{pert} and I is also highly accurate [185]. In [68] they suggest a relation the form $Mf_{\text{pert}}(\ln\Lambda)$.

---

[1] To ensure an accurate comparison, we report all deviations in terms of absolute frequencies, even for relations with mass-scaled frequencies.

[2] We note that [185] presented a second-order fit.

Table 6.2: Relations between $f-$mode frequencies of isolated stars and various stellar parameters. The first column includes references to the work where the respective relation has been proposed. The second column indicates if a relation is shown in a figure or only discussed in the main text. The third column presents the relations. The fourth and fifth columns list the mean and maximum deviation for the corresponding relation, respectively. In terms of units, frequencies are in kHz, masses in $M_\odot$, radii in units of $GM_\odot/c^2$, moments of inertia in units of $G^2M_\odot^3/c^4$, while the tidal deformability Λ is dimensionless. Table adapted from [197].

Reference	Position	Fit	Mean dev. [Hz]	Max dev. [Hz]
[22]	Fig. (6.2a)	$f_{\rm pert} = -0.133 + 47.23\sqrt{\frac{M}{R^3}} - 173.2\frac{M}{R^3}$	31	102
This work	Fig. (6.4a)	$f_{\rm pert} = -0.2 + 37.68\sqrt{\frac{M}{(R^{90\%})^3}} - 92.14\frac{M}{(R^{90\%})^3}$	12	34
This work	Text	$f_{\rm pert} = -0.106 + 37.15\sqrt{\frac{M^{\rm cc}}{(R^{\rm cc})^3}} - 57.56\frac{M^{\rm cc}}{(R^{\rm cc})^3}$	19	54
[295]	Fig. (6.2b)	$M f_{\rm pert} = -0.427 + 14.95\frac{M}{R} + 14.43\left(\frac{M}{R}\right)^2$	19	49
This work	Fig. (6.4b)	$M f_{\rm pert} = -0.626 + 13.69\frac{M}{R^{90\%}} + 11.67\left(\frac{M}{R^{90\%}}\right)^2$	10	34
This work	Text	$M^{\rm cc} f_{\rm pert} = -0.586 + 13.67\frac{M^{\rm cc}}{R^{\rm cc}} + 17.92\left(\frac{M^{\rm cc}}{R^{\rm cc}}\right)^2$	18	64
[185]	Text	$M f_{\rm pert} = -0.117 + 3.966\sqrt{\frac{M^3}{I}} + 18.97\frac{M^3}{I}$	0.9	5
[185]	Text	$M f_{\rm pert} = -0.117 + 4.161\sqrt{\frac{M^3}{I}} + 16.93\frac{M^3}{I} + 6.995\left(\frac{M^3}{I}\right)^{3/2} - 7.855\left(\frac{M^3}{I}\right)^2$	0.8	5
This work	Fig. (6.3)	$M f_{\rm pert} = -0.656 + 12.26\Lambda^{-1/5} - 5.471\Lambda^{-2/5}$	3	17
This work	Text	$M f_{\rm pert} = -0.24 + 7.726\Lambda^{-1/5} + 11.877\Lambda^{-2/5} - 27.653\Lambda^{-3/5} + 15.387\Lambda^{-4/5}$	0.12	0.7
[68]	Text	$M f_{\rm pert} = 6.939 - 9.294\times10^{-1}\ln\Lambda + 3.267\times10^{-2}\left(\ln\Lambda\right)^2$	4	19
[68]	Text	$M f_{\rm pert} = 5.965 - 0.2814\ln\Lambda - 0.1214\left(\ln\Lambda\right)^2 + 1.555\times10^{-2}\left(\ln\Lambda\right)^3 - 5.619\times10^{-4}\left(\ln\Lambda\right)^4$	0.14	0.8

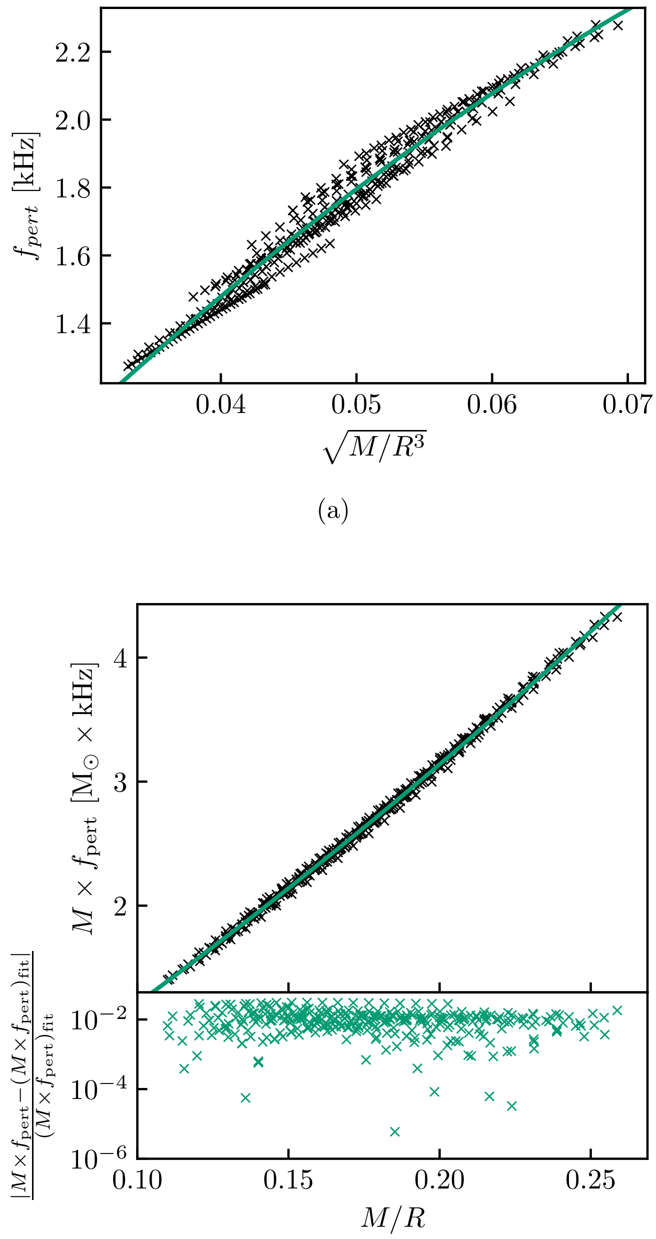

(a)

(b)

Figure 6.2: Relations between the $f-$mode frequency, the mass and the radius of non-rotating stellar configurations. Panel (a) shows $f_{\rm pert}$ versus the mean density of the star, which was originally proposed in [22]. Panel (b) displays the relation between the mass-scaled frequency and the compactness as suggested in [295]. In both panels we present a second-order fit to our data as a solid line. In panel (b) we also include the fractional error of the data with respect to the fit. Figure adapted from [197].

In addition, we note that the compactness and $\Lambda^{-1/5}$ are directly related. Hence, a relation of the form $Mf_{\rm pert}(\Lambda^{-1/5})$ should exist. Figure 6.3 shows a relation of this functional form. The solid line depicts a second-order fit to the data. The mean and maximum deviations with respect to the fit are 3 Hz and 17 Hz, which supports that this relation is highly accurate. We also construct a fourth-order fit (see Table 6.2), similarly to what was presented in [68]. The use of either $\Lambda^{-1/5}$ or $\ln\Lambda$ leads to very tight fits.

Comparing the accuracy of relations involving the moment of inertia I and the tidal deformability (either $\Lambda^{-1/5}$ or $\ln\Lambda$), we note that I leads to tighter second-order fits. However, contrary to the fit involving I, the accuracy of tidal deformability fits improve as we increase the order. Thus, fourth-order relations employing either $\Lambda^{-1/5}$ or $\ln\Lambda$ are tighter compared to the fourth-order relation involving I and the most accurate of all the functional forms that we examine.

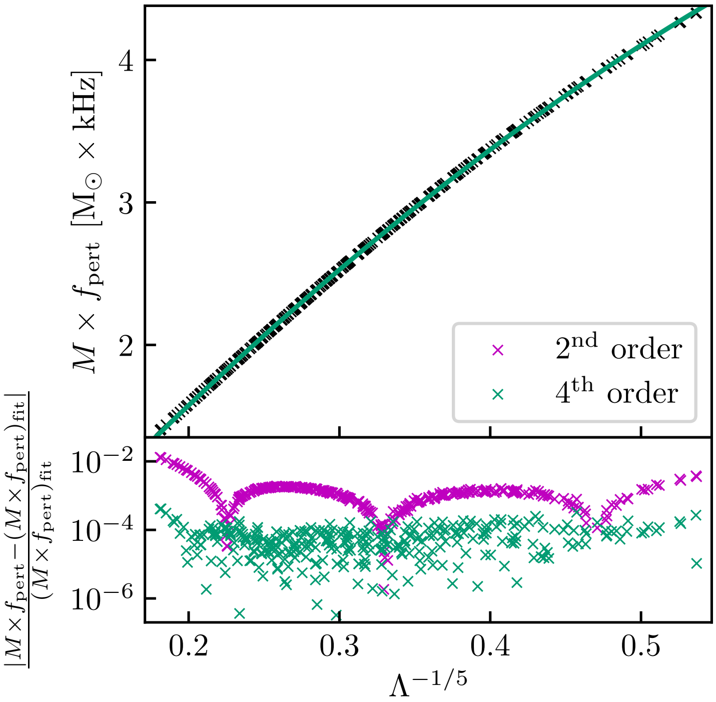

Figure 6.3: Relation between the mass-scaled $f_{\rm pert}$ and $\Lambda^{-1/5}$. The solid curve shows a second-order fit to our data. We also present the fractional errors for both the second-order fit shown in the plot, as well as the fourth-order fit discussed in the text and included in Table 6.2. The legend refers to the fractional errors and explains the colors of the symbols. Figure adapted from [197].

By examining the accuracy of all reported relation in Table 6.2, it is evident that relations involving Λ are more accurate than those connecting the $f-$mode frequency to M and R. Interestingly, compared to the compactness, the tidal deformability is less sensitive to the low-density parts of the star, particularly the crust [125, 235]. In contrast, the radius R is also sensitive to the low-density stellar interior. Naturally, this raises the question whether the scatter admitted by relations involving M and R originates solely from the crust. In order to investigate this point, we define two distinct excision procedures and focus on the high-density parts of the star.

As a first method, we define a new effective radius $R^{90\%}$ as the radius of the sphere which contains 90% of the gravitational mass of the static stellar model. By removing the outermost layers of the star containing 10% of its mass, $R^{90\%}$ is insensitive to the low-density EOS, in particular the crust. Based on this definition, for the various stellar models constructed, we excise the outermost $1.26 - 2.41$ km. Interestingly, for all the EOSs and stellar configurations considered, the pressure at a radial distance

$R^{90\%}$ is $3-5\%$ of the central pressure p_c of the respective stellar model[3]. Hence, an alternative definition could be to define for every star a fixed pressure surface of e.g. $p_* = 0.04 \times p_c$.

We can now examine the accuracy of relations involving M and R, but employing the newly defined radius. Figure 6.4 shows the same relations as in Fig. 6.2, but the mean density and compactness are now defined with respect to $R^{90\%}$. Notably, the accuracy of both relations is increased. This is explicitly shown in Table 6.2, where the mean and maximum deviations are presented for all relations. The improvement is more pronounced in the case of the relation involving the mean density. When considering the sphere containing 90% of the mass, relating $f_{\rm pert}$ to the mean density is equally accurate to relating the mass-scaled $f_{\rm pert}$ to the compactness. Overall, we conclude that the $f-$mode frequency in isolated stars accurately captures the mean density of the innermost part of the star, which contains 90% of its gravitational mass.

As a second excision procedure, we consider the crust-core transition density $\rho_{\rm cc}$ and disregard material with densities below $\rho_{\rm cc}$, i.e. formally the crust. The crust-core transition density is not publicly available for most of the EOS models. Hence, we need to estimate $\rho_{\rm cc}$. The dynamical crust-core transition density correlates with the slope of the symmetry energy L [98]. So, we determine $\rho_{\rm cc}$ by employing its relation to L from [98] and calculating L approximately through the pressure at nuclear saturation density, as given in the EOS table for neutrino-less beta-equilibrium. For each stellar configuration we identify the crust-core transition point and define the radius $R^{\rm cc}$ and mass $M^{\rm cc}$ corresponding to the respective sphere.

Similarly to the first excision method, i.e. via $R^{90\%}$, we examine how the accuracy of relations involving the mean density or compactness changes when these quantities are computed for the core region contained within $R^{\rm cc}$. We provide the new relations and their mean and maximum deviations in Table 6.2. Evidently, employing only the core region improves the accuracy of the relation involving the mean density by a factor of roughly two. The situation is different for the relation with respect to the compactness, where focusing on the core region does not affect the accuracy significantly compared to considering the whole star. We note that this might be related to how we estimate crust-core transition densities. A more accurate determination of $\rho_{\rm cc}$, for every EOS under consideration, can potentially result in both relations becoming tighter.

Overall, we note that excising low-density material through either $R^{90\%}$ or $R^{\rm cc}$ does not completely remove the scatter from relations between $f_{\rm pert}$, M and R. The correlation of the $f-$mode frequency with $\Lambda^{-1/5}$ is still significantly more accurate. Hence, we conclude that the scatter in relations involving the mean density or compactness does not entirely originate from the low-density EOS. This suggests that the way data points distribute with respect to the corresponding fit might encode additional information about the high-density EOS.

6.2.2. Binary neutron star mergers

A number of relations have been proposed also in the case of BNS systems, particularly between the dominant post-merger oscillation frequency $f_{\rm peak}$ and stellar properties of (typically static) stars. The use of properties of static stars is motivated by the fact

---

[3] We note that, even though the pressure at $R^{90\%}$ has dropped to roughly 4% of the central pressure for all stellar models, the density at this radial distance corresponds to about $25-47\%$ of the central rest-mass density ρ_c, namely it exhibits some sizable scatter.

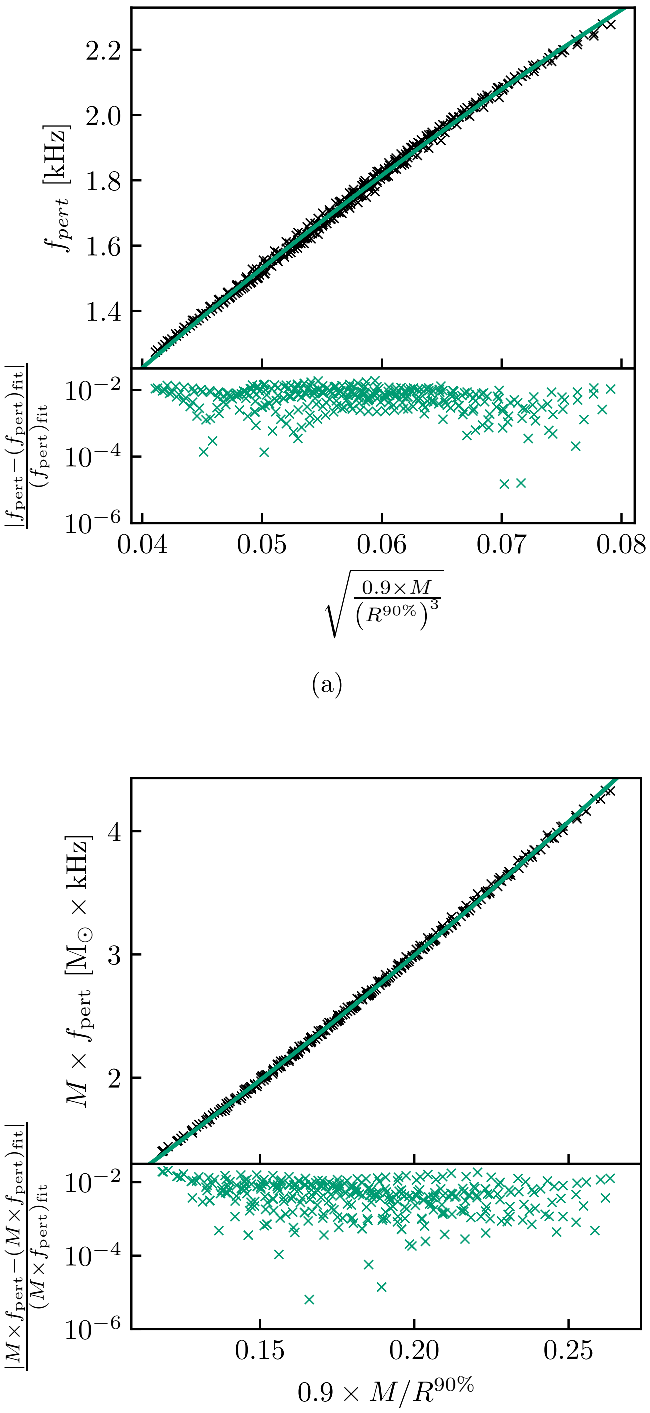

(a)

(b)

Figure 6.4: Same relations as in Fig. 6.2, but the mean density (panel (a)) and compactness (panel (b)) correspond to the sphere containing 90% of the gravitational mass of the corresponding stellar model. Both relations are tighter in comparison to those presented in Fig. 6.2. Adapted from [197].

that one cannot define quantities such as the mass or radius of the merger remnant in an unambiguous way. In [44, 45, 52] tight relations are found between $f_{\rm peak}$ for BNS systems with a fixed mass and the radii of fixed-mass static stars. Mass-scaled relations, which consider a broad range of masses, have also been proposed, but are less tight in comparison to fixed-mass relations [53, 57]. Here we consider relations between f_{peak} and $R^{90\%}$, R^{cc} or $\Lambda^{-1/5}$, motivated by our observation that, in the case of isolated stars, relations involving these quantities are more accurate than relations with the radius R.

Table 6.3 provides fit parameters and the mean and maximum deviation for all the relations discussed in this section. We consider relations of the form $f_{\mathrm{peak}}(R_x)$, $f_{\mathrm{peak}}(R_x^{90\%})$, $f_{\mathrm{peak}}(R_x^{\mathrm{cc}})$ and $f_{\mathrm{peak}}(\Lambda_x^{1/5})$ for binary systems with a fixed mass. We provide relations for every total binary mass considered here (see Table 6.1), while x refers to the mass of a static star. For each binary system we pick x such that the central densities of the static stellar models are roughly comparable with the maximum rest-mass densities exhibited in the first few milliseconds in the post-merger phase of the binary. We discuss this point more extensively in Appendix A. Based on this procedure, we relate binary systems with a total mass of 2.4, 2.7, 2.8 and 3 $M_{\odot}$ to static stars with a mass of 1.4, 1.6, 1.7 and 1.75 $M_{\odot}$, respectively. As an illustrative case, we present relations involving R, $R^{90\%}$ and $\Lambda^{1/5}$ for $1.2 + 1.2$ $M_{\odot}$ systems in Fig. 6.5.

In Table 6.3 we express all mean and maximum deviations in terms of frequencies, which enables a direct comparison between the various relations. We compare the accuracy of relations for each binary system, i.e. for fixed total binary masses. Evidently, relations involving $R^{90\%}$ or $\Lambda^{-1/5}$ are more accurate compared to relations depending on R or R^{cc} (see Table 6.3 and Fig. 6.5). We remark, however, that deviations depend up to some extent on the chosen fiducial mass x. In particular, the chosen fiducial mass x is closer to the optimal mass for relations involving $R^{90\%}$ than for relations with R^{cc} (see Table A.1). Overall, we note that relations between f_{peak} and $\Lambda^{-1/5}$ are, marginally, the most accurate. This observation aligns with the discussion in the previous section, which focuses on static stars and a broad range of masses. In the case of $1.5 + 1.5$ $M_{\odot}$ systems, relations involving R are similarly accurate as relations w.r.t. $R^{90\%}$ or $\Lambda^{-1/5}$. The underlying reason for this behavior is that the data set of $1.5 + 1.5$ $M_{\odot}$ systems is smaller compared to the sets referring to less massive binary systems. In Table 6.3 we also include for each system a relation between f_{peak} and the tidal deformability of the inspiraling stars. In all cases this results in less tight relations compared to picking a higher fiducial mass. The optimal mass range for each relation and binary system is discussed more extensively in Appendix A (see also [305] for relations considering a range of binary masses).

The maximum deviation in such relations serves as an estimate for the error. Hence, we conclude that extracting $R^{90\%}$ can be up to twice as accurate compared to determining R. In the scenario of a GW frequency measurement, extracting stellar properties of a static star relies on the inverted relations, e.g. $R_x(f_{\mathrm{peak}})$ or $R_x^{90\%}(f_{\mathrm{peak}})$. By examining the $R_x^{90\%}(f_{\mathrm{peak}})$ relations, we find a mean deviation of roughly 70 m for all binary systems. As a result, an observation of an equal-mass binary system can accurately determine $R^{90\%}$ of a fixed-mass static star. Notably, just like the radius R, the newly defined radius $R^{90\%}$ serves as a proxy for the EOS, particularly the high-density regime.

Table 6.3: Relations between $f_{\rm peak}$ and various stellar parameters referring to static stars for a chosen fiducial mass. The binary system and independent variable for each relation are given in the first and second column, respectively. The third third column lists the fits, while the fourth and fifth columns provide the mean and maximum deviation for each fit, respectively. Frequencies are in kHz, all radii (i.e. R, $R^{90\%}$ and $R^{\rm cc}$) are in km, while $\Lambda^{1/5}$ is dimensionless. Deviations for all relations are given in Hz, which enables a direct comparison between them. The table is adapted from [197].

Binary masses $[M_\odot]$	Independent variable	Fit	Mean dev. [Hz]	Max dev. [Hz]
$1.2+1.2$	R	$f_{\rm peak} = 10.428 - 8.347\times10^{-1}R_{1.4} + 1.749\times10^{-2}R_{1.4}^2$	41	109
$1.2+1.2$	$R^{90\%}$	$f_{\rm peak} = 12.963 - 1.449R_{1.4}^{90\%} + 4.604\times10^{-2}\left(R_{1.4}^{90\%}\right)^2$	31	58
$1.2+1.2$	$R^{\rm cc}$	$f_{\rm peak} = 16.526 - 1.9593R_{1.4}^{\rm cc} + 6.568\times10^{-2}\left(R_{1.4}^{\rm cc}\right)^2$	45	112
$1.2+1.2$	$\Lambda^{1/5}$	$f_{\rm peak} = 9.74 - 2.994\Lambda_{1.4}^{1/5} + 2.767\times10^{-1}\Lambda_{1.4}^{2/5}$	18	44
$1.2+1.2$	$\Lambda^{1/5}$	$f_{\rm peak} = 9.74 - 2.432\Lambda_{1.2}^{1/5} + 1.771\times10^{-1}\Lambda_{1.2}^{2/5}$	39	72
$1.35+1.35$	R	$f_{\rm peak} = 12.61 - 1.134R_{1.6} + 2.87\times10^{-2}R_{1.6}^2$	48	84
$1.35+1.35$	$R^{90\%}$	$f_{\rm peak} = 12.63 - 1.306R_{1.6}^{90\%} + 3.79\times10^{-2}\left(R_{1.6}^{90\%}\right)^2$	31	60
$1.35+1.35$	$R^{\rm cc}$	$f_{\rm peak} = 14.653 - 1.5432R_{1.4}^{\rm cc} + 4.597\times10^{-2}\left(R_{1.4}^{\rm cc}\right)^2$	47	110
$1.35+1.35$	$\Lambda^{1/5}$	$f_{\rm peak} = 9.063 - 2.912\Lambda_{1.6}^{1/5} + 0.276\Lambda_{1.6}^{2/5}$	26	61
$1.35+1.35$	$\Lambda^{1/5}$	$f_{\rm peak} = 8.886 - 2.147\Lambda_{1.35}^{1/5} + 1.397\times10^{-1}\Lambda_{1.35}^{2/5}$	46	88
$1.4+1.4$	R	$f_{\rm peak} = 12.61 - 1.085R_{1.7} + 2.54\times10^{-2}R_{1.7}^2$	53	151
$1.4+1.4$	$R^{90\%}$	$f_{\rm peak} = 15.16 - 1.716R_{1.7}^{90\%} + 5.51\times10^{-2}\left(R_{1.7}^{90\%}\right)^2$	38	130
$1.4+1.4$	$R^{\rm cc}$	$f_{\rm peak} = 16.389 - 1.7824R_{1.4}^{\rm cc} + 5.467\times10^{-2}\left(R_{1.4}^{\rm cc}\right)^2$	53	148
$1.4+1.4$	$\Lambda^{1/5}$	$f_{\rm peak} = 11.11 - 4.584\Lambda_{1.7}^{1/5} + 5.821\times10^{-1}\Lambda_{1.7}^{2/5}$	36	124
$1.4+1.4$	$\Lambda^{1/5}$	$f_{\rm peak} = 9.34 - 2.342\Lambda_{1.4}^{1/5} + 1.533\times10^{-1}\Lambda_{1.4}^{2/5}$	65	159
$1.5+1.5$	R	$f_{\rm peak} = -34.89 + 6.19R_{1.75} - 2.519\times10^{-1}R_{1.75}^2$	29	76
$1.5+1.5$	$R^{90\%}$	$f_{\rm peak} = -7.534 + 2.275R_{1.75}^{90\%} - 1.189\times10^{-1}\left(R_{1.75}^{90\%}\right)^2$	25	64
$1.5+1.5$	$R^{\rm cc}$	$f_{\rm peak} = -7.829 + 2.1565R_{1.4}^{\rm cc} - 1.0424\times10^{-1}\left(R_{1.4}^{\rm cc}\right)^2$	41	88
$1.5+1.5$	$\Lambda^{1/5}$	$f_{\rm peak} = 3.74 + 0.755\Lambda_{1.75}^{1/5} - 3.798\times10^{-1}\Lambda_{1.75}^{2/5}$	30	73
$1.5+1.5$	$\Lambda^{1/5}$	$f_{\rm peak} = -9.88 + 8.624\Lambda_{1.5}^{1/5} - 1.427\Lambda_{1.5}^{2/5}$	52	109

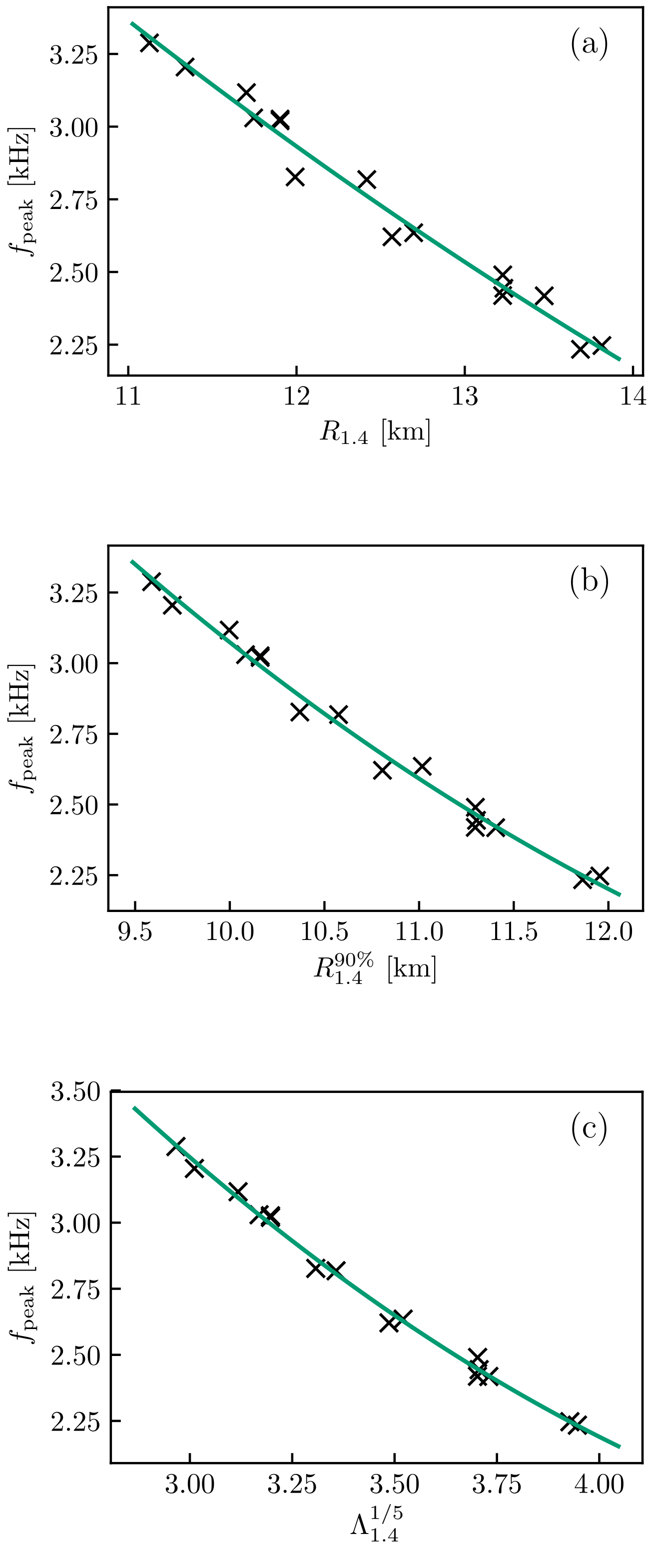

Figure 6.5: Post-merger frequencies f_{peak} for 1.2 + 1.2 $M_{\odot}$ binary systems versus various stellar parameters of 1.4 $M_{\odot}$ static stars described by different EOSs. The independent variable in the top panel is the radius $R_{1.4}$, in the middle panel the radius including 90% of the mass $R_{1.4}^{90\%}$ and in the bottom panel the fifth-root of the tidal deformability $\Lambda_{1.4}^{1/5}$. Adapted from [197].

6.3. Frequency deviations

In this section we examine in detail how individual data points scatter with respect to the corresponding fit to all data points and show that the exact point distribution encodes additional information.

6.3.1. Scatter in frequency relations

Figure 6.5 presents empirical relations between f_{peak} for $1.2 + 1.2\ M_{\odot}$ systems and three independent variables, namely R, $R^{90\%}$ and $\Lambda^{-1/5}$, computed for $1.4\ M_{\odot}$ static stars described by the same EOS. We observe that the data points scatter in a very similar manner in all the panels[4]. In particular, EOSs which lie above the respective fit in one of the panels, typically lie above the corresponding fit in the rest of the panels as well. Similarly, EOSs below the empirical relation in one panel tend to be below the respective fit in the other panels too. Notably, the data points distribute in a systematic way with respect to all three empirical relations. Moreover, the very similar point scatter with respect to the $f_{\mathrm{peak}}(R)$ and $f_{\mathrm{peak}}(R^{90\%})$ empirical relations supports that the deviations are sensitive to the high-density regime within the star.

We now examine how the points scatter in plots referring to binary systems (i.e. f_{peak}) compared to the point distribution from isolated NSs (i.e. f_{pert}). We present such a comparison in Fig. 6.6, focusing on $1.35 + 1.35\ M_{\odot}$ systems. We start by comparing the panels on the left. In the upper left panel, the dominant post-merger frequency f_{peak} is plotted as a function of the radius of $R_{1.6}$, namely the radius of $1.6\ M_{\odot}$ static stars. In the middle left panel, we present the perturbative $f-$mode frequency f_{pert}, computed for $1.6\ M_{\odot}$ isolated stars, versus the same independent variable, i.e. $R_{1.6}$. We emphasize that the independent variable is the same in both panels, while the frequencies refer to binaries and isolated stars in the upper and middle panel, respectively.

We compare how points distribute with respect to the corresponding fit in these two panels. EOSs which lie on the same side of the empirical relation in both panels are shown as black symbols. These points exhibit the same behavior in both plots, even though the frequencies refer to two very different systems. Data points which lie on opposite sides of the fit in these two panels do not follow the same systematic behavior. However, identifying all such points as outliers would be rather strict. In particular, points which are quite close to the respective fit in both panels cannot safely be classified as outliers, even if they are found on different sides of the fit. Performing the same analysis with a different set of EOSs or employing a different functional form for the fit would result in a different fit and possibly change whether a point is found above or below the fit. Points rather close to the fit are most prone to such a change in the character of the deviation. Hence, we identify actual outliers based on a refined criterion.

We consider green shaded bands around frequency fits in Fig. 6.6. The bands have a total width of 30 Hz, namely they extend 15 Hz towards both sides of the fits. If an EOS lies within the band in both panels, it is shown with a black marker and is not

---

[4] We highlight that each data point refers to a different EOS. Namely, the calculation for each EOS results in specific values for f_{peak}, R, $R^{90\%}$ and $\Lambda^{-1/5}$, which we then plot. Hence, in the text we shall employ the term "EOS" to refer to the actual data point corresponding to the calculation with the respective EOS.

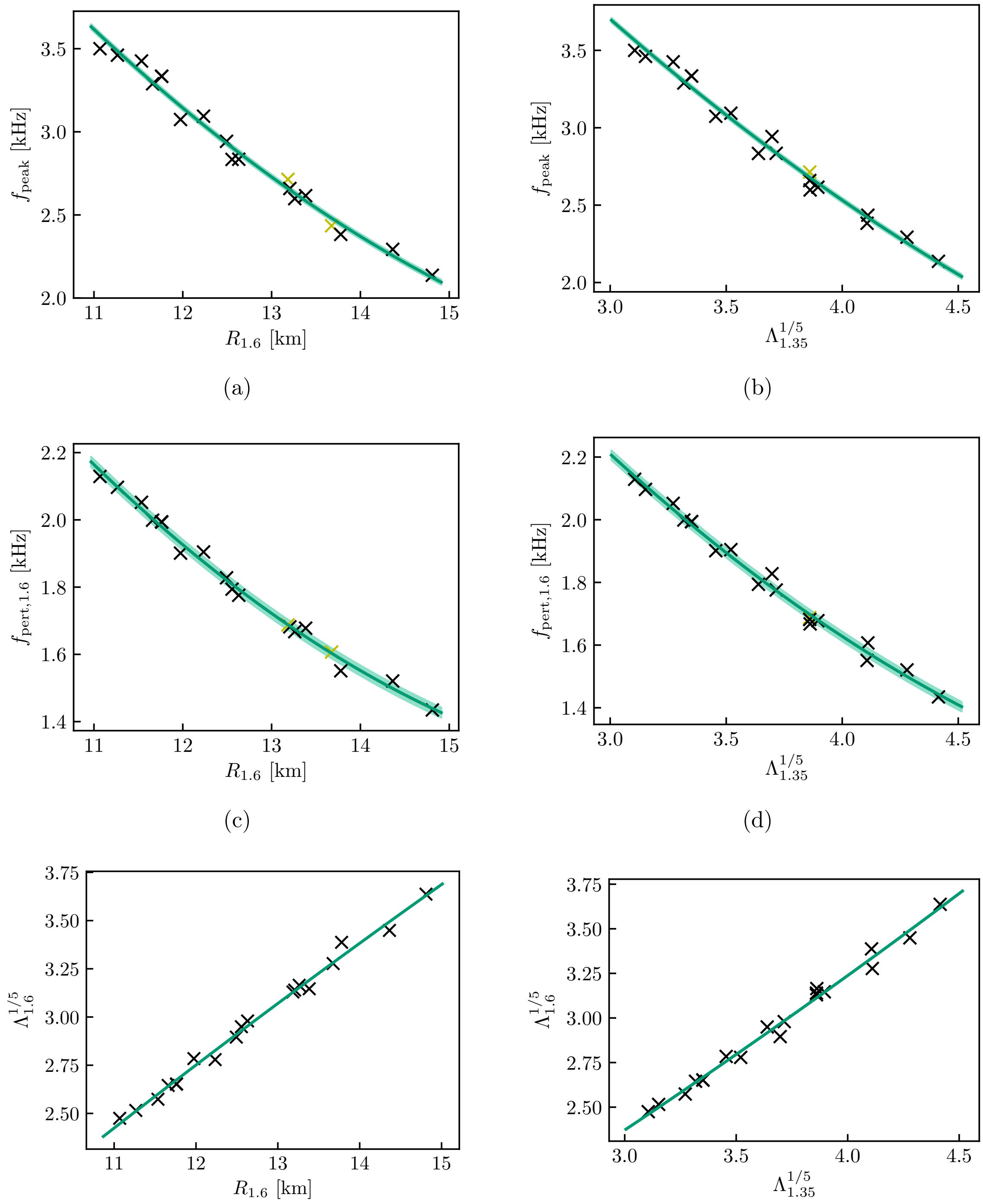

(a) (b)

(c) (d)

(e) (f)

Figure 6.6: In the various panels f_{peak} refers to post-merger frequencies for $1.35 + 1.35\ M_\odot$ binary systems, $f_{\mathrm{pert},1.6}$ are the perturbative frequencies for $1.6\ M_\odot$ stars, $R_{1.6}$ are the radii of static $1.6\ M_\odot$ stars, while $\Lambda_{1.35}^{1/5}$ and $\Lambda_{1.6}^{1/5}$ correspond to the fifth-root of the tidal deformabilities of $1.35\ M_\odot$ and $1.6\ M_\odot$ stars, respectively. Panels (a) and (c) display f_{peak} and $f_{\mathrm{pert},1.6}$, respectively, versus the same independent variable $R_{1.6}$. Panels (b) and (d) show f_{peak} and $f_{\mathrm{pert},1.6}$, respectively, as a function of $\Lambda_{1.35}^{1/5}$ in both plots. Panels (e) and (f) present $\Lambda_{1.6}^{1/5}$ as a function of $R_{1.6}$ and $\Lambda_{1.35}^{1/5}$, respectively. In all plots, a second-order fit to the data is shown as a solid curve. In frequency plots, we include a band with a total width of 30 Hz around each fit. The symbols' colors are explained in the main text. Adapted from [197].

classified as an outlier regardless of how it deviates from the two fits. If an EOS lies outside the band in at least one of the two panels and it also deviates in an opposite way in the two plots, we consider it an outlier and mark it with a yellow symbol. We note that including such a band is justified. The mean deviation for the $f_{\text{peak}}(R_{1.6})$ relation is 48 Hz (see Table 6.3). Hence, most points in the f_{peak} versus $R_{1.6}$ plot lie outside the green shaded band and are not captured by this criterion. In particular, only 4 out of 19 points lie within the band in the upper left panel of Fig. 6.6.

Remarkably, even though we compare two very different systems, most EOSs deviate in the same systematic way in the $f_{\text{pert}} - R$ and $f_{\text{peak}} - R$ relations displayed in Fig. 6.6. In particular, 17 out of 19 EOSs scatter in the same way when considering the classification that we introduced. We also note that, based on the discussion of Fig. 6.10 in Section 6.3.2, in reality all data points follow the same systematic trend in the way that they deviate.

Table 6.4: The fourth column indicates the number of outliers found when comparing frequency deviations between the pairs of relations listed in columns two and three. Outliers are defined as data points which lie on opposite sides of the respective fits and outside a 30 Hz band around each fit. The values of f_{peak} in each relation refer to the binary system shown in the first column. Table adapted from [197].

Binary masses $[M_\odot]$	Relation 1	Relation 2	Number of outliers
$1.2 + 1.2$	$f_{\text{pert},1.4}(R_{1.4})$	$f_{\text{peak}}(R_{1.4})$	1/16
$1.2 + 1.2$	$f_{\text{pert},1.4}(\Lambda_{1.2}^{1/5})$	$f_{\text{peak}}(\Lambda_{1.2}^{1/5})$	0/16
$1.2 + 1.2$	$f_{\text{pert},1.4}(R_{1.2})$	$f_{\text{peak}}(R_{1.2})$	1/16
$1.2 + 1.2$	$f_{\text{peak}}(\Lambda_{1.2}^{1/5})$	$f_{\text{peak}}(R_{1.2})$	1/16
$1.2 + 1.2$	$f_{\text{peak}}(R_{1.4})$	$f_{\text{peak}}(R_{1.2})$	1/16
$1.35 + 1.35$	$f_{\text{pert},1.6}(R_{1.6})$	$f_{\text{peak}}(R_{1.6})$	2/19
$1.35 + 1.35$	$f_{\text{pert},1.6}(\Lambda_{1.35}^{1/5})$	$f_{\text{peak}}(\Lambda_{1.35}^{1/5})$	1/19
$1.35 + 1.35$	$f_{\text{pert},1.6}(R_{1.35})$	$f_{\text{peak}}(R_{1.35})$	2/19
$1.35 + 1.35$	$f_{\text{peak}}(\Lambda_{1.35}^{1/5})$	$f_{\text{peak}}(R_{1.35})$	1/19
$1.35 + 1.35$	$f_{\text{peak}}(R_{1.6})$	$f_{\text{peak}}(R_{1.35})$	1/19
$1.4 + 1.4$	$f_{\text{pert},1.7}(R_{1.7})$	$f_{\text{peak}}(R_{1.7})$	3/16
$1.4 + 1.4$	$f_{\text{pert},1.7}(\Lambda_{1.4}^{1/5})$	$f_{\text{peak}}(\Lambda_{1.4}^{1/5})$	2/16
$1.4 + 1.4$	$f_{\text{pert},1.7}(R_{1.4})$	$f_{\text{peak}}(R_{1.4})$	2/16
$1.4 + 1.4$	$f_{\text{peak}}(\Lambda_{1.4}^{1/5})$	$f_{\text{peak}}(R_{1.4})$	1/16
$1.4 + 1.4$	$f_{\text{peak}}(R_{1.7})$	$f_{\text{peak}}(R_{1.4})$	2/16
$1.5 + 1.5$	$f_{\text{pert},1.75}(R_{1.75})$	$f_{\text{peak}}(R_{1.75})$	1/6
$1.5 + 1.5$	$f_{\text{pert},1.75}(\Lambda_{1.5}^{1/5})$	$f_{\text{peak}}(\Lambda_{1.5}^{1/5})$	0/6
$1.5 + 1.5$	$f_{\text{pert},1.75}(R_{1.5})$	$f_{\text{peak}}(R_{1.5})$	0/6
$1.5 + 1.5$	$f_{\text{peak}}(\Lambda_{1.5}^{1/5})$	$f_{\text{peak}}(R_{1.5})$	0/6
$1.5 + 1.5$	$f_{\text{peak}}(R_{1.75})$	$f_{\text{peak}}(R_{1.5})$	2/6

We now consider the top and middle right panels in Fig. 6.6. In the top right panel we plot f_{peak} for $1.35 + 1.35\ M_\odot$ binary systems versus $\Lambda_{1.35}^{1/5}$, namely the fifth-root of the tidal deformability corresponding to the inspiraling stars. In the middle right panel we show f_{pert} for 1.6 $M_{\odot}$ stars as a function of $\Lambda_{1.35}^{1/5}$. Based on our classification criterion, we can identify only a single outlier data point. That is, 18 out of 19 EOSs distribute in the same way with respect to the corresponding fits. Moreover, we note that the points distribute quite similarly in all four plots in the top and middle rows in Fig. 6.6.

We perform the same analysis for other binary systems and pairs of relations and consistently find similar results. Table 6.4 lists our findings. Notably, for all the binary systems considered here, we can identify many pairs of relations, where most EOSs deviate in the same way with respect to the corresponding fits. Many pairs of relations included in Table 6.4 compare frequency deviations between post-merger frequencies and perturbative calculations. The very low number of outliers across all such pairs, binary masses and independent variables corroborates our observation that, even though binary system remnants and isolated stars are very different systems, the data points distribute in a very similar way when comparing frequency plots for these systems (see also Fig. 6.10).

We find that the agreement is even more pronounced in plots where the data points exhibit overall larger mean deviations. In such plots the data points lie further away from the respective fit and frequency deviations are more pronounced. Hence, it is more straightforward to classify points as exhibiting the same behavior or being outliers. In addition, in such cases data points are less sensitive to changes in the fit. This further supports that the way in which individual points scatter with respect to the respective fit, which depicts some kind of average behavior, is systematic and determined by the EOS. An example of such plots are relations where the independent variable (R or $\Lambda^{1/5}$) corresponds to stars with the same mass as the inspiraling stars.

We note that one can identify a quite similar data point distribution in plots such as Fig. 6.6. Broadly speaking, the points form very similar clusters and the scatter shows some general pattern. This is quite interesting given that merger simulations are quite complex calculations, significantly more complicated than perturbative calculations.

We expect that the results will not be significantly affected by including more EOSs. The fit is constructed based on a large number of EOSs, which cover a broad range in the $M-R$ diagram, even parts which are excluded based on observations. Hence, considering additional EOSs should not affect the fit significantly and, subsequently, frequency deviations should remain largely unaffected.

It is important to stress out that the agreement in frequency deviations from the respective fit when comparing merger simulations and perturbative calculations is rather unexpected. Perturbative frequencies f_{pert} refer to static, cold and non-rotating stars. Binary remnants are rapidly rotating, reach high temperatures and have significantly higher masses. Moreover, in the early post-merger phase, when f_{peak} is extracted, the remnant is still dynamically evolving. Hence, the striking similarity of frequency deviations in these two systems strongly suggests that an underlying mechanism is responsible for shifting each frequency in a particular direction. Since the EOS is the only common component in both systems, frequency deviations very likely contain additional information about the EOS. We further examine this point in Section 6.3.2.

In principle, the frequency deviations may be observable. The fit is constructed based on numerical simulations. Thus, highly accurate simulations are required. Measuring the frequency and corresponding stellar property and comparing to the theoretical fit informs us about how the frequency deviates. Observations of BNS mergers can provide us with the frequency f_{peak}, as well as the radius R and the tidal deformability Λ. Alternatively, R or Λ can be measured independently from a different merger or type of event. We note that frequency deviations can potentially correlate with other features of the GW signal from a merger event. Secondary features of the GW signal apparently deviate in a similar way as the dominant peak (see Fig. 6 in [49]).

Naturally, applying these ideas requires high precision measurements. Both in terms of high accuracy observations, as well as in terms of the numerical modelling of the system. This serves as additional motivation to further develop new numerical approaches, such as the moving-mesh approach extensively discussed in this thesis.

We also comment on the accuracy of the employed numerical results, as well as the sensitivity of frequency deviations to numerical aspects of the modelling. We already pointed out that the 3D numerical simulations of binary systems are significantly more complex than linear perturbation calculations. Perturbative frequencies can be computed with a very high resolution, which ensures that the results have converged and are robust. Hence, it is rather promising that 3D hydrodynamical simulations with the employed resolution can resolve frequencies accurately enough to capture the underlying physics behind frequency deviations. This does not necessarily imply that systematic uncertainties of the numerical modelling and frequencies are resolved at the level of (a few) 10 Hz, namely the magnitude of frequency deviations. Numerical artifacts can in principle even be the reason which leads to the identified outliers[5]. However, the overall agreement in the behavior of data points in frequency plots for these two very different systems and numerical approaches is quite encouraging.

In addition, we examine the robustness of frequency deviations in binary systems with respect to numerical details of the modelling. In particular, we perform additional simulations for $1.35+1.35\ M_{\odot}$ systems employing the DD2F and SFHX EOSs. These two EOSs yield comparable values for $R_{1.6}$ of roughly 12 km, while they result in opposite frequency deviations. DD2F lies above the respective fit, while SFHX yields a smaller f_{peak} than the one computed from the fit. Initially, we evaluate the effect of the inspiral on our results. We simulate the systems starting from a larger initial separation (4 and 5 orbits before merging respectively) and find that the character of the deviations remains unaffected.

Furthermore, we perform different resolution simulations for DD2F to assess the effect of resolution. We employ roughly 100,000 and 600,000 SPH particles, namely lower and higher resolutions compared to our default choice of 300,000 particles. We find that the extracted value for f_{peak} exhibits statistical fluctuation of the order of a few 10 Hz. However, the differences in the frequencies are smaller that frequency deviations and the data points from different resolutions always lie on the same side of the fit (constructed from our standard resolution binary data set). Neither the number of orbits before merging nor resolution changes frequencies in a systematic way, which supports that frequency deviations are actually caused by the underlying EOS and not aspects of the numerical modelling.

As an additional, rather demanding test, we also simulate $1.37+1.37\ M_{\odot}$ binary systems employing the same set of EOSs as for $1.35+1.35\ M_{\odot}$ binaries (see Table 6.1). In these simulations we employ the C^6 Wendland kernel function [89, 310], instead of the spherically symmetric spline kernel which is our standard choice. We construct the

---

[5] We note however that outliers behave also in a very consistent way (see Fig. 6.10 and relevant discussion)

respective empirical relation and examine frequency deviations for these calculations. Notably, the individual data points distribute in the exact same way with respect to the fit as for $1.35 + 1.35\ M_\odot$ systems. The fact that the character of frequency deviations remains unaffected by the slightly increased binary mass and the different SPH kernel function highlights that our observation is robust against certain aspects of the numerical modelling.

Overall, we find that the exact details of the numerical treatment do affect the absolute values of the frequencies up to some extent. But the pattern of frequency deviations seems to be rather robust. The fact that we employ the same setup in all our binary simulations also suggests that our results are affected only by statistical fluctuations, which seemingly are smaller than the typical magnitude of frequency deviations.

Finally, we briefly consider unequal-mass systems. We simulate binaries with a total mass of $2.7\ M_\odot$ and mass ratios of $q = 0.95$ and $q = 0.9$ for DD2F and SFHX. The extracted frequencies are quite similar to the ones from equal-mass systems. In particular, the differences in the frequencies between equal-mass systems and systems with $q = 0.95$ and $q = 0.9$ are of the order of a few 10 Hz and they also seem to be dominated by statistical fluctuations. We thus expect that for a relatively small range of q, namely systems with relatively small mass asymmetry, the underlying physics leading to frequency deviations is more prevalent than the effects of the mass ratio.

6.3.2. Encoded equation of state information

In Section 6.3.1 we examine how data points deviate from the respective fit in frequency versus R or $\Lambda^{1/5}$ plots for two very different systems. In particular, we uncover a striking similarity between frequency deviations referring to BNS merger remnants and isolated NSs. This observation indicates that frequency deviations should carry additional information about the EOS, considering that the position of the data points in such plots is determined by the EOS. In this section we explore this direction focusing on perturbative frequencies, which are arguably more robust and accurate. This allows to reliably examine the position of individual points in frequency plots. We then extend the discussion to frequency deviations in binary systems, which is rather straightforward because deviations defined based on $f_{\mathrm{pert}}(R_x)$ and $f_{\mathrm{peak}}(R_x)$ relations are very similar, as shown in Section 6.3.1.

In Section 6.2.1 we show that, considering isolated stars with masses in the range $1.1 - 1.9\ M_\odot$, the relation $Mf_{\mathrm{pert}}(\Lambda^{-1/5})$ is extremely tight (see also Fig. 6.3 and Table 6.2). Naturally, focusing on a single static star mass, also results in very accurate relations between f_{pert} and $\Lambda^{-1/5}$. We present such a relation in Fig. 6.7 for $1.6\ M_\odot$ stars and find a maximum deviation of only 2.2 Hz (see Table 6.5). Other values for the fixed mass result in similarly, highly accurate relations. As a result, for any given stellar model, f_{pert} and $\Lambda^{-1/5}$ are practically equivalent.

Notably, relations between f_{pert} and the radius computed for the same mass are not as tight (see Table 6.2). Indeed, we notice that the points exhibit some sizable scatter in Fig. 6.6c, contrary to Fig. 6.7 which features practically no scatter[6]. Hence, focusing on $\Lambda^{1/5} - R$ relations should help determine which EOS properties cause the

---

[6] Note that in Fig. 6.6d f_{pert} and $\Lambda^{1/5}$ refer to isolated star with different masses, which is the reason behind the scatter.

Table 6.5: Fixed-mass relations presented in different plots. The first column lists the plot where the relation is shown. The second column lists the relations. The third and fourth columns present the mean and maximum deviations for each of the relations. The $f-$mode frequencies $f_{\rm pert}$ are in kHz, radii are in km and tidal deformabilities are dimensionless. The number in the subscript of each variable denotes the mass of the isolated star to which it refers. Table adapted from [197].

Position	Fit	Mean dev. [Hz]	Max dev. [Hz]
Fig. (6.6c)	$f_{pert,1.6} = 7.04 - 0.631R_{1.6} + 1.708 \times 10^{-2}R_{1.6}^2$	15	36
Fig. (6.6d)	$f_{pert,1.6} = 5.11 - 1.255\Lambda_{1.35}^{1/5} + 9.618 \times 10^{-2}\Lambda_{1.35}^{2/5}$	17	45
Fig. (6.7)	$f_{pert,1.6} = 4.988 - 1.539\Lambda_{1.6}^{1/5} + 1.546 \times 10^{-1}\Lambda_{1.6}^{2/5}$	1	2.2
Fig. (6.6f)	$\Lambda_{1.6}^{1/5} = 0.205 + 0.614\Lambda_{1.35}^{1/5} + 0.036\Lambda_{1.35}^{2/5}$	0.073	0.029

frequency deviations[7].

Focusing on a fixed mass, we can employ $f_{\rm pert}$ and $\Lambda^{1/5}$ interchangeably. This suggests that frequency deviations defined based on $f_{\rm pert,x}(R_x)$ relations for a given fiducial mass x, are tightly anti-correlated with deviations defined based on $\Lambda_x^{1/5}(R_x)$ relations (e.g. compare panels panel (c) and (e) in Fig. 6.6). In Fig. 6.8 we illustrate that this is the case for stars with mass $x = 1.6\ M_\odot$. Frequency deviations, which we denote as $\delta_R f_{\rm pert}$, are defined between the data points and the respective second-order fit in panel (c) of Fig. 6.6. Similarly, we define deviations $\delta_R\Lambda^{1/5}$ between data points and the second-order fit in panel (e) of Fig. 6.6. Evidently, the two types of deviations are indeed strongly anti-correlated and the point distribution in Fig. 6.8 follows a linear trend. We note that we verify that this behavior is independent of the chosen fiducial mass by examining plots like Fig. 6.8 for all the static star masses that we consider here, i.e. fixed masses in the interval $[1.1, 1.9]\ M_\odot$.

Evidently, frequency deviations $\delta_R f_{\rm pert}$, and ultimately $\delta_R f_{\rm peak}$, for a fixed mass relate to deviations in $\Lambda^{1/5}(R)$ relations. As a reminder, the tidal deformability is defined as $\Lambda = \frac{2}{3}k_2(\frac{c^2R}{GM})^5$. This suggests that frequency deviations can be linked to the tidal Love number k_2. Notably, k_2 correlates roughly with the inverse compactness R/M. For example, in [88] they find $\Lambda \simeq \alpha(\frac{c^2R}{GM})^6$ with $\alpha = 0.0093 \pm 0.0007$. Based on the definition of tidal deformability, this relation implies an average $k_2^{\rm av} = \frac{3}{2}\alpha(\frac{c^2R}{GM})$. Deviations between k_2 and $k_2^{\rm av}$ determine the scatter in $\Lambda^{1/5} - R$ plots and, subsequently, frequency deviations in $f_{\rm pert}(R)$ and $f_{\rm peak}(R)$ relations. We note that k_2 can be accurately computed for each EOS, while $k_2^{\rm av}$ indicates some average behavior based on the inverse compactness. We conclude that constraining frequency deviations based on observations is informative about k_2 and can be used to break the degeneracy between Λ, k_2 and R.

In Fig. 6.9, we apply our reasoning to 1.6 $M_\odot$ static models. In the upper panel we show k_2 as a function of R/M. The green solid line is a second-order fit to the data.

---

[7] We note that the tidal deformability is less sensitive than the radius to the low-density regime. In Section 6.2.1, we introduce two different radii, $R^{90\%}$ and $R^{\rm cc}$, based on the sphere containing 90% of the mass of the stellar model and the crust-core transition density, respectively. They are thus sensitive to the high-density parts of the star. By examining relations involving these two radii, we find that they still exhibit sizable scatter, which shows that frequency deviations encode information about the high-density EOS.

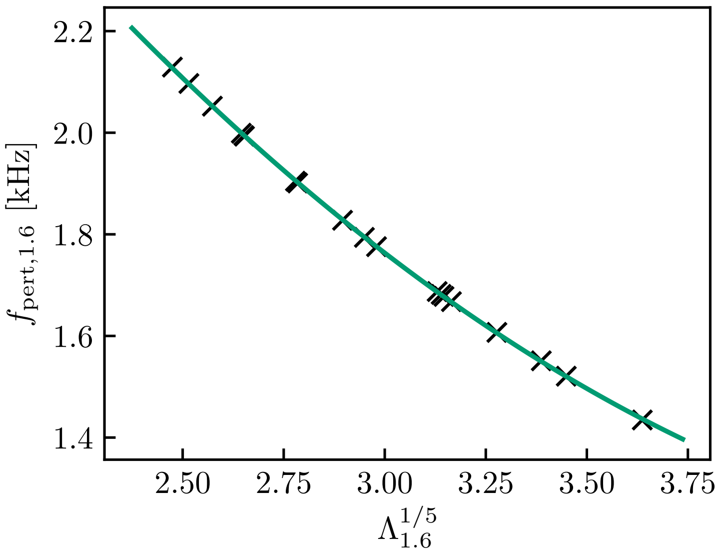

Figure 6.7: $f-$mode frequency as a function of $\Lambda_{1.6}^{1/5}$ for isolated 1.6 $M_\odot$ stars. The solid line displays a second-order fit to the data, which exhibits a maximum deviation of 2.2 Hz. Adapted from [197].

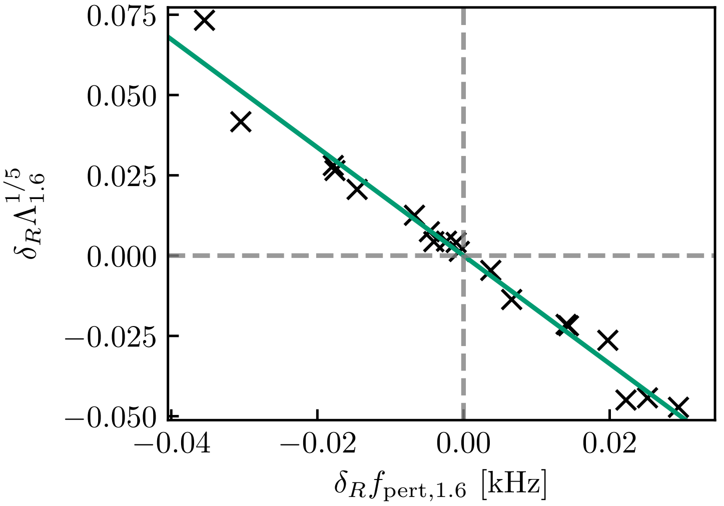

Figure 6.8: Deviations of data points and a second-order $\Lambda_{1.6}^{1/5}(R_{1.6})$ relation (denoted as $\delta_R \Lambda^{1/5}$) as a function of frequency deviations in a second-order $f_{\mathrm{pert}}(R_{1.6})$ empirical relation (denoted as $\delta_R f_{\mathrm{pert},1.6}$). We refer to panels (e) and (c) of Fig. 6.6 for the two deviations, respectively. A first-order fit to the data is shown (solid line). Figure is adapted from [197].

Data points, namely calculations for different EOSs, approximately follow the fit with some sizable point-to-point scatter around it. We display the maximum deviation from the fit with the gray shaded area.

We argued that the deviations in the upper panel of Fig. 6.9 are directly related to frequency deviations $\delta_R f_{\mathrm{pert}}$ referring to 1.6 $M_\odot$ stars. Based on this argument, we apply a correction to k_2 based on the frequency deviations defined for isolated stars. In particular, the "corrected" k_2 reads $k_2 - b\ \delta_R f_{\mathrm{pert,1.6}}$, where we determine $b = -0.2206$ kHz^{-1} based on a single fit to the deviations of the data points from the fit in the upper panel in Fig. 6.9. We plot $k_2 - b\ \delta_R f_{\mathrm{pert,1.6}}$ as a function of R/M in the middle panel of Fig. 6.9. The solid line is the same second-order fit presented in the upper panel, while the gray shaded area again depicts the maximum deviation from the fit. Taking frequency deviations into account results in a very tight correlation between the "corrected" $k_2 - b\ \delta_R f_{\mathrm{pert,1.6}}$ and R/M, which validates our argument that frequency deviations are directly related to deviations of k_2 from some average estimate for its value based on a large EOS sample. We explicitly present the analysis for 1.6 $M_\odot$ stars, but we find similar behavior for other masses in the range $1.1 - 1.9\ M_\odot$. We also note that, alternatively, one can include the correction in the independent variable R/M and determine k_2 based on the value of $R/M - b'\ \delta_R f_{\mathrm{pert}}$ with high accuracy[8].

We extend the discussion to frequency deviations $\delta_R f_{\mathrm{peak}}$, defined as the deviation of data points from the respective fit in post-merger frequencies versus radii plots. In Fig. 6.10, we plot $\delta_R f_{\mathrm{peak}}$ defined in panel (a) of Fig. 6.6 as a function of $\delta_R f_{\mathrm{pert,1.6}}$. The green shaded box has a side length of 30 Hz and corresponds to the green shaded bands that we introduce in frequency plots in Fig. 6.6 to identify outliers. We also present a first-order fit to the data as a solid line. We refer to the fit as $\delta_R f|_{\mathrm{fit}}$ (see caption of Fig. 6.10 for the exact expression).

In the bottom panel of Fig. 6.9, we employ the fit $\delta_R f|_{\mathrm{fit}}$ to compute a "corrected" value for k_2 based on frequency deviations from binary systems. The solid line matches the second-order fit shown in the upper panel of Fig. 6.9, the gray shaded area indicates the maximum deviation from the fit, while b has the same value as in the middle panel. Evidently, including the correction term $b\ \delta_R f|_{\mathrm{fit}}(\delta_R f_{\mathrm{peak}})$ reduces the scatter of data points around the second-order fit. We find a decrease of 33% and 36% in the average and maximum deviation from the fit, respectively. The improvement is even more pronounced for EOSs which yield $R/M < 5.5$. Moreover, the maximum deviation is practically determined by a single data point with $R/M \simeq 5.83$, which arguably deviates considerably more compared to any other data point. We consider also deviations defined on f_{peak} versus radius plots, where the radii are computed for different choices of the static mass. We find that they also decrease the scatter when included as corrections in k_2. Notably, considering deviations in relations of f_{peak} for $1.35 + 1.35\ M_\odot$ binary systems and radii $R_{1.35}$ of 1.35 $M_\odot$ stars leads to even better results than those shown in the bottom panel of Fig. 6.9. We remark that, in principle, the analysis of the inspiral can potentially provide an estimate for $R_{1.35}$.

Directly measuring frequency deviations $\delta_R f_{\mathrm{peak}}$ can be a challenge. However, determining the sign of $\delta_R f_{\mathrm{pert}}$ provides already important information. The sign indicates whether the respective data point is located above or below the corresponding $k_2(R/M)$ relation. Hence, the error in computing k_2 from the corresponding fit is

---

[8] Note that b' is determined by fitting $\delta_R f_{\mathrm{pert,1.6}}$ to the horizontal deviations between the data points and the fit in the upper panel of Fig. 6.9. Subsequently, $b' \neq b$.

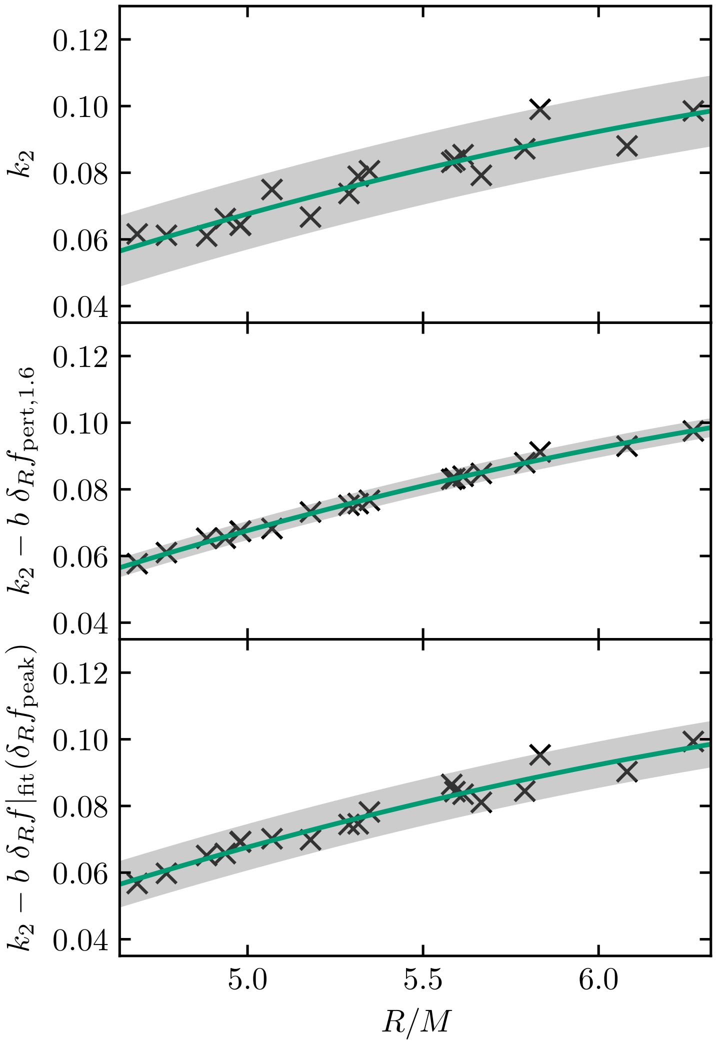

Figure 6.9: The upper panel displays the tidal Love number k_2 versus the inverse compactness R/M for 1.6 $M_\odot$ static stars. In the middle panel we "correct" k_2 based on the frequency deviations $\delta_R f_{\mathrm{pert},1.6}$ defined in panel (c) of Fig. 6.6. In the bottom panel k_2 is corrected based on $\delta_R f_{\mathrm{peak}}$ and the first-order fit shown in Fig. 6.10. The value of b in the middle and bottom panels is $-0.2206\ \mathrm{kHz}^{-1}$. The maximum deviation in each panel is displayed with a gray shaded band. The solid curve is the same in all panels and represents a second-order fit to $k_2(R/M)$. The figure is adapted from [197].

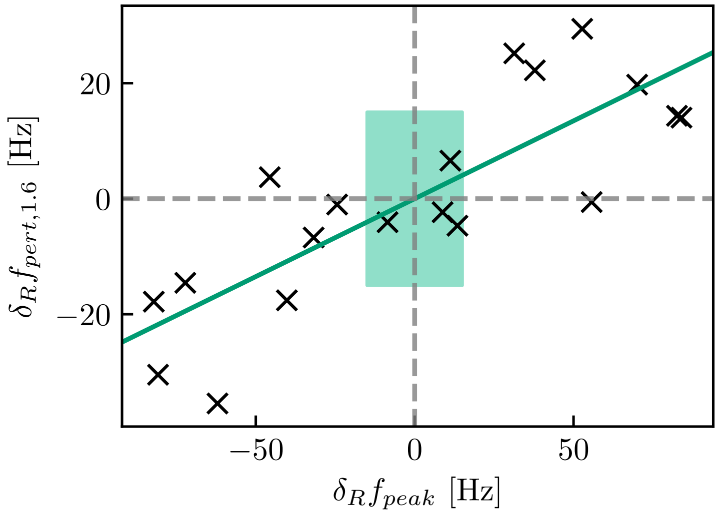

Figure 6.10: Frequency deviations between data points and second-order fits to the data in panels (a) and (c) of Fig. 6.6, respectively. The green-shaded box represents the bands shown in frequency plots in Fig. 6.6 and has a side length of 30 Hz. The solid green lines depicts a first-order fit to the data and reads $\delta_R f_{\mathrm{pert},1.6} = 0.2697\ \delta_R f_{\mathrm{peak}}$. Adapted from [197].

reduced by half. We also note that simulated injections support that the post-merger frequencies can be extracted with an accuracy of $\sim$ 10 Hz with future ground-based detectors, provided a sufficient signal-to-noise ratio (SNR) [73, 75]. This highlights that inferring frequency deviations largely depends on constructing accurate empirical relations between frequencies and properties of static stars to which we can compare measured frequencies. The main work in this thesis, namely extending the moving-mesh code AREPO to simulate general relativistic systems on dynamical spacetimes, is in this direction.

Overall, our analysis shows that frequency deviations $\delta_R f_{\mathrm{pert}}$ and $\delta_R f_{\mathrm{peak}}$ can be employed to improve the accuracy in determining k_2. This can lead to stricter EOS constraints, considering that Λ and R can potentially be extracted from the analysis of the inspiral. Moreover, Fig. 6.10 clearly shows that, when comparing $\delta_R f_{\mathrm{pert}}$ and $\delta_R f_{\mathrm{peak}}$, all data points follow a systematic trend, including the two outliers (see also Fig. 6.6 and Table 6.4). This suggests that our criterion to identify outliers might be too strict and possibly prone to numerical artifacts in simulations of binary systems. This further supports our observation that frequency deviations referring to the $f-$mode in isolated stars and the dominant post-merger oscillation in merger remnants is robust.

6.3.3. Relation to tidal deformability of high-mass neutron stars

In Section 6.3.2 we discuss extensively deviations on frequency versus radius plots and connect them to the tidal Love number k_2. We now examine deviations in frequency versus tidal deformability plots.

As discussed in Section 6.3.2, the perturbative $f-$mode frequency is practically equivalent to $\Lambda^{1/5}$ for stellar models with a fixed mass (see Fig. 6.7 for 1.6 $M_\odot$ configurations). Hence, $f_{\mathrm{pert}} - \Lambda^{1/5}$ plots, where f_{pert} and $\Lambda^{1/5}$ are computed for two different masses, practically show the relation between $\Lambda^{1/5}$ at these two masses. For example, in Fig. 6.6d we plot $f_{\mathrm{pert},1.6}$ referring to 1.6 $M_\odot$ models versus $\Lambda^{1/5}_{1.35}$ corresponding to 1.35 $M_\odot$ configurations. Thus, Fig. 6.6d essentially shows the relation between $\Lambda^{1/5}_{1.6}$ and $\Lambda^{1/5}_{1.35}$, i.e. $\Lambda^{1/5}$ at two different masses. The difference between values of $\Lambda^{1/5}$ computed at two different masses approximates its derivative with respect to the mass.

In the upper panel of Fig. 6.11, we plot the derivative $d\Lambda^{1/5}/dM$ computed at $M = 1.35\ M_\odot$ as a function of $\Lambda^{1/5}_{1.35}$. The green solid line is a second-order fit to the data, while the gray shaded area depicts the maximum deviation from the fit. The data points roughly follow the fit, but they exhibit some sizable scatter. This is expected, because different EOSs admit different derivatives at 1.35 $M_\odot$, even for similar values of $\Lambda^{1/5}_{1.35}$.

Clearly, the value of the tidal deformability at higher masses contains information about the slope of $\Lambda(M)$. Hence, we expect that the frequency deviations defined in plots like Fig. 6.6d (or frequency deviations which correlate with them such as $\delta_{\Lambda^{1/5}_{1.35}} f_{\mathrm{peak}}$) can be used to reduce the scatter in the upper panel of Fig. 6.11. We explicitly show this in the middle and lower panels of Fig. 6.11, where we "correct" the derivative $d\Lambda^{1/5}/dM$ through frequency deviations following an analogous procedure as in Fig. 6.9. In the middle panel we employ $\delta_{\Lambda^{1/5}_{1.35}} f_{\mathrm{pert},1.6}$, while in the lower panel we use $\delta_{\Lambda^{1/5}_{1.35}} f_{\mathrm{peak}}$. In both panels we display the same second-order fit as in the upper panel. Gray shaded areas display the maximum deviation of data points from the fit. Evidently, the relations for the "corrected" derivatives become tighter. In particular, the maximum deviation is reduced by 80% in the middle panel, where we employ the accurate and robust perturbative frequencies.

Figure 6.11 practically shows that a single BNS observation, where we extract the tidal deformability based on the analysis of the inspiral and measure f_{peak} in the post-merger phase, in essence determines also the derivative of the tidal deformability with respect to the mass. As a result, measuring the frequency deviations can help us probe $\Lambda(M)$ at higher masses, without directly measuring Λ at higher masses.

In our analysis we employ deviations defined on a $f_{\mathrm{pert},1.6} - \Lambda^{1/5}_{1.35}$ plot, but our results are not restricted to a mass of 1.6 $M_\odot$. In principle, tighter relations for the derivative $d\Lambda^{1/5}/dM$ can be obtained by considering f_{pert} of any mass. Moreover, similar results hold for other binary masses. Finally, we remark that the arguments discussed here might be reversible. An estimate of the derivative $d\Lambda^{1/5}/dM$, e.g. from two distinct measurements of Λ at different masses, can potentially provide information on the frequency deviations leading to a more accurate prediction of f_{peak}.

6.4. Direct relations between gravitational wave frequencies of merger remnants and isolated neutron stars

As it is evident based on the previous discussion, perturbative $f-$mode frequencies f_{pert}, as well as dominant post-merger oscillation frequencies f_{peak}, correlate with stellar properties of isolated stars. This suggests that a direct relation between f_{pert} and f_{peak} should exist. Moreover, in Sections 6.3.1 and 6.3.2, we find that frequency

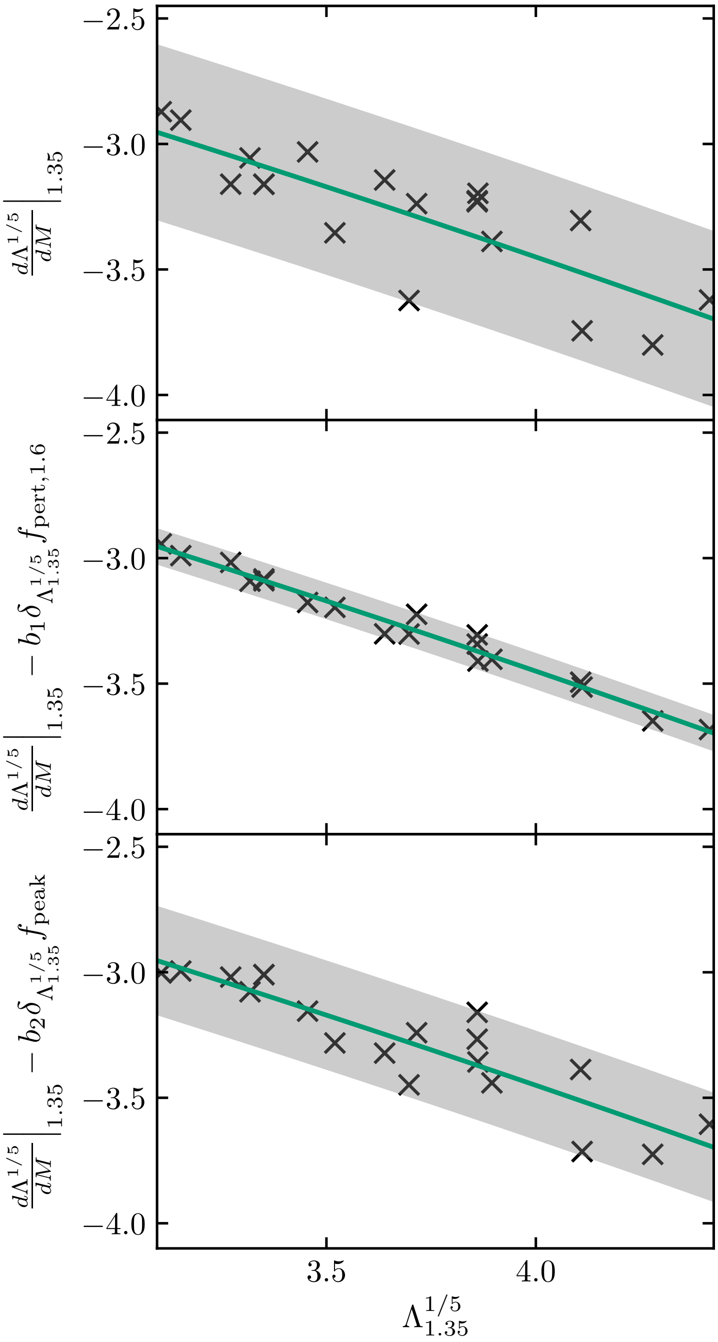

Figure 6.11: The upper panel displays the derivative $d\Lambda^{1/5}/dM$ at a fixed mass of 1.35 $M_\odot$ versus $\Lambda^{1/5}_{1.35}$. In the middle panel we "correct" the derivative based on the deviations $\delta_{\Lambda^{1/5}_{1.35}} f_{\mathrm{pert},1.6}$. In the bottom panel the derivative is corrected based on $\delta_{\Lambda^{1/5}_{1.35}} f_{\mathrm{peak}}$ defined in Fig. 6.6b. The solid line is identical in all panels and represents a second-order fit to the data in the upper panel. The maximum deviation in each panel is shown as a gray shaded band. The two fit parameters read $b_1 = -7.293$ kHz^{-1} and $b_2 = -2.029$ kHz^{-1}. Adapted from [197].

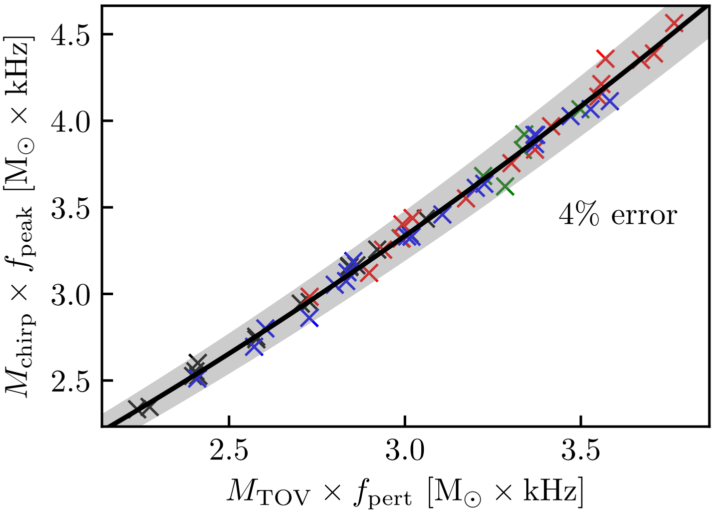

Figure 6.12: Mass-scaled dominant post-merger oscillation frequencies $M_{\rm chirp} f_{\rm peak}$ versus mass-scaled perturbative frequencies $M_{\rm TOV} f_{\rm pert}$ referring to stellar models with a mass $M_{\rm TOV}$. Here $M_{\rm TOV} = 1.23 \times M_{\rm tot}/2$, where $M_{\rm tot}$ is the total mass of the respective binary system. Black symbols denote $1.2 + 1.2\ M_\odot$, blue symbols $1.35 + 1.35\ M_\odot$, red markers $1.4 + 1.4\ M_\odot$ and green symbols $1.5 + 1.5\ M_\odot$ systems, respectively. The solid line displays a second-order fit to the data. The gray shaded area corresponds to the 4% error band and includes all the points. Figure adapted from [197].

deviations in plots involving $f_{\rm pert}$ are in agreement with deviations in the respective $f_{\rm peak}$ relations (see Table 6.4). The matching frequency deviations might, up to some extent, cancel each other out and result in rather accurate relations between $f_{\rm pert}$ and $f_{\rm peak}$.

Figure 6.12 displays the mass-scaled post-merger frequency $M_{\rm chirp} f_{\rm peak}$, for each one of the 57 binary systems considered here, as a function of the mass-scaled perturbative frequency $M_{\rm TOV} f_{\rm pert}$ referring to stellar configurations with a mass $M_{\rm TOV}$. Here $M_{\rm chirp}$ is the chirp mass[9], while we relate binary systems to static stars through $M_{\rm TOV} = 1.23 \times M_{\rm tot}/2$, where $M_{\rm tot}$ is the total mass of each binary. We determine the arithmetic value in the mapping between $M_{\rm TOV}$ and $M_{\rm tot}$ following a similar analysis to Appendix A. The values of $f_{\rm pert}$ (and $\Lambda^{1/5}$ in Fig. 6.13) for $M_{\rm TOV}$ models are computed based on a cubic spline fit to our perturbative data, which cover the range $[1.1, 1.9]\ M_\odot$ with a spacing of $0.05\ M_\odot$.

The solid line in Fig. 6.12 is a second-order fit to the data. Considering the scatter of data points around the fit, we find mean and maximum deviations of 30 Hz and 134 Hz, which shows that the relation is indeed very accurate. These deviations are only slightly higher compared to those reported in Table 6.3. Notably, the relations in Table 6.3 refer to fixed total binary masses, while the relation discussed here is mass-independent. The very tight correlation between $M_{\rm chirp} f_{\rm peak}(M_{\rm tot})$ and $M_{\rm TOV} f_{\rm pert}(M_{\rm TOV})$ further demonstrates the strong link between the dominant post-merger oscillation and the $f-$mode for the range of densities reached within the

---

[9] The chirp mass is defined as $M_{\rm chirp} = \frac{(M_1 M_2)^{3/5}}{(M_1+M_2)^{1/5}}$, where M_1 and M_2 are the masses of the two individual stars in the binary system. For equal-mass binaries the chirp mass is equivalent to the total mass.

Table 6.6: The third column provides mass-independent relations between the mass-scaled dominant post-merger oscillation frequency $M_{\rm chirp} f_{\rm peak}$ and stellar properties of isolated stars. The first column indicates if the relation is shown in a figure. The fourth and fifth columns list the average and maximum deviation for the corresponding relation, respectively. All frequencies are in kHz, masses have units of $M_\odot$, while the tidal deformability is dimensionless. The table is adapted from [197].

Fig.	Systems	Fit	Mean dev. [Hz]	Max dev. [Hz]
6.12	Equal-mass	$M_{\rm chirp} f_{\rm peak} = 0.299 + 0.595 M_{\rm TOV} f_{\rm pert} + 1.392 \times 10^{-1} \left(M_{\rm TOV} f_{\rm pert}\right)^2$	30	134
6.13	Equal-mass	$M_{\rm chirp} f_{\rm peak} = 11.846 - 4.464 \Lambda^{1/5} + 5.139 \times 10^{-1} \Lambda^{2/5}$	31	138
6.14	All	$M_{\rm chirp} f_{\rm peak} = 0.013 + 0.794 M_{\rm TOV} f_{\rm pert} + 1.042 \times 10^{-1} \left(M_{\rm TOV} f_{\rm pert}\right)^2$	35	150
-	All	$M_{\rm chirp} f_{\rm peak} = 11.536 - 4.261 \Lambda^{1/5} + 4.806 \times 10^{-1} \Lambda^{2/5}$	36	151

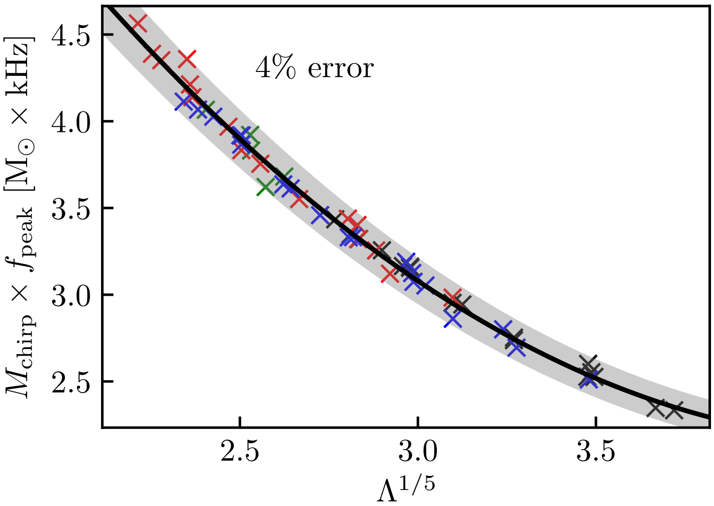

Figure 6.13: Mass-scaled dominant post-merger oscillation frequency $M_{\rm chirp} f_{\rm peak}$ as a function of the tidal deformability $\Lambda^{1/5}(M_{\rm TOV})$ of static stars. Symbol colors and $M_{\rm TOV}$ are the same as in Fig. 6.12. The solid line displays a second-order fit to the data. All data points lie within a 4% error band, shown as a gray shaded area around the fit. Adapted from [197].

remnant.

In Section 6.2.1 we discuss how the mass-scaled $f_{\rm pert}$ correlates remarkably tightly with $\Lambda^{-1/5}$ (see Fig. 6.3 and Table 6.2). Based on this discussion and Fig. 6.12, we expect that an accurate mass-independent relation between $M_{\rm chirp} f_{\rm peak}$ and $\Lambda^{-1/5}(M_{\rm TOV})$ should exist. Indeed, we find such a tight relation, which we present in Fig. 6.13 alongside a second-order fit to the data. We provide the fit expression and respective maximum and minimum deviation in Table 6.6. As expected, the deviations are in perfect agreement with those found for the $M_{\rm chirp} f_{\rm peak}(M_{\rm TOV} f_{\rm pert})$ relation. Furthermore, we remark that the average and maximum mass-scaled deviations in the $M_{\rm chirp} f_{\rm peak}(\Lambda^{-1/5}(M_{\rm TOV}))$ are 37 $\mathrm{M}_\odot \times$ Hz and 168 $\mathrm{M}_\odot \times$ Hz, respectively. Interestingly, they are considerably smaller than those reported for relation (4) in [59].

Up to now we have only considered equal-mass binary systems. We extend our analysis by considering also unequal-mass binaries and constructing relation of the same type which cover a broad range of mass ratios q. To this end, we directly import

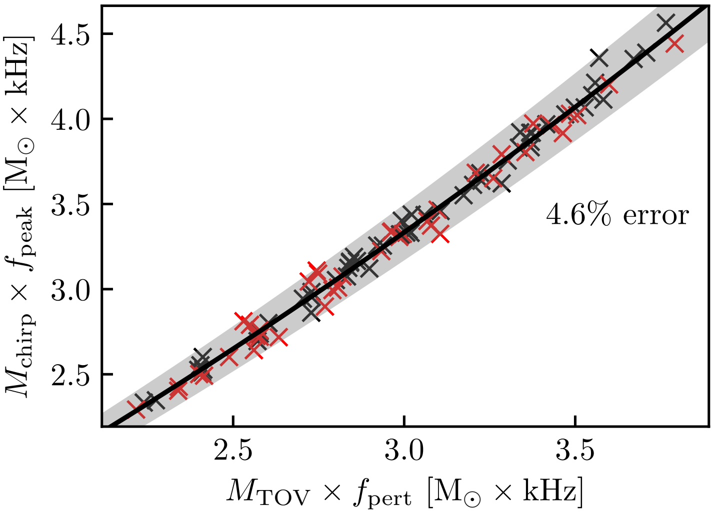

Figure 6.14: Same as Fig. 6.12, but black and red symbols correspond to equal-mass and unequal-mass systems, respectively. $M_{\rm TOV}$ is given by Eq. (6.1). The solid line displays a second-order fit to the data. The gray shaded array is a 4.6% error band. All points lie within the band. Figure adapted from [197].

the data referring to unequal-mass binary systems presented in Table II in [305] for all the EOSs listed in Section 6.1.3. The unequal-mass data set consists of an additional 40 binary systems. The lowest mass ratio is 0.67. To account for the variable mass ratio, we relate binary systems to static stars via

$$M_{\rm TOV} = \left[a + b \times (1-q)^2\right] \times \frac{M_{\rm tot}}{2}, \tag{6.1}$$

where $a = 1.23$ and $b = -0.67$. The value of a is such, that the relation reproduces the previous mapping between binary configurations and static stars at the equal-mass limit $q = 1$. We determine b based on a analysis similar to the one performed in Appendix A. Overall, we find that unequal-mass systems are better captured by static stars with a slightly smaller mass $M_{\rm TOV}$, compared to equal-mass binaries with the same total mass.

We present $M_{\rm chirp} f_{\rm peak}(M_{\rm tot})$ versus $M_{\rm TOV} f_{\rm pert}(M_{\rm TOV})$ for the combined data set of equal- and unequal-mass binary configurations in Fig. 6.14. The solid line is a second-order fit to the data. We find that including unequal-mass systems only marginally decreases the accuracy of the fit. Similarly to the case of equal-mass systems, a relation with $\Lambda^{1/5}(M_{\rm TOV})$ as the independent variable can be constructed. We provide the expressions for both relations in Table 6.6, alongside their mean and maximum deviations. Notably, these mass-independent relations, which cover a broad range of mass ratios, are highly accurate.

Part IV

Summary

7. Summary, conclusions and future directions

In the context of this thesis we introduce a fundamentally new tool for studying general relativistic problems in astrophysics. In particular, we extend the Arepo code to perform simulations of general relativistic systems with dynamical spacetimes on a moving mesh (Part II). We discuss our findings in Section 7.1, while our main results are presented in [196]. In addition, we perform a systematic study of various GW asteroseismology relations and discuss the potential for additional EOS constraints (Part III). In Section 7.2 we provide concluding remarks for this study, while our work is presented in [197]. In both cases, we also comment on future directions.

7.1. General relativistic moving-mesh hydrodynamics simulations with Arepo

In this thesis, we perform moving-mesh simulations of NS systems with the Arepo code. The original implementation of Arepo solves the equations of Newtonian hydrodynamics, thus a number of modifications are required for the study of general relativistic systems. In particular, GRHD is implemented into the code based on the Valencia formulation. We couple a metric solver which adopts the CFC approximation to account for dynamical spacetimes. Finally, since our main focus in the current study is NS systems, we implement a microphysics module to account for the NS high-density EOS.

We validate our implementation by evolving static NSs and monitoring the frequency of the radial oscillation. We perform a series of simulations, considering both a fixed and a dynamical spacetime. Our results are in agreement with independent simulations performed with other tools. Moreover, the stars remain close to their initial equilibrium during the roughly 10 ms for which we evolve them. These tests showcase that our implementation can successfully simulate general relativistic systems, including a dynamical spacetime, on a moving mesh.

We discuss the first BNS merger simulation on a moving mesh. For this particular calculation, we employ a mesh which is well-adapted to the geometry and the mass distribution of the system, which demonstrates the flexibility of the code. We find that the resolution in high-density regions is comparable to those employed nowadays in merger simulations. The simulation run for a few weeks on roughly 200 cores, which highlights the potential for higher resolution calculations.

The general dynamics and qualitative features of the simulation agree with independent simulations employing either SPH or Eulerian grid-based methods. Notably, the timescales over which different dynamical features evolve in the post-merger phase are longer in our moving-mesh simulation compared to these independent calculations.

In particular, we find that the quasi-radial oscillation survives for a long time. Furthermore, the initial double-core structure, which forms after the merging, persists for more than 20 ms, significantly longer compared to fixed-grid calculations. Angular momentum also redistributes on longer timescales.

The observed prolonged timescales of major dynamical features in the post-merger phase may very well mean that the lifetime of the remnant is extended with respect to what other simulations report. This could have important implications. Considering that even at the very end of our simulation density spiral arms starting from the remnant can be clearly identified, the central object still loses mass. This material is either ejected or might end up in the surrounding torus. Material from the torus (or accretion disk) can also become gravitationally unbound at later times and contribute to the ejecta [160, 199, 234, 270, 314]. The amount of ejected material, as well as its properties (e.g. composition, entropy, geometric distribution), impacts heavy-element nucleosynthesis in the ejecta. Hence, the abundance pattern of produced heavy elements and the properties of the observable kilonova can potentially be affected by a prolonged remnant lifetime and accompanying mass ejection pattern. A systematic analysis requires to run the simulation further, until the gravitational collapse of the central object. To evaluate if and how r-process calculations and electromagnetic observables are affected, we need to monitor mass ejection and perform nucleosynthesis calculations in the ejecta. A more complete analysis would require to include additional mechanisms that might affect properties of the ejecta (e.g. neutrino transport, magnetic fields).

Focusing on the post-merger GW emission, we find that the dominant oscillation frequency is in good agreement with independent simulations of the system employing different codes. Notably, the GW signal is damped very slowly. The system strongly emits GWs during the whole post-merger phase that we simulate ($\approx$ 40 ms), while the GW signal amplitude remains large even at the end of the simulation.

The height of the peaks in the GW spectrum determines which features are detectable based on the sensitivity curves of the detectors. Compared to an independent SPH simulation, we find that the peaks in the GW spectrum extracted from the moving-mesh simulation are more pronounced. Hence, the strong GW emission in the moving-mesh simulation, which lasts for a long time, suggests a higher probability to observe the system. We note that to better estimate the detectability of the system through GWs, one should consider damping mechanisms which act in addition to GW emission, such as magnetic or bulk viscosity [19, 168, 214]. Furthermore, we need to systematically examine the effect that the CFC approximation has on the damping times.

Overall, the fact that dynamical features of the remnant survive for long times, as well as the slow damping of the GW signal, suggest that numerical viscosity is rather low in our simulation. We remark that taking into account additional damping mechanisms might result on shorter timescales. However, performing and interpreting simulations which are not significantly affected by numerics is important, if we wish to extract timescales which reliably reflect how different physical processes act . This is a rather important point, which highlights the potential benefits of employing the moving-mesh approach in the study of BNS mergers.

In summary, future work should further investigate the time scales over which dynamical features evolve in the post-merger phase. A systematic study, which considers a broad range of EOSs and binary masses, is required to determine if moving-mesh simulations consistently feature low numerical viscosity. Aspects like the lifetime of the remnant, the damping of the GW signal and heavy element nucleosynthesis in the ejecta should be considered in detail. These points could have important consequences on the detectability of mergers through GWs, the abundances of elements synthesized in such events and how we interpret electromagnetic observations based on modeling the kilonova.

Furthermore, the flexibility offered by AREPO, particularly regarding the mesh setup (e.g. mesh motion, geometry, adaptive refinement/derefinement), suggests that the code should be rather well-suited for the study of other general relativistic systems as well. Besides BNS mergers, the code can be employed to study systems such as NS-black hole mergers, black hole accretion, relativistic jets, accretion tori and NS-white dwarf systems.

Regarding future development of the code, adding support for fully temperature-dependent EOSs and neutrino transport is currently ongoing. Other directions, which might be considered, include implementing magnetic fields in the code and, based on the current communication infrastructure, coupling a fully general relativistic metric solver. We also plan to investigate the effect that a number of technical elements have on the simulations. Such aspects include implementing a more advanced Riemann solver, a more sophisticated description of the atmosphere and experimenting with various mesh setup details, e.g. different initial mesh geometries and refinement/derefinement criteria.

7.2. Frequency deviations in universal relations

Another direction, which we considered in this thesis, are GW asteroseismology relations for two distinct systems. Based on perturbative calculations we compute the $f-$mode frequencies $f_{\rm pert}$ in isolated NSs. In addition, we employ full 3D simulations of BNS systems to extract the GW frequency originating from the dominant fluid oscillation $f_{\rm peak}$ in BNS merger remnants. In both cases we consider a broad range of EOSs.

In the case of isolated stars, we consider relations between $f_{\rm pert}$ and stellar parameters such as the radius R, the moment of inertia I and the tidal deformability Λ. We construct fits between $f_{\rm pert}$ (or the mass-scaled $Mf_{\rm pert}$) and the various stellar parameters based on a consistent data set. This enables us to compare the accuracy of different relations. Relations involving the moment of inertia or the tidal deformability turn out to be the most accurate. Moreover, our analysis supports that the scatter of points in GW asteroseismology relations is, at least partially, influenced by the high-density EOS. We find similar results in the case of merger remnants, considering relations between $f_{\rm peak}$ and properties of isolated stars (see Tables 6.3 and A.1).

The main result of this work is that data points scatter in a very similar way when comparing relations referring to isolated NSs and BNS merger remnants side by side. This is particularly interesting, because each data point refers to a stellar model described by a specific EOS. In essence, when we inspect the position of individual data points with respect to the fit to all data, we are practically examining how a particular EOS yields stellar parameters which deviate from “mean” values predicted based on the complete EOS sample. The fact that data points distribute in a very similar manner for isolated NSs and merger remnants indicates that these deviations are a signature of the EOS.

As an illustrative example, we explicitly show that the frequency versus radius relation referring to 1.6 $M_{\odot}$ isolated stars features extremely similar deviations as the corresponding relation constructed for merger remnants of $1.35 + 1.35$ $M_{\odot}$ binary systems. Overall, we consider a number of different pairs of relations between GW frequencies and stellar parameters and verify that this finding holds for all the binary systems considered in this study (see Table 6.4). Notably, this systematic behavior is rather unexpected, because we compare oscillations in two very different systems. The $f-$mode in cold, isolated, non-rotating NSs and the dominant fluid oscillation in hot, massive, rapidly rotating merger remnants.

We study how the EOS influences the exact distribution of points in f_{pert} versus R relations. We trace the frequency deviations in such relations to the tidal Love number k_2. In particular, measuring frequency deviations results in a better determination of k_2. For a fixed stellar mass, k_2 and R fully determine Λ (equivalently k_2 and Λ fully determine R). Thus, better estimates of k_2 can be extremely useful considering that Λ or R can in principle be extracted from observations. We remark that inferring the sign of the frequency deviation from an observation already reduces the error in determining k_2 by half. Moreover, the reported agreement of frequency deviations between isolated NSs and BNS merger remnants supports that frequency deviations from BNS mergers can also be employed to better estimate k_2. A similar analysis of relations involving the frequency and tidal deformability yields constraints on the derivative with respect to the mass $d\Lambda^{1/5}/dM$.

Finally, we present relations between f_{pert} and f_{peak}, which hold for a broad range of binary system masses. In this direction, we also extend the data set to include unequal-mass binaries and produce rather accurate relations covering a wide range of binary masses and mass ratios.

Many different future directions can be considered. Directly inferring frequency deviations depends to a great extent on the accuracy of the theoretical relations to which the measurement should be compared. Relations constructed based on high precision 3D simulations can, in principle, further enhance the observed correlation of frequency deviations between isolated NSs and BNS remnants. Furthermore, highly accurate relations could result in an even better determination of k_2 from BNS observations. Hence, frequency deviations in BNS systems should be investigated with independent hydrodynamical codes. One such possibility would be AREPO, which treats hydrodynamics in a finite-volume fashion on a moving mesh, namely a completely different approach compared to the SPH code that we employ to extract frequency deviations. Another approach would be to consider perturbative calculations of equilibrium NSs with rotational profiles which resemble merger remnants [95, 175].

We only briefly considered frequency deviations in unequal-mass systems. A more systematic study is required to determine the effect of mass ratio on frequency deviations and potential observational applications. Similarly, subdominant peaks of the GW spectrum are only shortly mentioned. Frequency deviations of secondary features of the GW spectrum need to also be examined to ascertain whether they exhibit the same systematic behavior. Finally, extracting frequency deviations from GW signals offers the potential for more accurate GW asteroseismology relations, which take into consideration how the EOS influences the deviations.

A. Accuracy of relations between f_peak and stellar properties of static stars

In Chapter 6 we consider relations between the dominant post-merger frequency f_peak and various stellar properties of static stars with a fixed mass (e.g. Table 6.3 and Figs. 6.5, 6.6, 6.12 and 6.13). The fiducial mass of the static stars is a free parameter, which, however, affects the accuracy of the relation (see also [45]). Here we investigate which choices for the static star mass lead to the tightest relations for the various binary systems and static star properties that serve as independent variables. This discussion follows the appendix in [197].

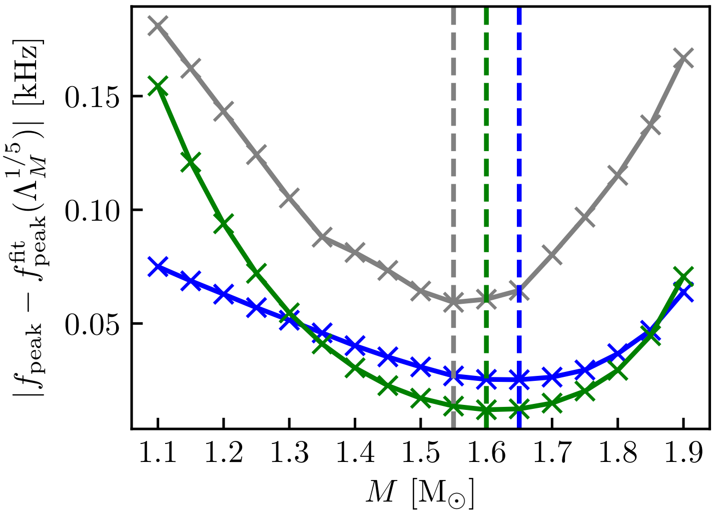

Figure A.1: Accuracy of relations of the form $f_\mathrm{peak}(\Lambda^{1/5}_M)$ for $1.35 + 1.35\ M_\odot$ binary systems versus the fiducial mass M. Three different figures of merit are shown. The gray curve depicts the maximum deviation, blue curve shows the average deviation and green curve illustrates the normalized sum of squared residuals of the least-squares fit. The minima of each curve is marked by a vertical dashed line of the same color. Adapted from [197].

We focus our attention on relations between f_peak and the four stellar properties discussed in Chapter 6, namely the radius R, the radius of the sphere containing 90% of the mass of the stellar configuration $R^{90\%}$, the radius R^cc where the rest-mass density equals the crust-core transition density ρ_cc and the fifth-root of the tidal deformability $\Lambda^{1/5}$. We employ three different metrics to evaluate the accuracy of the respective fits. In particular, we use the mean deviations, the maximum deviations and the sum of squared residuals of the least-squares fit.

Overall, we find good agreement between the three different figures of merit. For example, Fig. A.1 shows all three figures of merit for the relation of the form $f_{\text{peak}}(\Lambda_M^{1/5})$ for 1.35+1.35 $M_\odot$ binary systems and different values of the fiducial mass M. Based on the three distinct accuracy metrics, we identify $1.55-1.65$ $M_\odot$ as the optimal mass range for this particular binary system and relation.

Table A.1: Optimal range of fiducial masses which result in the tightest relations between post-merger frequencies and stellar parameters of static stars. The first column displays the masses of the binary systems. The second column indicates which stellar parameter is used as the independent variable in the respective fit. The third column shows the identified optimal mass range. The fourth column provides an upper limit on the average and maximum deviations computed in the corresponding mass range. The table is adapted from [197].

Binary masses $[M_\odot]$	Independent variable	Optimal mass range $[M_\odot]$	Mean/Max dev. [Hz]
$1.2+1.2$	R	$1.6-1.75$	$<(33,82)$
$1.2+1.2$	$R^{90\%}$	$1.5-1.6$	$<(20,49)$
$1.2+1.2$	R^{cc}	$1.7-1.75$	$<(18,57)$
$1.2+1.2$	$\Lambda^{1/5}$	$1.4-1.45$	$<(18,50)$
$1.35+1.35$	R	$1.7-1.8$	$<(38,91)$
$1.35+1.35$	$R^{90\%}$	$1.7-1.75$	$<(22,62)$
$1.35+1.35$	R^{cc}	$1.75-1.85$	$<(28,69)$
$1.35+1.35$	$\Lambda^{1/5}$	$1.55-1.65$	$<(27,65)$
$1.4+1.4$	R	$1.85-1.9$	$<(42,105)$
$1.4+1.4$	$R^{90\%}$	$1.8-1.85$	$<(30,99)$
$1.4+1.4$	R^{cc}	$1.85-1.9$	$<(28,98)$
$1.4+1.4$	$\Lambda^{1/5}$	$1.75-1.8$	$<(35,109)$
$1.5+1.5$	R	$1.75-1.8$	$<(33,76)$
$1.5+1.5$	$R^{90\%}$	$1.75-1.8$	$<(26,64)$
$1.5+1.5$	R^{cc}	1.9	$<(17,43)$
$1.5+1.5$	$\Lambda^{1/5}$	$1.65-1.75$	$<(30,73)$

Table A.1 lists the results of our analysis for all binary systems considered in Chapter 6 and independent variables. For each relation we identify the optimal range of fiducial masses, where all three figures of merit are minimized. In addition, we provide upper limits for the mean and maximum deviations for the respective relation within the optimal mass range. For all binary systems, relations w.r.t. the radius become more accurate for slightly higher values of the fiducial mass compared to tidal deformability relations. More massive binary systems correlate better with stellar properties of more massive static stars, as expected[1]. The remnants exhibit higher rest-mass densities in the interior compared to the two inspiralling stars. As a result, the identified mass ranges always refer to properties of static stars which are more massive compared to the each of the two companions.

---

[1] Binary systems with $M_{\text{tot}} = 3\ M_\odot$ deviate from this observation, because most EOSs result in a direct collapse to black hole after merging for such massive systems. Hence, the data set is significantly smaller compared to the data sets of less massive systems.

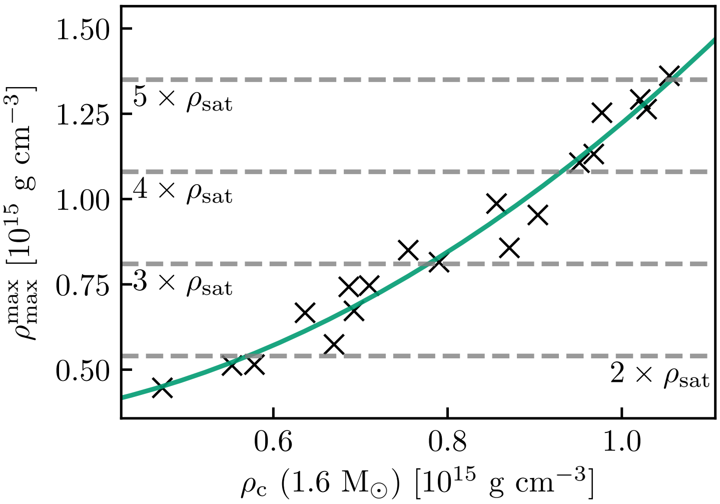

Figure A.2: Maximum rest-mass density $\rho_{\rm max}^{\rm max}$ found in remnants of $1.35 + 1.35\ M_\odot$ binary systems within the first few oscillation cycles after merging as a function of the central rest-mass densities $\rho_{\rm c}$ of $1.6\ M_\odot$ static stars modeled by the same EOS. A second-order fit to the data is presented with a solid green curve. The fit reads $\rho_{\rm max}^{\rm max} = 0.372 - 0.446\ \rho_{\rm c} + 1.296\ \rho_{\rm c}^2$. Horizontal dashed lines present densities in terms of the nuclear saturation density. Figure adapted from [197].

As shown in Table A.1, for each binary system, we identify a mass range of about $0.25\ M_\odot$, within which $f_{\rm peak}$ relations become most accurate for the four independent variables considered here. To better understand this result, we compare the rest-mass densities exhibited within the remnant in the first few milliseconds after merging to the central rest-mass densities $\rho_{\rm c}$ of static stars described by the same EOS and chosen such that they lie within the identified optimal mass range. A single characteristic density in the remnant cannot be uniquely defined, because in the early post-merger phase oscillations are strongly excited and the system is dynamically evolving. Here we track the maximum density within the remnant during the first few milliseconds and identify its maximum value[2]. We call this rest-mass density value $\rho_{\rm max}^{\rm max}$ (see [39, 59]). We show the extracted remnant densities for $1.35+1.35\ M_\odot$ systems versus the central densities of $1.6\ M_\odot$ static stars in Fig. A.2. Each point refers to a different EOS. Evidently, the densities at the center of $1.6\ M_\odot$ isolated stars are quite similar to the highest densities within the remnant in the early post-merge phase. This agreement demonstrates why the choice of such a fiducial mass results in tight relations. Binary systems described by softer EOSs collide typically with higher impact parameters and the remnant compression is more pronounced compared to stiff EOSs. Hence, they reach higher rest-mass densities in the remnant, which match better with central densities of higher fiducial masses. This aligns with the mass ranges reported in Table A.1, where for binary systems with a total mass of $2.7\ M_\odot$ the optimal fiducial masses extend also a bit higher than those reached in $1.6\ M_\odot$ static stars.

Summarizing, we conclude that the accuracy of relations between $f_{\rm peak}$ and different stellar properties of static stars is sensitive to the chosen fiducial mass of the

---

[2] An alternate definition which considers the average of the maximum rest-mass density over the first few milliseconds leads to very similar results.

static stellar configuration. The optimal mass range, which we identify based on three different figures of merit, varies for the various independent variables considered here, namely R, $R^{90\%}$, R^{cc} and $\Lambda^{1/5}$. Typically, the tightest relations occur when considering properties of static stars with densities comparable to the densities reached in the remnant over the first few oscillation cycles after merging. Given that the deviations are defined with respect to the fit to the data points, the various figures of merit should, up to some extent, be affected by the set of EOSs considered, the functional form of the fit and potentially details of the numerical modeling. Nevertheless, we expect that the ranges reported in Table A.1 are robust and fiducial masses within these ranges result in tight relations, because the minima of the different accuracy metrics in Fig. A.1 are relatively broad.

Acknowledgments

First and foremost, I would like to thank my supervisor Andreas Bauswein for his guidance and support that made this thesis possible. He always provided invaluable feedback, as well as numerous ideas regarding ongoing work and potential directions. In addition, he always found time to discuss, understood that life extends beyond the office and created an environment where I felt that I can share my ideas and be creative. I could not have asked for a better supervision.

I wish to acknowledge all the people I had the pleasure to collaborate with in the projects discussed in this thesis. All of them provided insights, interesting ideas and feedback that greatly improved the quality of this work. In particular, I want to thank: Volker Springel who provided me with access to Arepo, which served as the basis for most of the developments in this thesis. Rüdiger Pakmor for being always available to discuss and answer my many questions related to Arepo. Friedrich Röpke for providing me with many opportunities to meet and discuss with people who utilize Arepo to study different physical systems, sharing his experience in many university related issues and being part of my examination committee. Nikolaos Stergioulas for always sharing his expertise in neutron stars, as well as his constant guidance and support since my bachelor years. Theodoros Soultanis for always being eager to share his experience with fixed-grid codes and check his simulations or set up new ones, so that we can compare notes. In these past few years, besides a colleague, he has also been a friend.

Furthermore, I wish to thank Gabriel Martínez-Pinedo for many interesting discussions and generously sharing his knowledge. Many thanks go also to Thomas Neff for his aid and advice on the various aspects of working with a High-Performance Computing cluster.

I am grateful to Björn Malte Schäfer for agreeing to be the second referee of this thesis and Klaus Reygers for joining my examination committee.

I feel grateful for all the people that made life much more enjoyable during the past years. Thankfully, they are too many to fit in a paragraph by name. As an, admittedly incomplete, attempt, thank you to: Sebastian, who also helped me with the translation of the abstract to German, and Vimal for all the discussions, the hikes, the fun and for being such great collaborators. My office mates over the last years, Stelio, Christian, Gerrit, Ignacio and Zafar for the many discussions inside and outside the office. All the people that I met at GSI during these years for the interesting conversations and the nice times we shared. The members of the PSO group that made me feel welcome whenever I was at HITS. The friends I made in Darmstadt for all the fun times and support. The many people I met during my studies in Thessaloniki and Munich, that still text me as if we live a few blocks away. My friends from my hometown, Trikala, who always treat me like I only left for a few days and are still part of my everyday life.

I also wish to acknowledge the late John Hugh Seiradakis. I had the pleasure to

meet him before even starting my bachelor studies and through his advice and support he was a mentor to me.

I acknowledge financial support by the European Research Council (ERC) under the European Union's Horizon 2020 research and innovation programme under grant agreement No. 759253. I also want to acknowledge the GSI Helmholtzzentrum für Schwerionenforschung for providing a wonderful workspace and the needed computational resources via the Virgo and, previously, Kronos clusters.

Last but not least, a few very special thanks. To my sister, Georgia, and my parents, Irini and Thanasi, for their endless love, support and trust in me and my decisions, which have made this work, as well as my journey in science, possible. To Eleftheria for being a constant spark of excitement and creativity and for being there when I needed to talk. Eleftheria and Georgia decided to further add to this support by proof-reading and helping me improve this thesis and for that, I am also thankful.

List of publications

Results presented in this thesis:

[1] **G. Lioutas**, A. Bauswein, T. Soultanis, R. Pakmor, V. Springel, and F. K. Röpke. General relativistic moving-mesh hydrodynamics simulations with AREPO and applications to neutron star mergers. *arXiv e-prints*, page arXiv:2208.04267, Aug. 2022. (submitted to MNRAS)

[Discussed in: Section 1.2, Chapter 3, Chapter 4, Chapter 5, Section 7.1]

[2] **G. Lioutas**, A. Bauswein, and N. Stergioulas. Frequency deviations in universal relations of isolated neutron stars and postmerger remnants. *Phys. Rev. D*, 104(4):043011, Aug. 2021.

[Discussed in: Section 1.3, Chapter 6, Section 7.2, Appendix A]

Results not presented in this thesis:

[1] A. Bauswein, S. Blacker, **G. Lioutas**, T. Soultanis, V. Vijayan, and N. Stergioulas. Systematics of prompt black-hole formation in neutron star mergers. *Phys. Rev. D*, 103(12):123004, June 2021.

[2] **G. Lioutas** and N. Stergioulas. Universal and approximate relations for the gravitational-wave damping timescale of f-modes in neutron stars. *Gen. Relativ. Gravit.*, 50(1):12, Jan. 2018.

[3] **G. Lioutas** and N. Stergioulas. The gravitational wave damping timescales of f-modes in neutron stars. *J. Phys. Conf. Ser.*, 1667:012026, oct 2020.

Bibliography

[1] B. P. Abbott, R. Abbott, T. D. Abbott, M. R. Abernathy, K. Ackley, C. Adams, P. Addesso, R. X. Adhikari, V. B. Adya, C. Affeldt, et al. Exploring the sensitivity of next generation gravitational wave detectors. *Classical and Quantum Gravity*, 34(4):044001, Feb. 2017.

[2] B. P. Abbott, R. Abbott, T. D. Abbott, S. Abraham, F. Acernese, K. Ackley, C. Adams, R. X. Adhikari, V. B. Adya, C. Affeldt, et al. GWTC-1: A Gravitational-Wave Transient Catalog of Compact Binary Mergers Observed by LIGO and Virgo during the First and Second Observing Runs. *Physical Review X*, 9(3):031040, July 2019.

[3] B. P. Abbott, R. Abbott, T. D. Abbott, S. Abraham, F. Acernese, K. Ackley, C. Adams, R. X. Adhikari, V. B. Adya, C. Affeldt, et al. GW190425: Observation of a Compact Binary Coalescence with Total Mass $\sim 3.4\ \mathrm{M}_{\odot}$. *Astrophys. J. Lett.*, 892(1):L3, Mar. 2020.

[4] B. P. Abbott, R. Abbott, T. D. Abbott, S. Abraham, F. Acernese, K. Ackley, C. Adams, V. B. Adya, C. Affeldt, M. Agathos, et al. Prospects for observing and localizing gravitational-wave transients with Advanced LIGO, Advanced Virgo and KAGRA. *Living Reviews in Relativity*, 23(1):3, Sept. 2020.

[5] B. P. Abbott, R. Abbott, T. D. Abbott, F. Acernese, K. Ackley, C. Adams, T. Adams, P. Addesso, R. X. Adhikari, V. B. Adya, et al. Gravitational Waves and Gamma-Rays from a Binary Neutron Star Merger: GW170817 and GRB 170817A. *Astrophys. J. Lett.*, 848(2):L13, Oct. 2017.

[6] B. P. Abbott, R. Abbott, T. D. Abbott, F. Acernese, K. Ackley, C. Adams, T. Adams, P. Addesso, R. X. Adhikari, V. B. Adya, et al. GW170817: Observation of Gravitational Waves from a Binary Neutron Star Inspiral. *Phys. Rev. Lett.*, 119(16):161101, Oct. 2017.

[7] B. P. Abbott, R. Abbott, T. D. Abbott, F. Acernese, K. Ackley, C. Adams, T. Adams, P. Addesso, R. X. Adhikari, V. B. Adya, et al. Multi-messenger Observations of a Binary Neutron Star Merger. *Astrophys. J. Lett.*, 848(2):L12, Oct. 2017.

[8] B. P. Abbott, R. Abbott, T. D. Abbott, F. Acernese, K. Ackley, C. Adams, T. Adams, P. Addesso, R. X. Adhikari, V. B. Adya, et al. Search for Post-merger Gravitational Waves from the Remnant of the Binary Neutron Star Merger GW170817. *Astrophys. J. Lett.*, 851(1):L16, Dec. 2017.

[9] B. P. Abbott, R. Abbott, T. D. Abbott, F. Acernese, K. Ackley, C. Adams, T. Adams, P. Addesso, R. X. Adhikari, V. B. Adya, et al. GW170817: Measurements of Neutron Star Radii and Equation of State. *Phys. Rev. Lett.*, 121(16):161101, Oct. 2018.

[10] B. P. Abbott, R. Abbott, T. D. Abbott, F. Acernese, K. Ackley, C. Adams, T. Adams, P. Addesso, R. X. Adhikari, V. B. Adya, et al. Properties of the Binary Neutron Star Merger GW170817. *Physical Review X*, 9(1):011001, Jan. 2019.

[11] B. P. Abbott, R. Abbott, T. D. Abbott, F. Acernese, K. Ackley, C. Adams, T. Adams, P. Addesso, R. X. Adhikari, V. B. Adya, et al. Search for Gravitational Waves from a Long-lived Remnant of the Binary Neutron Star Merger GW170817. *Astrophys. J.*, 875(2):160, Apr. 2019.

[12] R. Abbott, T. D. Abbott, S. Abraham, F. Acernese, K. Ackley, A. Adams, C. Adams, R. X. Adhikari, V. B. Adya, C. Affeldt, et al. GWTC-2: Compact Binary Coalescences Observed by LIGO and Virgo during the First Half of the Third Observing Run. *Physical Review X*, 11(2):021053, Apr. 2021.

[13] F. Acernese, M. Agathos, K. Agatsuma, D. Aisa, N. Allemandou, A. Allocca, J. Amarni, P. Astone, G. Balestri, G. Ballardin, et al. Advanced Virgo: a second-generation interferometric gravitational wave detector. *Classical and Quantum Gravity*, 32(2):024001, Jan. 2015.

[14] K. Ackley, V. B. Adya, P. Agrawal, P. Altin, G. Ashton, M. Bailes, E. Baltinas, A. Barbuio, D. Beniwal, C. Blair, et al. Neutron Star Extreme Matter Observatory: A kilohertz-band gravitational-wave detector in the global network. *Publ. Astron. Soc. Aust.*, 37:e047, Nov. 2020.

[15] N. Aggarwal, O. D. Aguiar, A. Bauswein, G. Cella, S. Clesse, A. M. Cruise, V. Domcke, D. G. Figueroa, A. Geraci, M. Goryachev, et al. Challenges and opportunities of gravitational-wave searches at MHz to GHz frequencies. *Living Reviews in Relativity*, 24(1):4, Dec. 2021.

[16] A. Akmal, V. R. Pandharipande, and D. G. Ravenhall. Equation of state of nucleon matter and neutron star structure. *Phys. Rev. C*, 58:1804–1828, Sept. 1998.

[17] M. Alcubierre. *Introduction to 3+1 Numerical Relativity.* International Series of Monographs on Physics. OUP Oxford, 2008.

[18] M. Alford, M. Braby, M. Paris, and S. Reddy. Hybrid stars that masquerade as neutron stars. *Astrophys. J*, 629:969–978, Aug. 2005.

[19] M. G. Alford and S. P. Harris. Damping of density oscillations in neutrino-transparent nuclear matter. *Phys. Rev. C*, 100(3):035803, Sept. 2019.

[20] J. Alsing, H. O. Silva, and E. Berti. Evidence for a maximum mass cut-off in the neutron star mass distribution and constraints on the equation of state. *Mon. Not. R. Astron. Soc.*, 478(1):1377–1391, July 2018.

[21] D. Alvarez-Castillo, A. Ayriyan, S. Benic, D. Blaschke, H. Grigorian, and S. Typel. New class of hybrid eos and bayesian m - r data analysis. *European Physical Journal A*, 52:69, Mar. 2016.

[22] N. Andersson and K. D. Kokkotas. Towards gravitational wave asteroseismology. *Mon. Not. R. Astron. Soc*, 299(4):1059–1068, Oct. 1998.

[23] N. Andersson, K. D. Kokkotas, and B. F. Schutz. A new numerical approach to the oscillation modes of relativistic stars. *Mon. Not. R. Astron. Soc.*, 274(4):1039–1048, June 1995.

[24] J. Antoniadis, P. C. C. Freire, N. Wex, T. M. Tauris, R. S. Lynch, M. H. van Kerkwijk, M. Kramer, C. Bassa, V. S. Dhillon, T. Driebe, et al. A Massive Pulsar in a Compact Relativistic Binary. *Science*, 340(6131):448, Apr. 2013.

[25] J. Antoniadis, T. M. Tauris, F. Ozel, E. Barr, D. J. Champion, and P. C. C. Freire. The millisecond pulsar mass distribution: Evidence for bimodality and constraints on the maximum neutron star mass. *arXiv e-prints*, page arXiv:1605.01665, May 2016.

[26] I. Arcavi. The First Hours of the GW170817 Kilonova and the Importance of Early Optical and Ultraviolet Observations for Constraining Emission Models. *Astrophys. J. Lett.*, 855(2):L23, Mar. 2018.

[27] R. Arnowitt, S. Deser, and C. W. Misner. Republication of: The dynamics of general relativity. *Gen. Relativ. Gravit*, 40(9):1997–2027, Sept. 2008.

[28] Z. Arzoumanian, A. Brazier, S. Burke-Spolaor, S. Chamberlin, S. Chatterjee, B. Christy, J. M. Cordes, N. J. Cornish, F. Crawford, H. Thankful Cromartie, et al. The NANOGrav 11-year Data Set: High-precision Timing of 45 Millisecond Pulsars. *Astrophys. J., Suppl. Ser.*, 235(2):37, Apr. 2018.

[29] E. H. Ayache, H. J. van Eerten, and R. W. Eardley. GAMMA: a new method for modelling relativistic hydrodynamics and non-thermal emission on a moving mesh. *Mon. Not. R. Astron. Soc.*, 510(1):1315–1330, Feb. 2022.

[30] L. Baiotti. Gravitational waves from neutron star mergers and their relation to the nuclear equation of state. *Progress in Particle and Nuclear Physics*, 109:103714, Nov. 2019.

[31] L. Baiotti, B. Giacomazzo, and L. Rezzolla. Accurate evolutions of inspiralling neutron-star binaries: Prompt and delayed collapse to a black hole. *Phys. Rev. D*, 78(8):084033, Oct. 2008.

[32] L. Baiotti and L. Rezzolla. Binary neutron star mergers: a review of Einstein's richest laboratory. *Reports on Progress in Physics*, 80(9):096901, Sept. 2017.

[33] T. Baker, E. Bellini, P. G. Ferreira, M. Lagos, J. Noller, and I. Sawicki. Strong Constraints on Cosmological Gravity from GW170817 and GRB 170817A. *Phys. Rev. Lett.*, 119(25):251301, Dec. 2017.

[34] S. Banik, M. Hempel, and D. Bandyopadhyay. New hyperon equations of state for supernovae and neutron stars in density-dependent hadron field theory. *Astrophys. J., Suppl. Ser.*, 214:22, Oct. 2014.

[35] F. Banyuls, J. A. Font, J. M. Ibáñez, J. M. Martí, and J. A. Miralles. Numerical $\{3+1\}$ General Relativistic Hydrodynamics: A Local Characteristic Approach. *Astrophys. J.*, 476(1):221–231, Feb. 1997.

[36] T. W. Baumgarte, G. B. Cook, M. A. Scheel, S. L. Shapiro, and S. A. Teukolsky. General relativistic models of binary neutron stars in quasiequilibrium. *Phys. Rev. D*, 57(12):7299–7311, June 1998.

[37] T. W. Baumgarte and S. L. Shapiro. *Numerical Relativity: Solving Einstein's Equations on the Computer*. Cambridge University Press, 2010.

[38] T. W. Baumgarte, S. L. Shapiro, and M. Shibata. On the Maximum Mass of Differentially Rotating Neutron Stars. *Astrophys. J. Lett.*, 528(1):L29–L32, Jan. 2000.

[39] A. Bauswein, N.-U. F. Bastian, D. B. Blaschke, K. Chatziioannou, J. A. Clark, T. Fischer, and M. Oertel. Identifying a First-Order Phase Transition in Neutron-Star Mergers through Gravitational Waves. *Phys. Rev. Lett.*, 122(6):061102, Feb. 2019.

[40] A. Bauswein, T. W. Baumgarte, and H. T. Janka. Prompt Merger Collapse and the Maximum Mass of Neutron Stars. *Phys. Rev. Lett.*, 111(13):131101, Sept. 2013.

[41] A. Bauswein, S. Blacker, G. Lioutas, T. Soultanis, V. Vijayan, and N. Stergioulas. Systematics of prompt black-hole formation in neutron star mergers. *Phys. Rev. D*, 103(12):123004, June 2021.

[42] A. Bauswein, S. Blacker, V. Vijayan, N. Stergioulas, K. Chatziioannou, J. A. Clark, N.-U. F. Bastian, D. B. Blaschke, M. Cierniak, and T. Fischer. Equation of State Constraints from the Threshold Binary Mass for Prompt Collapse of Neutron Star Mergers. *Phys. Rev. Lett.*, 125(14):141103, Oct. 2020.

[43] A. Bauswein, S. Goriely, and H. T. Janka. Systematics of Dynamical Mass Ejection, Nucleosynthesis, and Radioactively Powered Electromagnetic Signals from Neutron-star Mergers. *Astrophys. J.*, 773(1):78, Aug. 2013.

[44] A. Bauswein and H. T. Janka. Measuring Neutron-Star Properties via Gravitational Waves from Neutron-Star Mergers. *Phys. Rev. Lett.*, 108(1):011101, Jan. 2012.

[45] A. Bauswein, H. T. Janka, K. Hebeler, and A. Schwenk. Equation-of-state dependence of the gravitational-wave signal from the ring-down phase of neutron-star mergers. *Phys. Rev. D*, 86(6):063001, Sept. 2012.

[46] A. Bauswein, H. T. Janka, and R. Oechslin. Testing approximations of thermal effects in neutron star merger simulations. *Phys. Rev. D*, 82(8):084043, Oct. 2010.

[47] A. Bauswein, O. Just, H.-T. Janka, and N. Stergioulas. Neutron-star Radius Constraints from GW170817 and Future Detections. *Astrophys. J. Lett.*, 850(2):L34, Dec. 2017.

[48] A. Bauswein, R. Oechslin, and H. T. Janka. Discriminating strange star mergers from neutron star mergers by gravitational-wave measurements. *Phys. Rev. D*, 81(2):024012, Jan. 2010.

[49] A. Bauswein and N. Stergioulas. Unified picture of the post-merger dynamics and gravitational wave emission in neutron star mergers. *Phys. Rev. D*, 91(12):124056, June 2015.

[50] A. Bauswein and N. Stergioulas. Unified picture of the post-merger dynamics and gravitational wave emission in neutron star mergers. *Phys. Rev. D*, 91(12):124056, June 2015.

[51] A. Bauswein and N. Stergioulas. Spectral classification of gravitational-wave emission and equation of state constraints in binary neutron star mergers. *Journal of Physics G Nuclear Physics*, 46(11):113002, Nov. 2019.

[52] A. Bauswein, N. Stergioulas, and H. T. Janka. Revealing the high-density equation of state through binary neutron star mergers. *Phys. Rev. D*, 90(2):023002, July 2014.

[53] A. Bauswein, N. Stergioulas, and H.-T. Janka. Exploring properties of high-density matter through remnants of neutron-star mergers. *European Physical Journal A*, 52:56, Mar. 2016.

[54] E. Berger. Short-Duration Gamma-Ray Bursts. *Annu. Rev. Astron. Astrophys.*, 52:43–105, Aug. 2014.

[55] S. Bernuzzi. Neutron star merger remnants. *General Relativity and Gravitation*, 52(11):108, Nov. 2020.

[56] S. Bernuzzi and T. Dietrich. Gravitational waveforms from binary neutron star mergers with high-order weighted-essentially-nonoscillatory schemes in numerical relativity. *Phys. Rev. D*, 94(6):064062, Sept. 2016.

[57] S. Bernuzzi, T. Dietrich, and A. Nagar. Modeling the Complete Gravitational Wave Spectrum of Neutron Star Mergers. *Phys. Rev. Lett.*, 115(9):091101, Aug. 2015.

[58] L. Bildsten and C. Cutler. Tidal Interactions of Inspiraling Compact Binaries. *Astrophys. J.*, 400:175, Nov. 1992.

[59] S. Blacker, N.-U. F. Bastian, A. Bauswein, D. B. Blaschke, T. Fischer, M. Oertel, T. Soultanis, and S. Typel. Constraining the onset density of the hadron-quark phase transition with gravitational-wave observations. *Phys. Rev. D*, 102(12):123023, Dec. 2020.

[60] L. Blanchet, T. Damour, and G. Schaefer. Post-Newtonian hydrodynamics and post-Newtonian gravitational wave generation for numerical relativity. *Mon. Not. R. Astron. Soc.*, 242:289–305, Jan. 1990.

[61] S. Bose, K. Chakravarti, L. Rezzolla, B. S. Sathyaprakash, and K. Takami. Neutron-Star Radius from a Population of Binary Neutron Star Mergers. *Phys. Rev. Lett.*, 120(3):031102, Jan. 2018.

[62] M. Breschi, S. Bernuzzi, F. Zappa, M. Agathos, A. Perego, D. Radice, and A. Nagar. Kilohertz gravitational waves from binary neutron star remnants: Time-domain model and constraints on extreme matter. *Phys. Rev. D*, 100(10):104029, Nov. 2019.

[63] W. L. Briggs, V. E. Henson, and S. F. McCormick. *A Multigrid Tutorial (2nd Ed.)*. Society for Industrial and Applied Mathematics, USA, 2000.

[64] M. Bruni, S. Matarrese, S. Mollerach, and S. Sonego. Perturbations of spacetime: gauge transformations and gauge invariance at second order and beyond. *Class. Quantum Gravity*, 14(9):2585–2606, Sept. 1997.

[65] G. F. Burgio, H. J. Schulze, I. Vidaña, and J. B. Wei. Neutron stars and the nuclear equation of state. *Prog. Part. Nucl. Phys.*, 120:103879, Sept. 2021.

[66] A. Campolattaro and K. S. Thorne. Nonradial Pulsation of General-Relativistic Stellar Models. V. Analytic Analysis for L = 1. *Astrophys. J.*, 159:847, Mar. 1970.

[67] K. Chakravarti and N. Andersson. Exploring universality in neutron star mergers. *Mon. Not. R. Astron. Soc.*, 497(4):5480–5484, Oct. 2020.

[68] T. K. Chan, Y. H. Sham, P. T. Leung, and L. M. Lin. Multipolar universal relations between f -mode frequency and tidal deformability of compact stars. *Phys. Rev. D*, 90(12):124023, Dec. 2014.

[69] S. Chandrasekhar. The Dynamical Instability of Gaseous Masses Approaching the Schwarzschild Limit in General Relativity. *Astrophys. J.*, 140:417, Aug. 1964.

[70] P. Chang and Z. B. Etienne. General relativistic hydrodynamics on a moving-mesh I: static space-times. *Mon. Not. R. Astron. Soc.*, 496(1):206–214, July 2020.

[71] P. Chang, J. Wadsley, and T. R. Quinn. A moving-mesh hydrodynamic solver for ChaNGa. *Mon. Not. R. Astron. Soc.*, 471(3):3577–3589, Nov. 2017.

[72] G. Chanmugam. Radial oscillations of zero-temperature white dwarfs and neutron stars below nuclear densities. *Astrophys. J.*, 217:799–808, Nov. 1977.

[73] K. Chatziioannou, J. A. Clark, A. Bauswein, M. Millhouse, T. B. Littenberg, and N. Cornish. Inferring the post-merger gravitational wave emission from binary neutron star coalescences. *Phys. Rev. D*, 96(12):124035, Dec. 2017.

[74] C. Chirenti, G. H. de Souza, and W. Kastaun. Fundamental oscillation modes of neutron stars: Validity of universal relations. *Phys. Rev. D*, 91(4):044034, Feb. 2015.

[75] J. Clark, A. Bauswein, L. Cadonati, H. T. Janka, C. Pankow, and N. Stergioulas. Prospects for high frequency burst searches following binary neutron star coalescence with advanced gravitational wave detectors. *Phys. Rev. D*, 90(6):062004, Sept. 2014.

[76] J. A. Clark, A. Bauswein, N. Stergioulas, and D. Shoemaker. Observing gravitational waves from the post-merger phase of binary neutron star coalescence. *Classical and Quantum Gravity*, 33(8):085003, Apr. 2016.

[77] P. Colella and P. R. Woodward. The Piecewise Parabolic Method (PPM) for Gas-Dynamical Simulations. *J. Comput. Phys.*, 54:174–201, Sept. 1984.

[78] G. B. Cook, S. L. Shapiro, and S. A. Teukolsky. Spin-up of a Rapidly Rotating Star by Angular Momentum Loss: Effects of General Relativity. *Astrophys. J.*, 398:203, Oct. 1992.

[79] G. B. Cook, S. L. Shapiro, and S. A. Teukolsky. Rapidly Rotating Neutron Stars in General Relativity: Realistic Equations of State. *Astrophys. J.*, 424:823, Apr. 1994.

[80] M. W. Coughlin, T. Ahumada, S. Anand, K. De, M. J. Hankins, M. M. Kasliwal, L. P. Singer, E. C. Bellm, I. Andreoni, S. B. Cenko, et al. GROWTH on S190425z: Searching Thousands of Square Degrees to Identify an Optical or Infrared Counterpart to a Binary Neutron Star Merger with the Zwicky Transient Facility and Palomar Gattini-IR. *Astrophys. J. Lett.*, 885(1):L19, Nov. 2019.

[81] D. A. Coulter, R. J. Foley, C. D. Kilpatrick, M. R. Drout, A. L. Piro, B. J. Shappee, M. R. Siebert, J. D. Simon, N. Ulloa, D. Kasen, B. F. Madore, A. Murguia-Berthier, Y. C. Pan, J. X. Prochaska, E. Ramirez-Ruiz, A. Rest, and C. Rojas-Bravo. Swope Supernova Survey 2017a (SSS17a), the optical counterpart to a gravitational wave source. *Science*, 358(6370):1556–1558, Dec. 2017.

[82] R. Courant, K. Friedrichs, and H. Lewy. Über die partiellen Differenzengleichungen der mathematischen Physik. *Math. Ann.*, 100:32–74, Jan. 1928. in German.

[83] R. Courant, K. Friedrichs, and H. Lewy. On the Partial Difference Equations of Mathematical Physics. *IBM J. Res. Dev.*, 11:215–234, Mar. 1967.

[84] J. J. Cowan, C. Sneden, J. E. Lawler, A. Aprahamian, M. Wiescher, K. Langanke, G. Martínez-Pinedo, and F.-K. Thielemann. Origin of the heaviest elements: The rapid neutron-capture process. *Reviews of Modern Physics*, 93(1):015002, Jan. 2021.

[85] H. T. Cromartie, E. Fonseca, S. M. Ransom, P. B. Demorest, Z. Arzoumanian, H. Blumer, P. R. Brook, M. E. DeCesar, T. Dolch, J. A. Ellis, et al. Relativistic Shapiro delay measurements of an extremely massive millisecond pulsar. *Nature Astronomy*, 4:72–76, Jan. 2020.

[86] T. Damour and A. Nagar. Effective one body description of tidal effects in inspiralling compact binaries. *Phys. Rev. D*, 81(8):084016, Apr. 2010.

[87] M. Darwish and F. Moukalled. Tvd schemes for unstructured grids. *International Journal of Heat and Mass Transfer*, 46(4):599–611, 2003.

[88] S. De, D. Finstad, J. M. Lattimer, D. A. Brown, E. Berger, and C. M. Biwer. Tidal Deformabilities and Radii of Neutron Stars from the Observation of GW170817. *Phys. Rev. Lett.*, 121(9):091102, Aug. 2018.

[89] W. Dehnen and H. Aly. Improving convergence in smoothed particle hydrodynamics simulations without pairing instability. *Mon. Not. R. Astron. Soc*, 425(2):1068–1082, Sept. 2012.

[90] P. B. Demorest, T. Pennucci, S. M. Ransom, M. S. E. Roberts, and J. W. T. Hessels. A two-solar-mass neutron star measured using Shapiro delay. *Nature*, 467(7319):1081–1083, Oct. 2010.

[91] S. Detweiler and L. Lindblom. On the nonradial pulsations of general relativistic stellar models. *Astrophys. J.*, 292:12–15, May 1985.

[92] P. Diener, S. Rosswog, and F. Torsello. Simulating neutron star mergers with the Lagrangian Numerical Relativity code SPHINCS_BSSN. *European Physical Journal A*, 58(4):74, Apr. 2022.

[93] T. Dietrich, T. Hinderer, and A. Samajdar. Interpreting binary neutron star mergers: describing the binary neutron star dynamics, modelling gravitational waveforms, and analyzing detections. *General Relativity and Gravitation*, 53(3):27, Mar. 2021.

[94] T. Dietrich, D. Radice, S. Bernuzzi, F. Zappa, A. Perego, B. Brügmann, S. Vivekanandji Chaurasia, R. Dudi, W. Tichy, and M. Ujevic. CoRe database of binary neutron star merger waveforms. *Classical and Quantum Gravity*, 35(24):24LT01, Dec. 2018.

[95] D. D. Doneva, E. Gaertig, K. D. Kokkotas, and C. Krüger. Gravitational wave asteroseismology of fast rotating neutron stars with realistic equations of state. *Phys. Rev. D*, 88(4):044052, Aug. 2013.

[96] K. L. Dooley, J. R. Leong, T. Adams, C. Affeldt, A. Bisht, C. Bogan, J. Degallaix, C. Gräf, S. Hild, J. Hough, et al. GEO 600 and the GEO-HF upgrade program: successes and challenges. *Classical and Quantum Gravity*, 33(7):075009, Apr. 2016.

[97] F. Douchin and P. Haensel. A unified equation of state of dense matter and neutron star structure. *Astron. Astrophys.*, 380:151–167, Dec. 2001.

[98] C. Ducoin, J. Margueron, C. Providência, and I. Vidaña. Core-crust transition in neutron stars: Predictivity of density developments. *Phys. Rev. C*, 83(4):045810, Apr. 2011.

[99] M. D. Duez, P. Marronetti, S. L. Shapiro, and T. W. Baumgarte. Hydrodynamic simulations in 3+1 general relativity. *Phys. Rev. D*, 67(2):024004, Jan. 2003.

[100] P. C. Duffell and A. I. MacFadyen. TESS: A Relativistic Hydrodynamics Code on a Moving Voronoi Mesh. *Astrophys. J. Suppl. Ser.*, 197(2):15, Dec. 2011.

[101] P. C. Duffell and A. I. MacFadyen. Global Calculations of Density Waves and Gap Formation in Protoplanetary Disks Using a Moving Mesh. *Astrophys. J.*, 755(1):7, Aug. 2012.

[102] P. C. Duffell and A. I. MacFadyen. Rayleigh-Taylor Instability in a Relativistic Fireball on a Moving Computational Grid. *Astrophys. J.*, 775(2):87, Oct. 2013.

[103] W. E. East, V. Paschalidis, F. Pretorius, and S. L. Shapiro. Relativistic simulations of eccentric binary neutron star mergers: One-arm spiral instability and effects of neutron star spin. *Phys. Rev. D*, 93(2):024011, Jan. 2016.

[104] P. J. Easter, S. Ghonge, P. D. Lasky, A. R. Casey, J. A. Clark, F. Hernandez Vivanco, and K. Chatziioannou. Detection and parameter estimation of binary neutron star merger remnants. *Phys. Rev. D*, 102(4):043011, Aug. 2020.

[105] P. J. Easter, P. D. Lasky, A. R. Casey, L. Rezzolla, and K. Takami. Computing fast and reliable gravitational waveforms of binary neutron star merger remnants. *Phys. Rev. D*, 100(4):043005, Aug. 2019.

[106] D. Eichler, M. Livio, T. Piran, and D. N. Schramm. Nucleosynthesis, neutrino bursts and γ-rays from coalescing neutron stars. *Nature*, 340(6229):126–128, July 1989.

[107] D. Eichler, M. Livio, T. Piran, and D. N. Schramm. Nucleosynthesis, Neutrino Bursts and Gamma-Rays from Coalescing Neutron Stars. *Nature*, 340:126–128, 1989.

[108] B. Einfeldt. On Godunov-Type Methods for Gas Dynamics. *SIAM J. Numer. Anal.*, 25(2):294–318, Apr. 1988.

[109] E. D. Fackerell. Solutions of Zerilli's Equation for Even-Parity Gravitational Perturbations. *Astrophys. J.*, 166:197, May 1971.

[110] S. Fairhurst. Improved source localization with LIGO-India. In *Journal of Physics Conference Series*, volume 484 of *Journal of Physics Conference Series*, page 012007, Mar. 2014.

[111] N. Farrow, X.-J. Zhu, and E. Thrane. The Mass Distribution of Galactic Double Neutron Stars. *Astrophys. J.*, 876(1):18, May 2019.

[112] F. J. Fattoyev, J. Piekarewicz, and C. J. Horowitz. Neutron Skins and Neutron Stars in the Multimessenger Era. *Phys. Rev. Lett.*, 120(17):172702, Apr. 2018.

[113] G. Faye and G. Schäfer. Optimizing the third-and-a-half post-Newtonian gravitational radiation-reaction force for numerical simulations. *Phys. Rev. D*, 68(8):084001, Oct. 2003.

[114] G. Fiorella Burgio and A. F. Fantina. Nuclear Equation of State for Compact Stars and Supernovae. In L. Rezzolla, P. Pizzochero, D. I. Jones, N. Rea, and I. Vidaña, editors, *Astrophysics and Space Science Library*, volume 457 of *Astrophysics and Space Science Library*, page 255, Jan. 2018.

[115] J. A. Font. Numerical Hydrodynamics and Magnetohydrodynamics in General Relativity. *Living Reviews in Relativity*, 11(1):7, Sept. 2008.

[116] J. A. Font, T. Goodale, S. Iyer, M. Miller, L. Rezzolla, E. Seidel, N. Stergioulas, W.-M. Suen, and M. Tobias. Three-dimensional numerical general relativistic hydrodynamics. II. Long-term dynamics of single relativistic stars. *Phys. Rev. D*, 65(8):084024, Apr. 2002.

[117] J. A. Font, M. Miller, W.-M. Suen, and M. Tobias. Three-dimensional numerical general relativistic hydrodynamics: Formulations, methods, and code tests. *Phys. Rev. D*, 61(4):044011, Feb. 2000.

[118] M. Fortin, M. Oertel, and C. Providência. Hyperons in hot dense matter: what do the constraints tell us for equation of state? *Publ. Astron. Soc. Aust.*, 35, Dec. 2018.

[119] F. Foucart, P. Laguna, G. Lovelace, D. Radice, and H. Witek. Snowmass2021 Cosmic Frontier White Paper: Numerical relativity for next-generation gravitational-wave probes of fundamental physics. *arXiv e-prints*, page arXiv:2203.08139, Mar. 2022.

[120] C. Freiburghaus, S. Rosswog, and F. K. Thielemann. R-Process in Neutron Star Mergers. *Astrophys. J. Lett.*, 525(2):L121–L124, Nov. 1999.

[121] J. L. Friedman and N. Stergioulas. *Rotating Relativistic Stars*. Cambridge Monographs on Mathematical Physics. Cambridge University Press, 3 2013.

[122] J. L. Friedman and N. Stergioulas. Astrophysical implications of neutron star inspiral and coalescence. *International Journal of Modern Physics D*, 29(11):2041015–632, Jan. 2020.

[123] S. Fujibayashi, K. Kiuchi, S. Wanajo, K. Kyutoku, Y. Sekiguchi, and M. Shibata. Comprehensive study on the mass ejection and nucleosynthesis in the binary neutron star mergers leaving short-lived massive neutron stars. *arXiv e-prints*, page arXiv:2205.05557, May 2022.

[124] E. Gaburov, A. Johansen, and Y. Levin. Magnetically Levitating Accretion Disks around Supermassive Black Holes. *Astrophys. J.*, 758(2):103, Oct. 2012.

[125] R. Gamba, J. S. Read, and L. E. Wade. The impact of the crust equation of state on the analysis of GW170817. *Classical and Quantum Gravity*, 37(2):025008, Jan. 2020.

[126] D. Ganapathy, L. McCuller, J. G. Rollins, E. D. Hall, L. Barsotti, and M. Evans. Tuning Advanced LIGO to kilohertz signals from neutron-star collisions. *Phys. Rev. D*, 103(2):022002, Jan. 2021.

[127] R. A. Gingold and J. J. Monaghan. Smoothed particle hydrodynamics: theory and application to non-spherical stars. *Mon. Not. R. Astron. Soc.*, 181:375–389, Nov. 1977.

[128] R. J. Gleiser, C. O. Nicasio, R. H. Price, and J. Pullin. Gravitational radiation from Schwarzschild black holes: the second-order perturbation formalism. *Phys. Rep.*, 325(2):41–81, Feb. 2000.

[129] S. K. Godunov. A difference method for numerical calculation of discontinuous solutions of the equations of hydrodynamics. *Mat. Sb., Nov. Ser.*, 47:271–306, 1959. in Russian.

[130] A. Goldstein, P. Veres, E. Burns, M. S. Briggs, R. Hamburg, D. Kocevski, C. A. Wilson-Hodge, R. D. Preece, S. Poolakkil, O. J. Roberts, et al. An Ordinary Short Gamma-Ray Burst with Extraordinary Implications: Fermi-GBM Detection of GRB 170817A. *Astrophys. J. Lett.*, 848(2):L14, Oct. 2017.

[131] D. Gondek, P. Haensel, and J. L. Zdunik. Radial pulsations and stability of protoneutron stars. *Astron. Astrophys.*, 325:217–227, Sept. 1997.

[132] S. Goriely, N. Chamel, and J. M. Pearson. Further explorations of Skyrme-Hartree-Fock-Bogoliubov mass formulas. XII. Stiffness and stability of neutron-star matter. *Phys. Rev. C*, 82(3):035804, Sept. 2010.

[133] K. M. Górski, E. Hivon, A. J. Banday, B. D. Wandelt, F. K. Hansen, M. Reinecke, and M. Bartelmann. HEALPix: A Framework for High-Resolution Discretization and Fast Analysis of Data Distributed on the Sphere. *Astrophys. J.*, 622(2):759–771, Apr. 2005.

[134] O. Gottlieb, E. Nakar, T. Piran, and K. Hotokezaka. A cocoon shock breakout as the origin of the γ-ray emission in GW170817. *Mon. Not. R. Astron. Soc.*, 479(1):588–600, Sept. 2018.

[135] E. Gourgoulhon, P. Grandclément, K. Taniguchi, J.-A. Marck, and S. Bonazzola. Quasiequilibrium sequences of synchronized and irrotational binary neutron stars in general relativity: Method and tests. *Phys. Rev. D*, 63(6):064029, Mar. 2001.

[136] S. Gronow, C. E. Collins, S. A. Sim, and F. K. Röpke. Double detonations of sub-M_{Ch} CO white dwarfs: variations in Type Ia supernovae due to different core and He shell masses. *Astron. Astrophys.*, 649:A155, May 2021.

[137] J. Guilet, A. Bauswein, O. Just, and H.-T. Janka. Magnetorotational instability in neutron star mergers: impact of neutrinos. *Mon. Not. R. Astron. Soc.*, 471(2):1879–1887, Oct. 2017.

[138] P. Haensel, A. Y. Potekhin, and D. G. Yakovlev. *Neutron stars 1: Equation of state and structure*, volume 326. Springer, New York, USA, 2007.

[139] E. D. Hall and M. Evans. Metrics for next-generation gravitational-wave detectors. *Classical and Quantum Gravity*, 36(22):225002, Nov. 2019.

[140] G. Hallinan, A. Corsi, K. P. Mooley, K. Hotokezaka, E. Nakar, M. M. Kasliwal, D. L. Kaplan, D. A. Frail, S. T. Myers, T. Murphy, et al. A radio counterpart to a neutron star merger. *Science*, 358(6370):1579–1583, Dec. 2017.

[141] M. Hanauske, K. Takami, L. Bovard, L. Rezzolla, J. A. Font, F. Galeazzi, and H. Stöcker. Rotational properties of hypermassive neutron stars from binary mergers. *Phys. Rev. D*, 96(4):043004, Aug. 2017.

[142] B. Harrison, K. Thorne, M. Wakano, and J. Wheeler. *Gravitation Theory and Gravitational Collapse*. University of Chicago Press, 1965.

[143] A. Harten. High Resolution Schemes for Hyperbolic Conservation Laws. *J. Comput. Phys.*, 49(3):357–393, Mar. 1983.

[144] A. Harten. On a Class of High Resolution Total-Variation-Stable Finite-Difference Schemes. *SIAM Journal on Numerical Analysis*, 21(1):1–23, Feb. 1984.

[145] A. Harten, B. Engquist, S. Osher, and S. R. Chakravarthy. Uniformly high order accurate essentially non-oscillatory schemes, III. *J. Comput. Phys.*, 71(2):231–303, Aug. 1987.

[146] A. Harten, P. D. Lax, and B. V. Leer. On upstream differencing and godunov-type schemes for hyperbolic conservation laws. *SIAM Rev.*, 25(1):35–61, 1983.

[147] C.-J. Haster, K. Chatziioannou, A. Bauswein, and J. A. Clark. Inference of the Neutron Star Equation of State from Cosmological Distances. *Phys. Rev. Lett.*, 125(26):261101, Dec. 2020.

[148] K. Hebeler. Three-nucleon forces: Implementation and applications to atomic nuclei and dense matter. *Phys. Rep*, 890:1–116, Jan. 2021.

[149] M. Hempel, T. Fischer, J. Schaffner-Bielich, and M. Liebendörfer. New Equations of State in Simulations of Core-collapse Supernovae. *Astrophys. J.*, 748:70, Mar. 2012.

[150] M. Hempel and J. Schaffner-Bielich. A statistical model for a complete supernova equation of state. *Nucl. Phys. A*, 837:210–254, June 2010.

[151] T. Hinderer. Tidal Love Numbers of Neutron Stars. *Astrophys. J.*, 677(2):1216–1220, Apr. 2008.

[152] T. Hinderer, B. D. Lackey, R. N. Lang, and J. S. Read. Tidal deformability of neutron stars with realistic equations of state and their gravitational wave signatures in binary inspiral. *Phys. Rev. D*, 81(12):123016, June 2010.

[153] K. Hotokezaka, K. Kiuchi, K. Kyutoku, T. Muranushi, Y. Sekiguchi, M. Shibata, and K. Taniguchi. Remnant massive neutron stars of binary neutron star mergers: Evolution process and gravitational waveform. *Phys. Rev. D*, 88(4):044026, Aug. 2013.

[154] K. Hotokezaka, K. Kiuchi, K. Kyutoku, H. Okawa, Y.-i. Sekiguchi, M. Shibata, and K. Taniguchi. Mass ejection from the merger of binary neutron stars. *Phys. Rev. D*, 87(2):024001, Jan. 2013.

[155] K. Hotokezaka, K. Kyutoku, H. Okawa, M. Shibata, and K. Kiuchi. Binary neutron star mergers: Dependence on the nuclear equation of state. *Phys. Rev. D*, 83(12):124008, June 2011.

[156] J. R. Ipser and K. S. Thorne. Nonradial Pulsation of General-Relativistic Stellar Models.VI. Corrections. *Astrophys. J.*, 181:181–182, Apr. 1973.

[157] J. Isenberg and J. Nester. Canonical Gravity. In *General Relativity and Gravitation. Vol. 1. One hundred years after the birth of Albert Einstein. Edited by A. Held. New York*, volume 1, page 23, Jan. 1980.

[158] B. Iyer et al. LIGO-India, Proposal of the Consortium for Indian Initiative in Gravitational-wave Observations (IndIGO). Technical Report LIGO-M1100296-v2, 2011. https://dcc.ligo.org/LIGO-M1100296/public.

[159] H. T. Janka, T. Zwerger, and R. Moenchmeyer. Does artificial viscosity destroy prompt type-II supernova explosions? *Astron. Astrophys.*, 268(1):360–368, Feb. 1993.

[160] O. Just, A. Bauswein, R. Ardevol Pulpillo, S. Goriely, and H. T. Janka. Comprehensive nucleosynthesis analysis for ejecta of compact binary mergers. *Mon. Not. R. Astron. Soc.*, 448(1):541–567, Mar. 2015.

[161] KAGRA Collaboration, H. Abe, R. X. Adhikari, T. Akutsu, M. Ando, A. Araya, N. Aritomi, H. Asada, Y. Aso, S. Bae, et al. Performance of the KAGRA detector during the first joint observation with GEO 600 (O3GK). *arXiv e-prints*, page arXiv:2203.07011, Mar. 2022.

[162] Kagra Collaboration, T. Akutsu, M. Ando, K. Arai, Y. Arai, S. Araki, A. Araya, N. Aritomi, H. Asada, Y. Aso, et al. KAGRA: 2.5 generation interferometric gravitational wave detector. *Nature Astronomy*, 3:35–40, Jan. 2019.

[163] D. Kasen, B. Metzger, J. Barnes, E. Quataert, and E. Ramirez-Ruiz. Origin of the heavy elements in binary neutron-star mergers from a gravitational-wave event. *Nature*, 551(7678):80–84, Nov. 2017.

[164] M. M. Kasliwal, E. Nakar, L. P. Singer, D. L. Kaplan, D. O. Cook, A. Van Sistine, R. M. Lau, C. Fremling, O. Gottlieb, J. E. Jencson, et al. Illuminating gravitational waves: A concordant picture of photons from a neutron star merger. *Science*, 358(6370):1559–1565, Dec. 2017.

[165] W. Kastaun, R. Ciolfi, and B. Giacomazzo. Structure of stable binary neutron star merger remnants: A case study. *Phys. Rev. D*, 94(4):044060, Aug. 2016.

[166] K. Kiuchi, P. Cerdá-Durán, K. Kyutoku, Y. Sekiguchi, and M. Shibata. Efficient magnetic-field amplification due to the Kelvin-Helmholtz instability in binary neutron star mergers. *Phys. Rev. D*, 92(12):124034, Dec. 2015.

[167] K. Kiuchi, L. E. Held, Y. Sekiguchi, and M. Shibata. Implementation of advanced Riemann solvers in a neutrino-radiation magnetohydrodynamics code in numerical relativity and its application to a binary neutron star merger. *arXiv e-prints*, page arXiv:2205.04487, May 2022.

[168] K. Kiuchi, K. Kyutoku, Y. Sekiguchi, and M. Shibata. Global simulations of strongly magnetized remnant massive neutron stars formed in binary neutron star mergers. *Phys. Rev. D*, 97(12):124039, June 2018.

[169] K. Kiuchi, K. Kyutoku, M. Shibata, and K. Taniguchi. Revisiting the Lower Bound on Tidal Deformability Derived by AT 2017gfo. *Astrophys. J. Lett.*, 876(2):L31, May 2019.

[170] C. S. Kochanek. Coalescing Binary Neutron Stars. *Astrophys. J.*, 398:234, Oct. 1992.

[171] K. D. Kokkotas and J. Ruoff. Radial oscillations of relativistic stars. *Astron. Astrophys.*, 366:565–572, Feb. 2001.

[172] K. D. Kokkotas and B. G. Schmidt. Quasi-Normal Modes of Stars and Black Holes. *Living Rev. Relativ.*, 2(1):2, Sept. 1999.

[173] M. Kölsch, T. Dietrich, M. Ujevic, and B. Bruegmann. Investigating the mass-ratio dependence of the prompt-collapse threshold with numerical-relativity simulations. *arXiv e-prints*, page arXiv:2112.11851, Dec. 2021.

[174] S. Koudmani, D. Sijacki, M. A. Bourne, and M. C. Smith. Fast and energetic AGN-driven outflows in simulated dwarf galaxies. *Mon. Not. R. Astron. Soc.*, 484(2):2047–2066, Apr. 2019.

[175] C. J. Krüger and K. D. Kokkotas. Fast Rotating Relativistic Stars: Spectra and Stability without Approximation. *Phys. Rev. Lett.*, 125(11):111106, Sept. 2020.

[176] B. D. Lackey, M. Nayyar, and B. J. Owen. Observational constraints on hyperons in neutron stars. *Phys. Rev. D*, 73(2):024021, Jan. 2006.

[177] G. A. Lalazissis, J. König, and P. Ring. New parametrization for the lagrangian density of relativistic mean field theory. *Phys. Rev. C*, 55:540–543, Jan. 1997.

[178] S. Lalit, M. A. A. Mamun, C. Constantinou, and M. Prakash. Dense matter equation of state for neutron star mergers. *European Physical Journal A*, 55(1):10, Jan. 2019.

[179] J. Lattimer. Neutron stars and the nuclear matter equation of state. *Annual Review of Nuclear and Particle Science*, 71(1):433–464, 2021.

[180] J. M. Lattimer. The Nuclear Equation of State and Neutron Star Masses. *Annu. Rev. Nucl. Part. Sci.*, 62(1):485–515, Nov. 2012.

[181] J. M. Lattimer and F. Douglas Swesty. A generalized equation of state for hot, dense matter. *Nuclear Physics A*, 535:331–376, Dec. 1991.

[182] J. M. Lattimer and M. Prakash. Neutron star observations: Prognosis for equation of state constraints. *Phys. Rep.*, 442(1-6):109–165, Apr. 2007.

[183] J. M. Lattimer and D. N. Schramm. Black-Hole-Neutron-Star Collisions. *Astrophys. J. Lett.*, 192:L145, Sept. 1974.

[184] J. M. Lattimer and D. N. Schramm. The tidal disruption of neutron stars by black holes in close binaries. *Astrophys. J.*, 210:549–567, Dec. 1976.

[185] H. K. Lau, P. T. Leung, and L. M. Lin. Inferring Physical Parameters of Compact Stars from their f-mode Gravitational Wave Signals. *Astrophys. J.*, 714(2):1234–1238, May 2010.

[186] D. Lazzati, R. Perna, B. J. Morsony, D. Lopez-Camara, M. Cantiello, R. Ciolfi, B. Giacomazzo, and J. C. Workman. Late Time Afterglow Observations Reveal a Collimated Relativistic Jet in the Ejecta of the Binary Neutron Star Merger GW170817. *Phys. Rev. Lett.*, 120(24):241103, June 2018.

[187] L. Lehner, S. L. Liebling, C. Palenzuela, and P. M. Motl. m =1 instability and gravitational wave signal in binary neutron star mergers. *Phys. Rev. D*, 94(4):043003, Aug. 2016.

[188] L.-X. Li and B. Paczyński. Transient Events from Neutron Star Mergers. *Astrophys. J. Lett.*, 507(1):L59–L62, Nov. 1998.

[189] LIGO Scientific Collaboration, J. Aasi, B. P. Abbott, R. Abbott, T. Abbott, M. R. Abernathy, K. Ackley, C. Adams, T. Adams, P. Addesso, et al. Advanced LIGO. *Classical and Quantum Gravity*, 32(7):074001, Apr. 2015.

[190] M. Linares, T. Shahbaz, and J. Casares. Peering into the Dark Side: Magnesium Lines Establish a Massive Neutron Star in PSR J2215+5135. *Astrophys. J*, 859(1):54, May 2018.

[191] L. Lindblom. Determining the Nuclear Equation of State from Neutron-Star Masses and Radii. *Astrophys. J.*, 398:569, Oct. 1992.

[192] L. Lindblom. The relativistic inverse stellar structure problem. In *Recent Developments on Physics in Strong Gravitational Fields: V Leopoldo García-Colín Mexican Meeting on Mathematical and Experimental Physics*, volume 1577 of *American Institute of Physics Conference Series*, pages 153–164, Jan. 2014.

[193] L. Lindblom and S. L. Detweiler. The quadrupole oscillations of neutron stars. *Astrophys. J. Suppl. Ser.*, 53:73–92, Sept. 1983.

[194] L. Lindblom and N. M. Indik. Spectral approach to the relativistic inverse stellar structure problem. *Phys. Rev. D*, 86(8):084003, Oct. 2012.

[195] L. Lindblom and N. M. Indik. Spectral approach to the relativistic inverse stellar structure problem II. *Phys. Rev. D*, 89(6):064003, Mar. 2014.

[196] G. Lioutas, A. Bauswein, T. Soultanis, R. Pakmor, V. Springel, and F. K. Röpke. General relativistic moving-mesh hydrodynamics simulations with AREPO and applications to neutron star mergers. *arXiv e-prints*, page arXiv:2208.04267, Aug. 2022.

[197] G. Lioutas, A. Bauswein, and N. Stergioulas. Frequency deviations in universal relations of isolated neutron stars and postmerger remnants. *Phys. Rev. D*, 104(4):043011, Aug. 2021.

[198] G. Lioutas and N. Stergioulas. Universal and approximate relations for the gravitational-wave damping timescale of f-modes in neutron stars. *Gen. Relativ. Gravit.*, 50(1):12, Jan. 2018.

[199] J. Lippuner, R. Fernández, L. F. Roberts, F. Foucart, D. Kasen, B. D. Metzger, and C. D. Ott. Signatures of hypermassive neutron star lifetimes on r-process nucleosynthesis in the disc ejecta from neutron star mergers. *Mon. Not. R. Astron. Soc.*, 472(1):904–918, Nov. 2017.

[200] D. Liptai and D. J. Price. General relativistic smoothed particle hydrodynamics. *Mon. Not. R. Astron. Soc.*, 485(1):819–842, May 2019.

[201] X.-D. Liu, S. Osher, and T. Chan. Weighted Essentially Non-oscillatory Schemes. *J. Comput. Phys.*, 115(1):200–212, Nov. 1994.

[202] L. B. Lucy. A numerical approach to the testing of the fission hypothesis. *Astron. J.*, 82:1013–1024, Dec. 1977.

[203] B. Margalit and B. D. Metzger. Constraining the Maximum Mass of Neutron Stars from Multi-messenger Observations of GW170817. *Astrophys. J. Lett.*, 850(2):L19, Dec. 2017.

[204] R. Margutti, E. Berger, W. Fong, C. Guidorzi, K. D. Alexander, B. D. Metzger, P. K. Blanchard, P. S. Cowperthwaite, R. Chornock, T. Eftekhari, et al. The Electromagnetic Counterpart of the Binary Neutron Star Merger LIGO/Virgo GW170817. V. Rising X-Ray Emission from an Off-axis Jet. *Astrophys. J. Lett.*, 848(2):L20, Oct. 2017.

[205] M. Marques, M. Oertel, M. Hempel, and J. Novak. New temperature dependent hyperonic equation of state: Application to rotating neutron star models and I-Q relations. *Phys. Rev. C*, 96(4):045806, 2017.

[206] J. M. Martí and E. Müller. Grid-based Methods in Relativistic Hydrodynamics and Magnetohydrodynamics. *Living Reviews in Computational Astrophysics*, 1(1):3, Dec. 2015.

[207] D. Martynov, H. Miao, H. Yang, F. H. Vivanco, E. Thrane, R. Smith, P. Lasky, W. E. East, R. Adhikari, A. Bauswein, A. Brooks, Y. Chen, T. Corbitt, A. Freise, H. Grote, Y. Levin, C. Zhao, and A. Vecchio. Exploring the sensitivity of gravitational wave detectors to neutron star physics. *Phys. Rev. D*, 99(10):102004, May 2019.

[208] B. D. Metzger. Kilonovae. *Living Reviews in Relativity*, 23(1):1, Dec. 2019.

[209] B. D. Metzger, G. Martínez-Pinedo, S. Darbha, E. Quataert, A. Arcones, D. Kasen, R. Thomas, P. Nugent, I. V. Panov, and N. T. Zinner. Electromagnetic counterparts of compact object mergers powered by the radioactive decay of r-process nuclei. *Mon. Not. R. Astron. Soc.*, 406(4):2650–2662, Aug. 2010.

[210] A. Mignone and G. Bodo. An HLLC Riemann solver for relativistic flows - I. Hydrodynamics. *Mon. Not. R. Astron. Soc.*, 364(1):126–136, Nov. 2005.

[211] J. J. Monaghan. Smoothed particle hydrodynamics. *Annu. Rev. Astron. Astrophys.*, 30:543–574, Jan. 1992.

[212] J. J. Monaghan. SPH and Riemann Solvers. *J. Comput. Phys.*, 136(2):298–307, Sept. 1997.

[213] J. J. Monaghan and J. C. Lattanzio. A refined particle method for astrophysical problems. *Astron. Astrophys.*, 149(1):135–143, Aug. 1985.

[214] E. R. Most, S. P. Harris, C. Plumberg, M. G. Alford, J. Noronha, J. Noronha-Hostler, F. Pretorius, H. Witek, and N. Yunes. Projecting the likely importance of weak-interaction-driven bulk viscosity in neutron star mergers. *Mon. Not. R. Astron. Soc.*, 509(1):1096–1108, Jan. 2022.

[215] E. R. Most, L. J. Papenfort, and L. Rezzolla. Beyond second-order convergence in simulations of magnetized binary neutron stars with realistic microphysics. *Mon. Not. R. Astron. Soc.*, 490(3):3588–3600, Dec. 2019.

[216] E. Nakar. Short-hard gamma-ray bursts. *Phys. Rep.*, 442(1-6):166–236, Apr. 2007.

[217] E. Nakar, O. Gottlieb, T. Piran, M. M. Kasliwal, and G. Hallinan. From γ to Radio: The Electromagnetic Counterpart of GW170817. *Astrophys. J.*, 867(1):18, Nov. 2018.

[218] R. Oechslin and H. T. Janka. Gravitational Waves from Relativistic Neutron-Star Mergers with Microphysical Equations of State. *Phys. Rev. Lett.*, 99(12):121102, Sept. 2007.

[219] R. Oechslin, H. T. Janka, and A. Marek. Relativistic neutron star merger simulations with non-zero temperature equations of state. I. Variation of binary parameters and equation of state. *Astron. Astrophys.*, 467(2):395–409, May 2007.

[220] R. Oechslin, S. Rosswog, and F.-K. Thielemann. Conformally flat smoothed particle hydrodynamics application to neutron star mergers. *Phys. Rev. D*, 65(10):103005, May 2002.

[221] M. Oertel, M. Hempel, T. Klähn, and S. Typel. Equations of state for supernovae and compact stars. *Rev. Mod. Phys.*, 89(1):015007, Jan. 2017.

[222] S. T. Ohlmann, F. K. Röpke, R. Pakmor, and V. Springel. Hydrodynamic Moving-mesh Simulations of the Common Envelope Phase in Binary Stellar Systems. *Astrophys. J. Lett.*, 816(1):L9, Jan. 2016.

[223] S. T. Ohlmann, F. K. Röpke, R. Pakmor, and V. Springel. Constructing stable 3D hydrodynamical models of giant stars. *Astron. Astrophys.*, 599:A5, Mar. 2017.

[224] M. Oliver, D. Keitel, A. L. Miller, H. Estelles, and A. M. Sintes. Matched-filter study and energy budget suggest no detectable gravitational-wave ‘extended emission’ from GW170817. *Mon. Not. R. Astron. Soc*, 485(1):843–850, May 2019.

[225] J. R. Oppenheimer and G. M. Volkoff. On massive neutron cores. *Phys. Rev.*, 55:374–381, Feb 1939.

[226] F. Özel and P. Freire. Masses, Radii, and the Equation of State of Neutron Stars. *Annu. Rev. Astron. Astrophys.*, 54:401–440, Sept. 2016.

[227] F. Özel, D. Psaltis, R. Narayan, and A. Santos Villarreal. On the Mass Distribution and Birth Masses of Neutron Stars. *Astrophys. J.*, 757(1):55, Sept. 2012.

[228] M. A. Page, M. Goryachev, H. Miao, Y. Chen, Y. Ma, D. Mason, M. Rossi, C. D. Blair, L. Ju, D. G. Blair, et al. Gravitational wave detectors with broadband high frequency sensitivity. *Communications Physics*, 4(1):27, Dec. 2021.

[229] R. Pakmor, A. Bauer, and V. Springel. Magnetohydrodynamics on an unstructured moving grid. *Mon. Not. R. Astron. Soc.*, 418(2):1392–1401, Dec. 2011.

[230] R. Pakmor, F. P. Callan, C. E. Collins, S. E. de Mink, A. Holas, W. E. Kerzendorf, M. Kromer, J. T. O'Brien, F. K. Roepke, A. J. Ruiter, I. R. Seitenzahl, L. J. Shingles, S. A. Sim, and S. Taubenberger. On the fate of the secondary white dwarf in double-degenerate double-detonation Type Ia supernovae. *arXiv e-prints*, page arXiv:2203.14990, Mar. 2022.

[231] R. Pakmor, M. Kromer, S. Taubenberger, and V. Springel. Helium-ignited Violent Mergers as a Unified Model for Normal and Rapidly Declining Type Ia Supernovae. *Astrophys. J. Lett.*, 770(1):L8, June 2013.

[232] R. Pakmor, V. Springel, A. Bauer, P. Mocz, D. J. Munoz, S. T. Ohlmann, K. Schaal, and C. Zhu. Improving the convergence properties of the moving-mesh code AREPO. *Mon. Not. R. Astron. Soc.*, 455(1):1134–1143, Jan. 2016.

[233] V. Paschalidis, W. E. East, F. Pretorius, and S. L. Shapiro. One-arm spiral instability in hypermassive neutron stars formed by dynamical-capture binary neutron star mergers. *Phys. Rev. D*, 92(12):121502, Dec. 2015.

[234] A. Perego, D. Radice, and S. Bernuzzi. AT 2017gfo: An Anisotropic and Three-component Kilonova Counterpart of GW170817. *Astrophys. J. Lett.*, 850(2):L37, Dec. 2017.

[235] J. Piekarewicz and F. J. Fattoyev. Impact of the neutron star crust on the tidal polarizability. *Phys. Rev. C*, 99(4):045802, Apr. 2019.

[236] A. S. Pozanenko, M. V. Barkov, P. Y. Minaev, A. A. Volnova, E. D. Mazaeva, A. S. Moskvitin, M. A. Krugov, V. A. Samodurov, V. M. Loznikov, and M. Lyutikov. GRB 170817A Associated with GW170817: Multi-frequency Observations and Modeling of Prompt Gamma-Ray Emission. *Astrophys. J. Lett.*, 852(2):L30, Jan. 2018.

[237] R. Price and K. S. Thorne. Non-Radial Pulsation of General-Relativistic Stellar Models. II. Properties of the Gravitational Waves. *Astrophys. J.*, 155:163, Jan. 1969.

[238] M. Punturo, M. Abernathy, F. Acernese, B. Allen, N. Andersson, K. Arun, F. Barone, B. Barr, M. Barsuglia, M. Beker, et al. The Einstein Telescope: a third-generation gravitational wave observatory. *Classical and Quantum Gravity*, 27(19):194002, Oct. 2010.

[239] D. Radice, S. Bernuzzi, W. Del Pozzo, L. F. Roberts, and C. D. Ott. Probing Extreme-density Matter with Gravitational-wave Observations of Binary Neutron Star Merger Remnants. *Astrophys. J. Lett.*, 842(2):L10, June 2017.

[240] D. Radice, S. Bernuzzi, and C. D. Ott. One-armed spiral instability in neutron star mergers and its detectability in gravitational waves. *Phys. Rev. D*, 94(6):064011, Sept. 2016.

[241] D. Radice and L. Dai. Multimessenger parameter estimation of GW170817. *European Physical Journal A*, 55(4):50, Apr. 2019.

[242] D. Radice, F. Galeazzi, J. Lippuner, L. F. Roberts, C. D. Ott, and L. Rezzolla. Dynamical mass ejection from binary neutron star mergers. *Mon. Not. R. Astron. Soc.*, 460(3):3255–3271, Aug. 2016.

[243] D. Radice, A. Perego, K. Hotokezaka, S. A. Fromm, S. Bernuzzi, and L. F. Roberts. Binary Neutron Star Mergers: Mass Ejection, Electromagnetic Counterparts, and Nucleosynthesis. *Astrophys. J.*, 869(2):130, Dec. 2018.

[244] D. Radice, A. Perego, F. Zappa, and S. Bernuzzi. GW170817: Joint Constraint on the Neutron Star Equation of State from Multimessenger Observations. *Astrophys. J. Lett.*, 852(2):L29, Jan. 2018.

[245] C. A. Raithel and E. R. Most. Characterizing the Breakdown of Quasi-universality in Postmerger Gravitational Waves from Binary Neutron Star Mergers. *Astrophys. J. Lett.*, 933(2):L39, July 2022.

[246] J. S. Read, B. D. Lackey, B. J. Owen, and J. L. Friedman. Constraints on a phenomenologically parametrized neutron-star equation of state. *Phys. Rev. D*, 79(12):124032, June 2009.

[247] J. S. Read, B. D. Lackey, B. J. Owen, and J. L. Friedman. Constraints on a phenomenologically parametrized neutron-star equation of state. *Phys. Rev. D*, 79(12):124032, June 2009.

[248] L. Rezzolla, E. R. Most, and L. R. Weih. Using Gravitational-wave Observations and Quasi-universal Relations to Constrain the Maximum Mass of Neutron Stars. *Astrophys. J. Lett.*, 852(2):L25, Jan. 2018.

[249] L. Rezzolla and O. Zanotti. *Relativistic Hydrodynamics*. OUP Oxford, 2013.

[250] P. L. Roe. Some contributions to the modelling of discontinuous flows. In *Large-Scale Computations in Fluid Mechanics*, pages 163–193, Jan. 1985.

[251] S. Rosswog. Astrophysical smooth particle hydrodynamics. *New Astron. Rev.*, 53(4-6):78–104, Apr. 2009.

[252] S. Rosswog. Conservative, special-relativistic smoothed particle hydrodynamics. *J. Comput. Phys.*, 229(22):8591–8612, Nov. 2010.

[253] S. Rosswog. SPH Methods in the Modelling of Compact Objects. *Living rev. comput. astrophys.*, 1(1):1, Oct. 2015.

[254] S. Rosswog and P. Diener. SPHINCS_BSSN: a general relativistic smooth particle hydrodynamics code for dynamical spacetimes. *Classical and Quantum Gravity*, 38(11):115002, June 2021.

[255] M. Ruiz, S. L. Shapiro, and A. Tsokaros. GW170817, general relativistic magnetohydrodynamic simulations, and the neutron star maximum mass. *Phys. Rev. D*, 97(2):021501, Jan. 2018.

[256] G. Ryan and A. MacFadyen. Minidisks in Binary Black Hole Accretion. *Astrophys. J.*, 835(2):199, Feb. 2017.

[257] M. Saleem, J. Rana, V. Gayathri, A. Vijaykumar, S. Goyal, S. Sachdev, J. Suresh, S. Sudhagar, A. Mukherjee, G. Gaur, et al. The science case for LIGO-India. *Classical and Quantum Gravity*, 39(2):025004, Jan. 2022.

[258] N. Sarin and P. D. Lasky. The evolution of binary neutron star post-merger remnants: a review. *General Relativity and Gravitation*, 53(6):59, June 2021.

[259] V. Savchenko, C. Ferrigno, E. Kuulkers, A. Bazzano, E. Bozzo, S. Brandt, J. Chenevez, T. J. L. Courvoisier, R. Diehl, A. Domingo, et al. INTEGRAL Detection of the First Prompt Gamma-Ray Signal Coincident with the Gravitational-wave Event GW170817. *Astrophys. J. Lett.*, 848(2):L15, Oct. 2017.

[260] F. R. N. Schneider, S. T. Ohlmann, P. Podsiadlowski, F. K. Röpke, S. A. Balbus, R. Pakmor, and V. Springel. Stellar mergers as the origin of magnetic massive stars. *Nature*, 574(7777):211–214, Oct. 2019.

[261] B. F. Schutz. Networks of gravitational wave detectors and three figures of merit. *Classical and Quantum Gravity*, 28(12):125023, June 2011.

[262] G. Shen, C. J. Horowitz, and S. Teige. New equation of state for astrophysical simulations. *Phys. Rev. C*, 83(3):035802, Mar. 2011.

[263] M. Shibata. Constraining Nuclear Equations of State Using Gravitational Waves from Hypermassive Neutron Stars. *Phys. Rev. Lett.*, 94(20):201101, May 2005.

[264] M. Shibata. Constraining nuclear equations of state using gravitational waves from hypermassive neutron stars. *Phys. Rev. Lett.*, 94:201101, May 2005.

[265] M. Shibata. *Numerical Relativity.* 100 years of general relativity. World Scientific Publishing Company Pte. Limited, 2016.

[266] M. Shibata, S. Fujibayashi, K. Hotokezaka, K. Kiuchi, K. Kyutoku, Y. Sekiguchi, and M. Tanaka. Modeling GW170817 based on numerical relativity and its implications. *Phys. Rev. D*, 96(12):123012, Dec. 2017.

[267] M. Shibata and K. Taniguchi. Merger of binary neutron stars to a black hole: Disk mass, short gamma-ray bursts, and quasinormal mode ringing. *Phys. Rev. D*, 73(6):064027, Mar. 2006.

[268] M. Shibata, K. Taniguchi, and K. Uryū. Merger of binary neutron stars with realistic equations of state in full general relativity. *Phys. Rev. D*, 71(8):084021, Apr. 2005.

[269] M. Shibata and K. Uryū. Gravitational Waves from Merger of Binary Neutron Stars in Fully General Relativistic Simulation. *Progress of Theoretical Physics*, 107(2):265–303, Feb. 2002.

[270] D. M. Siegel and B. D. Metzger. Three-Dimensional General-Relativistic Magnetohydrodynamic Simulations of Remnant Accretion Disks from Neutron Star Mergers: Outflows and r -Process Nucleosynthesis. *Phys. Rev. Lett.*, 119(23):231102, Dec. 2017.

[271] M. Soares-Santos, D. E. Holz, J. Annis, R. Chornock, K. Herner, E. Berger, D. Brout, H. Y. Chen, R. Kessler, M. Sako, et al. The Electromagnetic Counterpart of the Binary Neutron Star Merger LIGO/Virgo GW170817. I. Discovery of the Optical Counterpart Using the Dark Energy Camera. *Astrophys. J. Lett.*, 848(2):L16, Oct. 2017.

[272] T. Soultanis, A. Bauswein, and N. Stergioulas. Analytic models of the spectral properties of gravitational waves from neutron star merger remnants. *Phys. Rev. D*, 105(4):043020, Feb. 2022.

[273] V. Springel. E pur si muove: Galilean-invariant cosmological hydrodynamical simulations on a moving mesh. *Mon. Not. R. Astron. Soc.*, 401(2):791–851, Jan. 2010.

[274] A. W. Steiner, M. Hempel, and T. Fischer. Core-collapse supernova equations of state based on neutron star observations. *Astrophys. J.*, 774:17, Sept. 2013.

[275] N. Stergioulas, A. Bauswein, K. Zagkouris, and H.-T. Janka. Gravitational waves and non-axisymmetric oscillation modes in mergers of compact object binaries. *Mon. Not. R. Astron. Soc.*, 418(1):427–436, Nov. 2011.

[276] N. Stergioulas, A. Bauswein, K. Zagkouris, and H.-T. Janka. Gravitational waves and non-axisymmetric oscillation modes in mergers of compact object binaries. *Mon. Not. R. Astron. Soc*, 418:427–436, Nov. 2011.

[277] Y. Sugahara and H. Toki. Relativistic mean-field theory for unstable nuclei with non-linear σ and ω terms. *Nuclear Physics A*, 579:557–572, Oct. 1994.

[278] A. Suresh and H. T. Huynh. Accurate Monotonicity-Preserving Schemes with Runge Kutta Time Stepping. *J. Comput. Phys.*, 136(1):83–99, Sept. 1997.

[279] E. Symbalisty and D. N. Schramm. Neutron Star Collisions and the r-Process. *Astrophys. Lett.*, 22:143, Jan. 1982.

[280] K. Takami, L. Rezzolla, and L. Baiotti. Constraining the Equation of State of Neutron Stars from Binary Mergers. *Phys. Rev. Lett.*, 113(9):091104, 2014.

[281] K. Takami, L. Rezzolla, and L. Baiotti. Spectral properties of the post-merger gravitational-wave signal from binary neutron stars. *Phys. Rev. D*, 91(6):064001, Mar. 2015.

[282] M. Tanaka, Y. Utsumi, P. A. Mazzali, N. Tominaga, M. Yoshida, Y. Sekiguchi, T. Morokuma, K. Motohara, K. Ohta, K. S. Kawabata, et al. Kilonova from post-merger ejecta as an optical and near-Infrared counterpart of GW170817. *Publ. Astron. Soc. Jpn.*, 69(6):102, Dec. 2017.

[283] The LIGO Scientific Collaboration, the Virgo Collaboration, R. Abbott, T. D. Abbott, F. Acernese, K. Ackley, C. Adams, N. Adhikari, R. X. Adhikari, V. B. Adya, et al. GWTC-2.1: Deep Extended Catalog of Compact Binary Coalescences Observed by LIGO and Virgo During the First Half of the Third Observing Run. *arXiv e-prints*, page arXiv:2108.01045, Aug. 2021.

[284] The LIGO Scientific Collaboration, the Virgo Collaboration, the KAGRA Collaboration, R. Abbott, T. D. Abbott, F. Acernese, K. Ackley, C. Adams, N. Adhikari, R. X. Adhikari, et al. GWTC-3: Compact Binary Coalescences Observed by LIGO and Virgo During the Second Part of the Third Observing Run. *arXiv e-prints*, page arXiv:2111.03606, Nov. 2021.

[285] K. S. Thorne. Nonradial Pulsation of General-Relativistic Stellar Models. III. Analytic and Numerical Results for Neutron Stars. *Astrophys. J.*, 158:1, Oct. 1969.

[286] K. S. Thorne. Nonradial Pulsation of General-Relativistic Stellar Models.IV. The Weakfield Limit. *Astrophys. J.*, 158:997, Dec. 1969.

[287] K. S. Thorne and A. Campolattaro. Non-Radial Pulsation of General-Relativistic Stellar Models. I. Analytic Analysis for $L >= 2$. *Astrophys. J.*, 149:591, Sept. 1967.

[288] H. Toki, D. Hirata, Y. Sugahara, K. Sumiyoshi, and I. Tanihata. Relativistic many body approach for unstable nuclei and supernova. *Nuclear Physics A*, 588:357–363, Feb. 1995.

[289] R. C. Tolman. Static solutions of einstein's field equations for spheres of fluid. *Phys. Rev.*, 55:364–373, Feb 1939.

[290] E. F. Toro. *Riemann Solvers and Numerical Methods for Fluid Dynamics: A Practical Introduction.* Springer Science & Business Media, Apr. 2009.

[291] E. F. Toro, M. Spruce, and W. Speares. Restoration of the contact surface in the HLL-Riemann solver. *Shock Waves*, 4(1):25–34, July 1994.

[292] A. Torres-Rivas, K. Chatziioannou, A. Bauswein, and J. A. Clark. Observing the post-merger signal of GW170817-like events with improved gravitational-wave detectors. *Phys. Rev. D*, 99(4):044014, Feb. 2019.

[293] E. Troja, L. Piro, H. van Eerten, R. T. Wollaeger, M. Im, O. D. Fox, N. R. Butler, S. B. Cenko, T. Sakamoto, C. L. Fryer, et al. The X-ray counterpart to the gravitational-wave event GW170817. *Nature*, 551(7678):71–74, Nov. 2017.

[294] K. W. Tsang, T. Dietrich, and C. Van Den Broeck. Modeling the postmerger gravitational wave signal and extracting binary properties from future binary neutron star detections. *Phys. Rev. D*, 100(4):044047, Aug. 2019.

[295] L. K. Tsui and P. T. Leung. Universality in quasi-normal modes of neutron stars. *Mon. Not. R. Astron. Soc*, 357(3):1029–1037, Mar. 2005.

[296] S. Typel. Relativistic model for nuclear matter and atomic nuclei with momentum-dependent self-energies. *Phys. Rev. C*, 71(6):064301, 2005.

[297] S. Typel, G. Röpke, T. Klähn, D. Blaschke, and H. H. Wolter. Composition and thermodynamics of nuclear matter with light clusters. *Phys. Rev. C*, 81(1):015803, Jan. 2010.

[298] S. Valenti, D. J. Sand, S. Yang, E. Cappellaro, L. Tartaglia, A. Corsi, S. W. Jha, D. E. Reichart, J. Haislip, and V. Kouprianov. The Discovery of the Electromagnetic Counterpart of GW170817: Kilonova AT 2017gfo/DLT17ck. *Astrophys. J. Lett.*, 848(2):L24, Oct. 2017.

[299] B. van Leer. Towards the Ultimate Conservative Difference Scheme. IV. A New Approach to Numerical Convection. *J. Comput. Phys.*, 23:276, Mar. 1977.

[300] B. van Leer. Towards the Ultimate Conservative Difference Scheme. V. A Second-Order Sequel to Godunov's Method. *J. Comput. Phys.*, 32(1):101–136, July 1979.

[301] B. Vandenbroucke and S. De Rijcke. The moving mesh code SHADOWFAX. *Astronomy and Computing*, 16:109–130, July 2016.

[302] V. A. Villar, J. Guillochon, E. Berger, B. D. Metzger, P. S. Cowperthwaite, M. Nicholl, K. D. Alexander, P. K. Blanchard, R. Chornock, T. Eftekhari, et al. The Combined Ultraviolet, Optical, and Near-infrared Light Curves of the Kilonova Associated with the Binary Neutron Star Merger GW170817: Unified Data Set, Analytic Models, and Physical Implications. *Astrophys. J. Lett.*, 851(1):L21, Dec. 2017.

[303] M. Vogelsberger, S. Genel, V. Springel, P. Torrey, D. Sijacki, D. Xu, G. Snyder, S. Bird, D. Nelson, and L. Hernquist. Properties of galaxies reproduced by a hydrodynamic simulation. *Nature*, 509(7499):177–182, May 2014.

[304] M. Vogelsberger, D. Sijacki, D. Kereš, V. Springel, and L. Hernquist. Moving mesh cosmology: numerical techniques and global statistics. *Mon. Not. R. Astron. Soc.*, 425(4):3024–3057, Oct. 2012.

[305] S. Vretinaris, N. Stergioulas, and A. Bauswein. Empirical relations for gravitational-wave asteroseismology of binary neutron star mergers. *Phys. Rev. D*, 101(8):084039, Apr. 2020.

[306] D. Watson, C. J. Hansen, J. Selsing, A. Koch, D. B. Malesani, A. C. Andersen, J. P. U. Fynbo, A. Arcones, A. Bauswein, S. Covino, et al. Identification of strontium in the merger of two neutron stars. *Nature*, 574(7779):497–500, Oct. 2019.

[307] R. Weinberger, K. Ehlert, C. Pfrommer, R. Pakmor, and V. Springel. Simulating the interaction of jets with the intracluster medium. *Mon. Not. R. Astron. Soc.*, 470(4):4530–4546, Oct. 2017.

[308] R. Weinberger, V. Springel, and R. Pakmor. The AREPO Public Code Release. *Astrophys. J. Suppl. Ser.*, 248(2):32, June 2020.

[309] D.-H. Wen, B.-A. Li, H.-Y. Chen, and N.-B. Zhang. GW170817 implications on the frequency and damping time of f -mode oscillations of neutron stars. *Phys. Rev. C*, 99(4):045806, Apr. 2019.

[310] H. Wendland. Piecewise polynomial, positive definite and compactly supported radial functions of minimal degree. *Adv. Comput. Math.*, 4(1):389–396, Dec. 1995.

[311] J. R. Wilson and G. J. Mathews. *Relativistic Numerical Hydrodynamics*. Cambridge Monographs on Mathematical Physics. Cambridge University Press, 2003.

[312] J. R. Wilson, G. J. Mathews, and P. Marronetti. Relativistic numerical model for close neutron-star binaries. *Phys. Rev. D*, 54(2):1317–1331, July 1996.

[313] R. B. Wiringa, V. Fiks, and A. Fabrocini. Equation of state for dense nucleon matter. *Phys. Rev. C*, 38:1010–1037, Aug. 1988.

[314] M.-R. Wu, R. Fernández, G. Martínez-Pinedo, and B. D. Metzger. Production of the entire range of r-process nuclides by black hole accretion disc outflows from neutron star mergers. *Mon. Not. R. Astron. Soc.*, 463(3):2323–2334, Dec. 2016.

[315] Z. Xing, J. M. Centrella, and S. L. W. McMillan. Gravitational radiation from coalescing binary neutron stars. *Phys. Rev. D*, 50(10):6247–6261, Nov. 1994.

[316] K. Yagi and N. Yunes. I-Love-Q: Unexpected Universal Relations for Neutron Stars and Quark Stars. *Science*, 341(6144):365–368, July 2013.

[317] A. Yalinewich, E. Steinberg, and R. Sari. RICH: Open-source Hydrodynamic Simulation on a Moving Voronoi Mesh. *Astrophys. J. Suppl. Ser.*, 216(2):35, Feb. 2015.

[318] H. Yang, V. Paschalidis, K. Yagi, L. Lehner, F. Pretorius, and N. Yunes. Gravitational wave spectroscopy of binary neutron star merger remnants with mode stacking. *Phys. Rev. D*, 97(2):024049, Jan. 2018.

[319] F. J. Zerilli. Gravitational field of a particle falling in a schwarzschild geometry analyzed in tensor harmonics. *Phys. Rev. D*, 2:2141–2160, Nov 1970.